Atomic-Scale Study Of Complex Cobalt Oxide

Using Scanning Transmission Electron Microscope

BY

Ahmet Güleç
B.S., Bogazici University, Turkey, 2006

THESIS

Submitted as partial fulfillment of the requirements
for the degree of Doctor of Philosophy in Physics
in the Graduate College of the
University of Illinois at Chicago, 2015

Chicago, Illinois

Defense Committee:

Robert F. Klie, Chair and Advisor
Serdar Öğüt
W. Andreas Schroeder
Alan W. Nicholls, RRC
Christos G. Takoudis, Department of Chemical Engineering

ACKNOWLEDGMENTS

I would like to thank Professor Robert Klie, for his supervision, encouragement, patience and his support during my Ph.D. research. I learned a lot of valuable things from him as a mentor and as a scientist. I am also very thankful to Drs. Alan Nicholls and Ke-bin Low from RRC for teaching me how to use all the experimental tools that I have used during my studies. Additionally, I would like to thank Professors Serdar Öğüt, Andreas Schroeder and Christos Takoudis for being on my committee and for their guidance. Similarly, I would like to acknowledge Dr. Patrick Philips for his valuable comments and direction. I also want to thank Dr. J.F. Mitchell from ANL for providing the Sr-doped single crystal LCO samples and Professor C. Leighton and his group at University of Minnesota for sending me PYCCO samples and for his stimulating discussions about our results. I extend my gratitude to Prof. Peter Schattschneider, Dr. Michael Stöger-Pollach, Stefan Löffler and other members of USTEM, TU Wien, for hosting me in Vienna and guiding me through every aspect of the EMCD method. I am also very thankful to the past and present members of the NSPG group for making things easier. I should also extend my thanks to my family for making Chicago home. Finally, I would like to thank the reader for taking the time to read this thesis.

TABLE OF CONTENTS

TABLE OF CONTENTS (Continued)

CHAPTER **PAGE**

LIST OF FIGURES

LIST OF FIGURES (continued)

LIST OF FIGURES (continued)

LIST OF FIGURES (continued)

LIST OF FIGURES (continued)

LIST OF FIGURES (continued)

LIST OF FIGURES (continued)

LIST OF FIGURES (continued)

LIST OF ABBREVIATIONS

ΔCF	Crystal-Field Splitting
ABF	Annular Bright Field
BF	Bright Filed
CBED	Convergent Beam Electron Diffraction
CCD	Charge-Coupled Device
CTEM	Conventional Transmission Electron Microscopy
DFT	Density Functional Theory
DOS	Density Of States
EDX	Energy-Dispersive X-Ray Spectroscopy
EELS	Electron Energy Loss Spectroscopy
E_F	Fermi Energy
EFTEM	Energy Filtered Transmission Electron Microscope
ELNES	Energy Loss Near Edge Structure
EMCD	Electron Energy-Loss Magnetic Chiral Dichroism
ESD	Energy Spectroscopic Diffraction
ESR	Electron Spin Resonance
EXAFS	Extended X-Ray Absorption Fine Structure
FFT	Fast Fourier Transform
FM	Ferromagnetic
FWHM	Full Width At Half Maximum

LIST OF ABBREVIATIONS (Continued)

GGA	Generalized Gradient Approximation
GIF	Gatan Imaging Filter
HAADF	High-Angle Annular Dark Field
HR	High Resolution
HS	High Spin
INS	Inelastic Neutron Scattering
IS	Intermediate Spin
LAADF	Low-Angle Annular Dark Field
LACDIFF	Large-Angle Convergent Diffraction
LCP	Left Circular Photons
LDA	Local-Density Approximations
LN_2	Liquid Nitrogen
LS	Low Spin
MaBF	Middle Angle Bright Field
MIT	Metal-Insulator Transitions
MR	Magnetoresistivity
NMR	Nuclear Magnetic Resonance
PDF	Neutron Pair Distribution Function
PM	Paramagnetic
RCP	Right Circular Photons
RGB	Red-Green-Blue
RT	Room Temperature

LIST OF ABBREVIATIONS (Continued)

SAD	Selected Area Diffraction
SANS	Small-Angle Neutron Scattering
SST	Spin State Transition
STEM	Scanning Transmission Electron Microscopy
TDS	Thermal Diffuse Scattering
TEM	Transmission Electron Microscopy
VT	Valance Transition
XMCD	X-Ray Magnetic Circular Dichroism
XPS	X-Ray Photoelectron Spectra
ZLP	Zero-Loss Peak

SUMMARY

From superconductors to exotic magnetic phases, cobalt oxides offer a fertile ground for the formation of unique phases involving a mixed valence state of cobalt and/or the presence of oxygen vacancies. Another aspect that distinguishes cobalt oxides from other *3d* transition-metal oxides is the accessibility of different spin states, such as low spin (LS), high spin (HS), and intermediate spin (IS). The presence of such spin states make the physics of the cobalt oxides significantly more complicated and as a results it has not yet been completely understood. In order to improve our understanding of the various phase transitions observed in cobalt oxides, and to comprehend the relationship between crystal and electronic structure, both high energy and high spatial resolution are essential. Fortunately, transmission electron microscopy (TEM) is a technique which is capable of fulfilling both of these requirements. In this thesis, I have utilized a combination of techniques in a scanning transmission electron microscope (STEM) to analyze the atomic-scale structure-property relationship, both at room temperature and through *insitu* cooling to liquid nitrogen (LN_2) temperature. In particular, by using correlated Z-contrast imaging, electron energy loss spectrum (EELS) and electron energy loss magnetic circular dichroism (EMCD), the structure, composition, bonding and magnetic behavior are characterized directly on the atomic scale. In this thesis, I mainly examined two groups of complex cobalt oxides, i) $La_{1-x}Sr_xCoO_3$ (for *x=0.05, 0.17* and *x=0.30*) and ii) $(Pr_{0.85}Y_{0.15})_{0.7}Ca_{03}CoO_3$.

In the $La_{1-x}Sr_xCoO_3$ related part, I found a Co-ion spin state transition in 5% doped $La_{1-x}Sr_xCoO_3$ utilizing the change in the *O K*-edge pre-peak intensity through *in-situ* cooling experiments. On the other hand, for the 17% and 30% doped samples, the doping driven

SUMMARY (continued)

spin state transition is dominant over the thermally driven spin state transition at low temperature.

I also have shown that the CoO_6 octahedral distortions can be measured using HAADF and ABF imaging. In $La_{1-x}Sr_xCoO_3$, increasing the hole doping changes the octahedral distortion, which can be seen as checkerboard pattern such that lowering the doping level increases the octahedral distortion. However, at high dopant level (x=0.3) the single crystal sample contains some areas where the distortions are strong but not well-ordered, while others show very little distortions. Additionally, the octahedral distortion found by ABF imaging is characterized by the atomic-column resolved EELS maps, where the oxygen displacement is directly measured.

For critically doped $La_{1-x}Sr_xCoO_3$ (*x=0.17*), I investigated the chemical and magnetic sample inhomogeneities at room and liquid nitrogen temperatures, using the O and Co near edge fine structures. Finally, I applied the EMCD method to quantify the local magnetism in $La_{1-x}Sr_xCoO_3$ single crystal samples at low spatial, as well as high spatial resolution. On average, the samples characterized at low temperature and/or with high hole doping concentration exhibit a higher dichromatic signal. The spatial distribution of magnetic ordering of the 17% doped sample at room temperature is examined and the result suggested the coexistence of LS, IS and HS states.

I also have investigated the valance state transition in $(Pr_{0.85}Y_{0.15})_{0.70}Ca_{0.30}CoO_3$, which has been reported to have a simultaneous metal to insulator transition (MIT) and a sharp drop in magnetic moment upon cooling as some fraction of the Pr ions increase their

SUMMARY (continued)

oxidation state from *3+* to *4+*. The Pr *M* edge fine structure is examined as a function of sample temperature to confirm the Pr oxidation state change. Since the Co L_2 and L_3 edges do not show any interpretable change during the cooling experiment, the *O K*-edge pre-peak intensity is used to quantify the Co valance state. Using as set of $Pr_{1-x}Ca_xCoO_6$ samples as a reference, I found that there exists a partial oxidation state transition of Co ions, such that during the cooling, the oxidation state of Co changes from ~*+3.3* to ~*+3*. Furthermore, at room temperature, occasional structural modulation associated with oxygen vacancy ordering is observed. Below the transition temperature, these structural modulation disappear nearly completely which is interpreted as the diffusion of oxygen vacancies as the result of the charge transfer from Pr ions to Co ions.

Finally, I presented experimental results showing that the EELS near edge fine structure varies in several 3d-transition metal perovskite oxides, such as $(Pr_{0.85}Y_{0.15})_{0.7}Ca_{03}CoO_3$, $La_{1-x}Sr_xCoO_3$, $BiFeO_3$ and $SrTiO_3$ as a function of probe position, if it is smaller than the interatomic spacing. Except for $SrTiO_3$, all the samples show changes in the white line ratio of the transition metals depending on the probe position within the projected unit-cell. These deviations suggest that the conventional way of quantifying the valence states of transition metal oxides using the white line ration is no longer valid when using small probes. This could be either due to channeling effects, or the fact that different initial states are measured when the probe moves of the column. However, it is not easy to get a definitive answer to that question and this subject needs significant additional theoretical calculations.

1 INTRODUCTION

Having a wide range of fascinating physical properties, transition metal oxides have been studied for over half a century. However, our understanding of many of the physical properties exhibited by transition metal oxides remains incomplete. Amongst this large group of transition metal oxides, cobalt oxides can provide variety of applications such as gas sensors, solid oxide fuel cell, oxygen membrane, magnetic data storage, heterogeneous catalysis because of their diverse properties including ionic conductivity, thermo-electricity, superconductivity, magnetic and insulator–metal transitions (IMT) and magnetoresistivity (MR). (1). Additionally, the several layered cobalt oxides generate the high thermopower which makes them to be considered as a feasible substitute to the traditional semiconducting thermoelectric materials (2, 3).

In order to improve our understanding of the various phase transitions observed in Cobalt oxides and to comprehend the relationship between crystal and electronic structure, both high energy resolution and high spatial resolution are essential. Fortunately, transmission electron microscopy (TEM) is a technique which is capable of fulfilling both of these requirements. In this thesis, I have utilized a combination of techniques in a scanning transmission electron microscope (STEM) to analyze the atomic-scale structure-property relationship, both at room temperature and through *in-situ* cooling to liquid nitrogen (LN_2) temperature. In particular, by using correlated Z-contrast imaging and electron energy loss spectroscopy (EELS), the structure, composition and bonding can be characterized directly

on the atomic scale. Light atoms, like H, O and C, can be directly seen using annular bright field (ABF) images.

Cobalt, having several possible oxidation states, Co^{2+}, $Co3^{+}$, and Co^{4+}, offers a wide field for the creation of novel structures, involving a mixed valence or spin state of cobalt and/or the presence of oxygen vacancies. A specific property of cobalt oxides is the ability to adopt various spin states, such as a low spin (LS), high spin (HS), and intermediate spin (IS), as well as a temperature induced transition between those spin states. These spin states transitions are related to the competition between the crystal-field splitting (Δ_{CF}) of the Co *3d* states into e_g and t_{2g} orbitals, which encourage the lower spin states, and the Hund's exchange rule, which is responsible for higher spin configurations.

$LaCoO_3$-based perovskite oxides have been studied for decades, primarily due to their exceptional magnetic transitions which are related to changes the Co^{3+}-ion spin states. Bulk $LaCoO_3$ has a temperature dependent transition from a nonmagnetic to a semiconducting insulating state, which occurs below 100 K and another transition from semiconducting to metallic phase above 500 K. The first magnetic transition is believed(4),(5),(6) to be due to a change in the Co^{3+}-ion spin state from a low spin-LS ($t^{6}_{2g}\ e^{0}_{g}\ S=0$) state to a combination of -HS ($t^{4}_{2g}\ e^{2}_{g}\ S=2$) and LS states(7) or alternatively an IS ($t^{5}_{2g}\ e^{1}_{g}\ S=1$) state(8, 9). The high-temperature transition stems from a change in the intermediate temperature Co^{3+}-ion spin-state to the HS state. The possible spin state configurations of different Co ions are shown in Figure 1.

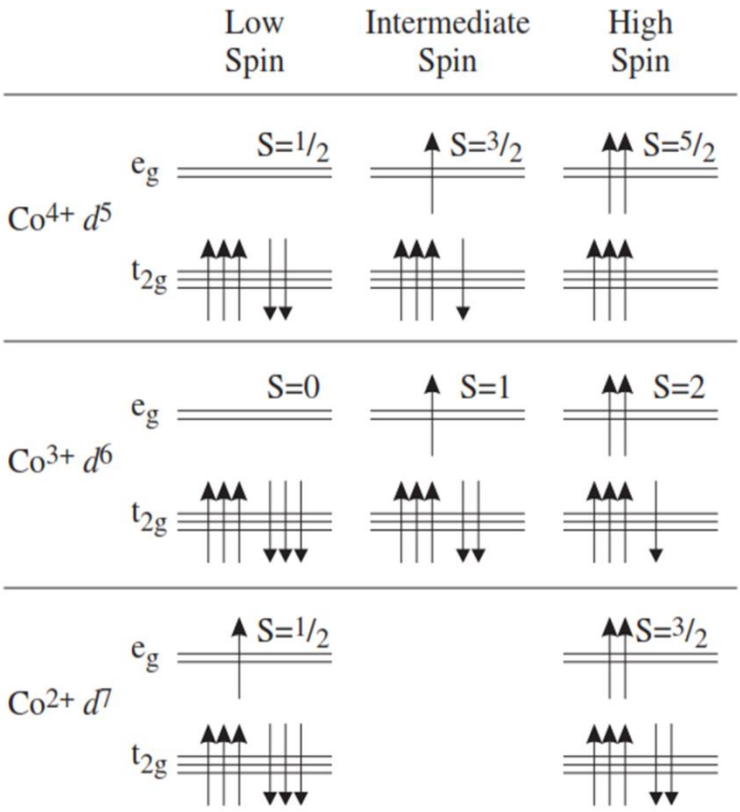

Figure 1 Possible Spin state configuration of Co with different *d* orbital electron population.

To achieve magnetic ordering in $LaCoO_3$, a change in grain size of powder samples(10), the application of epitaxial tensile strain on thin film sample via the properly chosen substrate(11),(12), the application of external pressure to bulk sample(13),(14) or hole doping with an alkaline rare-earth ion having a different ionic radius, such as *Sr*, has been previously suggested.

The substitution of a divalent cations in $LaCoO_3$, such as Sr^{2+}, is of great scientific interest since it allows for the formation of a mixed Co^{3+}, Co^{4+} valence state. $La_{1-x}Sr_xCoO_3$ have

been the object of numerous experimental studies, from Extended X-ray Absorption Fine Structure (EXAFS), Neutron Pair Distribution Function (PDF)(15), NMR(16),(17) , Small-Angle Neutron Scattering (SANS)(18), and Inelastic Neutron Scattering (INS), to Electron Spin Resonance (ESR)(19). A detailed phase diagram as a function of doping concentration and temperature has been constructed based on these experiments (16) as shown in Figure 2, where the blue line marks the expected spin-state transition temperature seen in the hole-poor regions. As seen in Figure 2, there are five distinct magnetic phases as function of dopant concentration and temperature, namely, paramagnetic region, spin polaron region, which are nucleating around Sr dopants, a region with long range homogenous ferromagnetic ordering, an inhomogeneous ferromagnetic region and, finally, a spin glass region at low temperature. An Insulator Metal Transition (IMT), which is indicated with red dashed line, is also observed at *x=0.17*.

However, there is no general consensus on the crystal symmetries of this family of materials. The rhombohedral $R\bar{3}c$ space group is claimed to be suitable symmetry for samples with higher Sr doping concentrations. (20, 21). On the other hand, the *I2/a* space group, which allows for Jahn–Teller distortions associated with the intermediate Co^{3+}-ion spin state, has been reported for structures with broken symmetry in the CoO_6 octahedra.(22, 23)

Moreover, a change in the lattice parameters and the CoO_6 distortions affects the Co-O bond distance, the Co-O-Co bond angle, and ultimately the magnetic ordering(24). Therefore, substituting divalent Sr^{2+} ions for trivalent La^{+3} ions does not only increase the

average Co oxidation state and spin states, but also changes the structure of CoO_6 environment which can directly alter the spin state and spin ordering of Co ions. Recently, first-principles calculations revealed that the cubic octahedral environment is more stable in magnetic states compared to the non-magnetic ones, while introducing rhombohedral distortion lowers the non-magnetic ground state energy and thus the insulating character.(25)

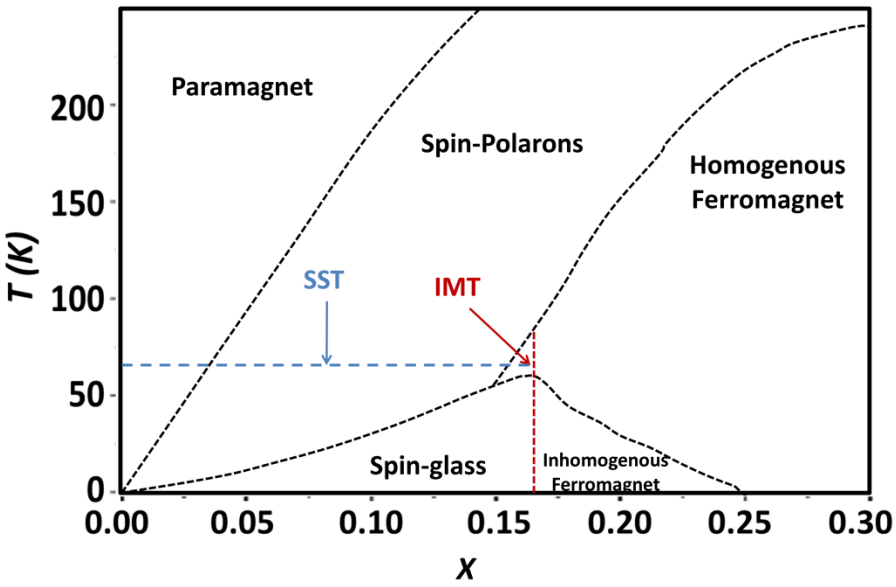

Figure 2 The $La_{1-x}Sr_xCoO_3$ phase diagram. Adapted from (16).

To date, it is generally accepted that with increasing Sr-doping concentration, $La_{1-x}Sr_xCoO_3$ changes its magnetic ordering from paramagnet to a ferromagnet (as shown in Figure 2). Additionally, at the low Sr doping concentration, Co ions undergo a thermally induced spin-state transition at low temperature, from higher spin states to low spin state.

As the Sr-doping concentration increases, spin polarons, which are caused by substituting divalent Sr^{2+} ions for trivalent La^{+3} ions, merge and form short-range FM clusters, since the neighboring mixed valance Co ions interact ferromagnatically via double exchange mechanism(17). At the critical doping of $x \approx 0.17$, the clusters percolate, leading to a crossover from a short- to long-range FM material. (26) The system simultaneously undergoes a percolative insulator-to-metal transition (IMT).(17)

The goal of my thesis work is to address the following objectives related to the $La_{1-x}Sr_xCoO_3$ system:

- To investigate the spin state transition of $La_{1-x}Sr_xCoO_3$ at low temperature as a function of hole dope concentration.
- To investigate the local CoO_6 octahedral distortions.
- To investigate the inhomogeneity of the Co oxidation state.
- To determine the existence of a dichroic signal during cooling experiment and at room temperature.
- To examine the spatially resolved spin-state map and determine the percolative nature of magnetism in critically doped $La_{1-x}Sr_xCoO_3$.

The second kind of cobalt oxide studied in this thesis is $(Pr_{1-y}Y_y)_{0.7}Ca_{0.3}CoO_3$, which has been reported to have a simultaneous metal to insulator transition (MIT) and a sharp drop in magnetic moment upon cooling. The temperature dependence of the specific heat for $(Pr_{1-y}Y_y)_{0.7}Ca_{0.3}CoO_3$ as a function of Y doping is shown in Figure 3 (27) (28, 29) where the abrupt changes in specific heat stem from metal-insulator transitions. In general, for the

same amount of Ca content, the Y doping stabilizes the transition at higher temperature. $(Pr_{1-y}Y_y)_{0.7}Ca_{0.3}CoO_3$ appears to be the only system, where the Pr ions are observed to undergo a valance state transition from 3+ to 4+, which led to the speculation that the valance state was related to the trapping of holes in the Pr *4f* O *2p* hybridized orbitals.(30). A number of x-ray absorption experiments spectroscopy (XAS) measurements strongly suggest the transfer of electrons into the hybridized Co-O states. (31, 32)

The crystal structure of $(Pr_{1-y}Y_y)_{0.7}Ca_{0.3}CoO_3$ has been described as an orthorhombic perovskite [with space group *Pbnm* (or equivalently *Pnma*)].(33) (34) (35) This symmetry allows for large CoO_6 distortion which was claimed to be the reason for the observed MIT at high temperature (36).

In my thesis, the following issues related to $(Pr_{1-y}Y_y)_{0.7}Ca_{0.3}CoO_3$ are addressed:

- Low and room temperature local structural analysis using HAADF and ABF imaging.
- Spatially resolved elemental map to investigate chemical inhomogeneities.
- Investigating electronic and spin state transition through i*n-situ* cooling below the MIT temperature.
- Map the Pr valance state below the MIT temperature.

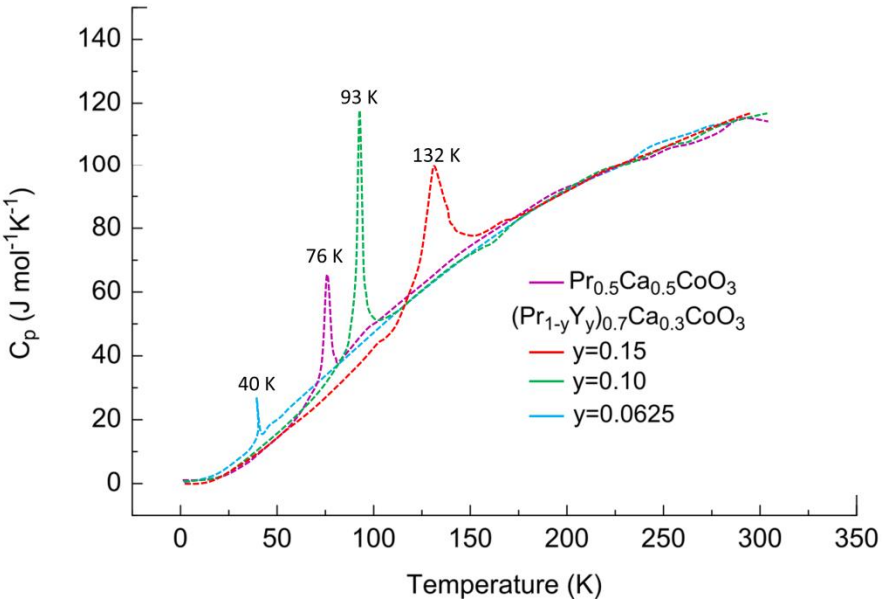

Figure 3 Temperature dependence of the specific heat of $(Pr_{1-y}Y_y)_{0.7}Ca_{0.3}CoO_3$ (y =0.0625−0.15) and $Pr_{0.5}Ca_{0.5}CoO_3$. The critical temperatures of M-I transitions are marked. Adapted from (37)

EELS allows us to identify the chemical composition of atomic column by probing the energy necessary for the excitation of an inner shell electron to unoccupied orbitals. The resulting EELS fine structure provides the local electronic structure information. With the development of aberration correctors in transmission electron microscope, sub-angstrom probe sizes are now possible, enabling us to investigate the intra-atomic regions of the crystal unit-cell. This is a very new concept which has not been accessible in the pre-aberration corrector era of transmission electron microscope and which has a huge potential. Therefore, the final part of my thesis will try to answer the following question:

- Is probing the oxidation state by using the white line ratio still valid when the probe size is small enough to map inter-atomic space?

The structure of this thesis is as follows: Chapter 2 introduces the basic theory behind the techniques used and describes the experimental methods employed in my PhD research. Chapter 3 focuses on the spin state transition of $La_{1-x}Sr_xCoO_3$ through the *in-situ* cooling experiments. In Chapter 4, the CoO_6 octahedral distortions are quantified and the spatially resolved spin-state map of $La_{1-x}Sr_xCoO_3$ is studied. Chapter 5 focusses on the inter-atomic electron transfer and the associated changes in the local atomic structure of $(Pr_{1-y}Y_y)_{0.7}Ca_{0.3}CoO_3$. In chapter 6, I will present an EELS investigation of several transition metal oxides with subatomic spatial resolution. Finally, Chapter 7 contains a summary of the results of this thesis. The implications of the work are discussed, and possible future work is outlined.

2 METHODS

2.1.1 Introduction

In this chapter, the methods and instruments used in my PhD research are described. Throughout this thesis, an aberration-corrected scanning transmission electron microscope (STEM) is used in an atomic-column resolved annular dark filed (ADF) and annular bright field (ABF) imaging mode which is combined with electron energy loss spectroscopy (EELS) as well as *in-situ* cooling, if necessary. For magnetic measurements, the electron-loss magnetic circular dichroism (EMCD) method is applied at liquid nitrogen (LN_2) and room temperature. (38-43)

2.2 Transmission Electron Microscopy (TEM)

Historically, Transmission Electron Microscope (TEM) was invented to improve upon the resolution of light microscope which was limited by the wavelength of visible light. In principle, a TEM provides an environment for a scattering experiment and allows for the detection of the outcome of such experiments using detectors similar to other quantum level, molecular, atomic and even sub-atomic probes, such as synchrotrons, particle accelerators etc. In a scattering experiment, three things should be provided, namely:

- Incident beam (probe),
- the interaction between the sample and the beam,
- the detection or the detectors to identify the electron exit wave .

I will talk about these three parts from a TEM perspective. However, first I will introduce the optical components of the instruments.

A TEM consists of three main components: an illumination system, an objective lens and sample stage, and an imaging system. The first, the illumination system, consists of an electron gun and a series of condenser lenses which focus the electron beam on to the specimen. These lenses can be configured to focus the beam to a point, as in a STEM, or into a parallel beam, as in a conventional TEM (CTEM). These two modes of operation are shown diagrammatically in Figure 4 *a)* and *b)* and the all the signals generated after the interaction is shown Figure 4*c).* In the conventional TEM (CTEM) mode, which is a wide-beam technique, a close-to-parallel electron beam floods the whole area of interest and the image, formed by an imaging (objective) lens after the thin specimen, is collected in parallel. It is also consider as *coherent imaging,* where the interaction between the incoming electron wave and the potential of the nuclei in the specimen results in a phase shift of the incident beam at the exit surface, i.e., the object can be represented by a transmission function. (40) On the other hand, the scanning TEM (STEM) uses a fine focused beam, formed by a probe forming (objective) lens before the specimen, to address each pixel in series as the probe is scanned across the specimen(44). If the diffracted beams do not overlap on the detectors, such as at higher angles, this kind of imaging is considered as *incoherent imaging* since each pixel in the final image stem from different interaction of incident beam and the specimen.

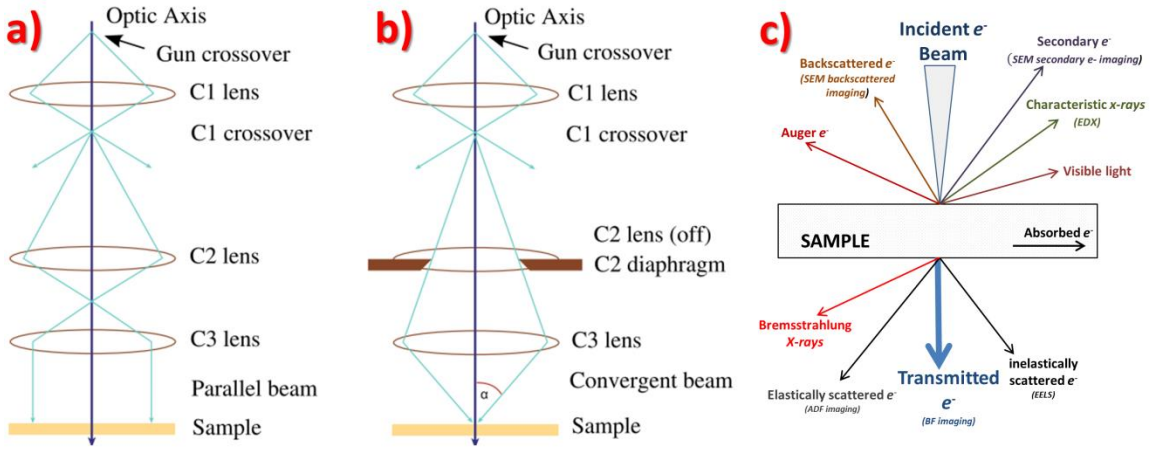

Figure 4 Optical diagram showing the operation of an electron microscope in *a)* parallel (CTEM), *b)* convergent (STEM) modes and the signals generated after the beam-sample interaction. Adapted fr(41).

2.2.1 Probe

The first component of a scattering experiment, in particularly in a TEM is the incident electron beam. Using even a "perfect" optical system, a point of light cannot be focused as a perfect dot. Instead, the image of the probe appear like an Airy disc, consisting of concentric circles with diminishing intensity. The intensity within the first minimum of the airy pattern contains approximately 84 percent of the luminous energy. Additionally, it is impossible to achieve absolute focus with any optical system, because of diffraction and interference effects. Diffraction occurs when a wavefront is impeded by any object: the edge of the lens area constitutes an object, as does any superimposed aperture. In particular, the circular aperture creates the probe with the airy disk shape. The imperfections or aberrations in the objective lens are the primary factor of limitation in the image resolution in CTEM, while in a STEM instrument, the resolution of the scanned image is determined largely by the size of the electron probe,(45) which is not affected by aberrations in the

imaging lenses as a conventional TEM is. Aberrations in the illumination system lenses, however, affect the size of the probe and so aberration correction of the illumination system is important for improving the resolution of STEM images.

When the electron beam passes through real lens, the aberrations fall into two main categories. The first one is spherical aberration, in which off-axis rays are bent more strongly than those passing through the optical axis, causing a point to be imaged as a disk of finite size. The second type of aberration, chromatic aberration, is related to the energy of the electrons. The illumination is not actually monochromatic, but can have an energy spread of between 0.3 - 1.0 eV. Electrons with a lower energy will be bent more by the lens, leading again to a loss of resolution. If, for simplicity, we ignore all non-rotationally symmetric aberrations, the aberration function, which is conventionally expressed as a power series in angle θ, becomes

$$\chi(\theta) = \frac{1}{2}\Delta f\theta^2 + \frac{1}{4}C_s\theta^4 + \frac{1}{6}C_5\theta^6 + \frac{1}{8}C_7\theta^8 + \cdots \qquad (2.1)$$

where Δf is the defocus, C_s, C_5 and C_7 are the coefficient of third fifth and seventh-order spherical aberrations, respectively. All these variables have dimensions of length with positive values for a round magnetic lenses. In a microscope without an aberration corrector, the overriding term in the equation is C_s. (40) The effect of the geometric aberrations are the following. At different angles, the electron rays are brought to different focus points along the optic axis, such a way that a lateral displacement in the Gaussian

focus plane is observed. The gradient of the aberration function gives the amount of sideways translation d as the following

$$\delta(\theta) = \Delta f\theta + C_s\theta^3 + C_5\theta^5 + C_7\theta^7 + \cdots \quad (2.2)$$

The separate contribution of each term in Equation (2.2) on probe size can be seen in Figure 5*a)* for an uncorrected probe as function of the semi-angle θ. The optimum probe sizes are labeled as *A* and *B* for corrected C_3, and C_5, respectively. For example, if one can correct up to C_5, *a ~0.5* Å probe size can be achieved as indicated by point *B*. In Figure 5b), a comparison of STEM probes with and without an aberration corrector at 100 *keV* can be seen. The uncorrected probe has C_s= 1.3 mm, Δf = *694Å* and α_{max}= *10.3 mrad*. The corrected probe has $C_s = \Delta f$ = *0Å* and α_{max}= *25 mrad*, Both curves are normalized to have the same total (integrated) current. It is obviously seen that the advantage of aberration correction is not only a smaller probe, but also stronger peak intensity. In order to achieve a higher signal-to-noise ratio which provides imaging of individual atoms or nanostructures, it is very important.

The current density per unit area and illumination semi-angle determine the brightness as the following

$$B = \frac{I}{\pi A\theta^2} \quad 2.3$$

where *I* is the beam current, *A* is the area of the beam, θ is the illumination semi-angle.

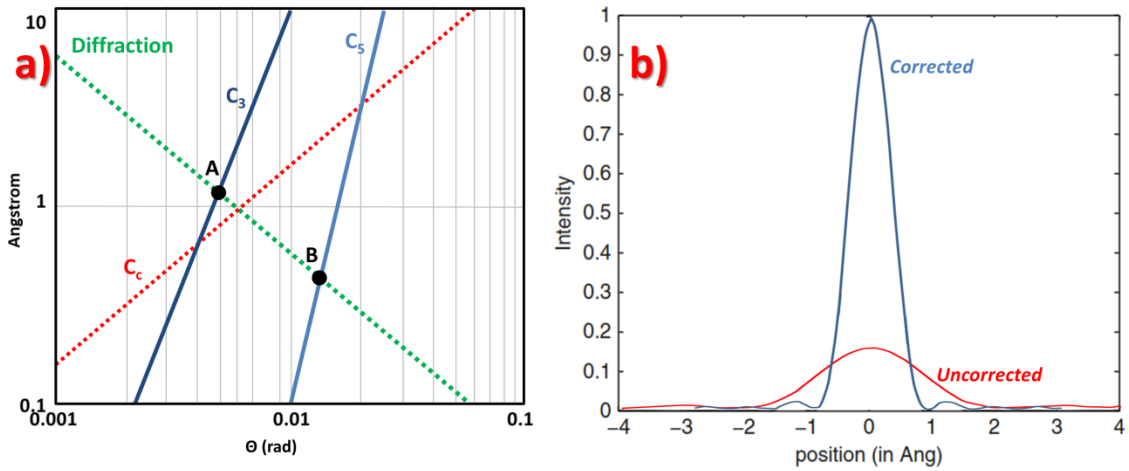

Figure 5 *a)* STEM Probe size as a function of the aperture of semi-angle θ and the aberrations with the diffraction limit. The optimum probes are labeled as *A* and *B* for corrected C_3 and C_5 respectively. *b)* Comparison of STEM probe with and without an aberration corrector at 100 *keV*. The uncorrected probe has Cs= 1.3 mm, Δf = 694Å and α_{max}= 10.3 mrad. The corrected probe has Cs= Δf = 0Å and α_{max} = 25 mrad, Both curves are normalized to have the same total (integrated) current**.** Adapted from (40)

The beam current density in the sample can be increased by a large aperture of the condenser lens or by using a bigger spot size. Increasing the spot size (spot number) leads to increased demagnification of the source and an increased current in the beam. Practically, this leads only a small portion of the emitted beam current to participate to the probe. In the limit, mathematically, zero beam current give us the ultimate spatial resolution. That is to say, the choice of probe size requires the balance between signal-to-noise ratio and resolution. (40)

The electron Ronchigram, a shadow image, referring to the features at the center of the convergent beam electron diffraction (CBED) pattern, is formed by a focused and

stationary electron probe on preferably amorphous material.(46) The Ronchigram provides a convenient way for aligning a scanning transmission electron microscope (STEM). Up to now, all of the commercially available aberration correctors use Ronchigram as part of their alignment procedures (47, 48). The Ronchigram varies considerably with angle, and this variation is a very sensitive function of lens aberration and defocus ((49)) as shown in Figure 6, where Ronchigrams are recorded with *a)* an underfocus, *b)* optimal defocus and *c)* overfocus electron probe on an amorphous specimen when there is no astigmatism. The aberration free region is enclosed by the dashed circle at optimal defocus so that the condenser lens (CL) aperture can select this region to form an aberration free probe.

Typical Ronchigrams are taken from the amorphous edge of a specimen, at a defocus, where the electron cross-over is at a large distance from the specimen along the optic axis and a projection image is observed (50). Axial astigmatism can be very accurately corrected by exciting the stigmator coils so that the Ronchigram features have six-fold symmetry as shown in Figure 6*d), e)* and *f)*. Here, Figure 6*d)* shows induced vertical astigmatism, Figure 6*e)* shows no astigmatism and Figure 6*f)* shows induced horizontal astigmatism. (46) As the beam is focused, the center of the Ronchigram displays the infinite magnification. The coma-free axis is defined by the location of the Ronchigram center and all alignments, detector/aperture positioning are performed with respect to this spot.

At large defocus, when a shadow image at low magnification is visible, Kikuchi lines are also seen on crystalline areas, which can be used to align the specimen’s orientation. If the

corrector is able to correct the higher order spherical aberrations the aberration free central area is expanded.

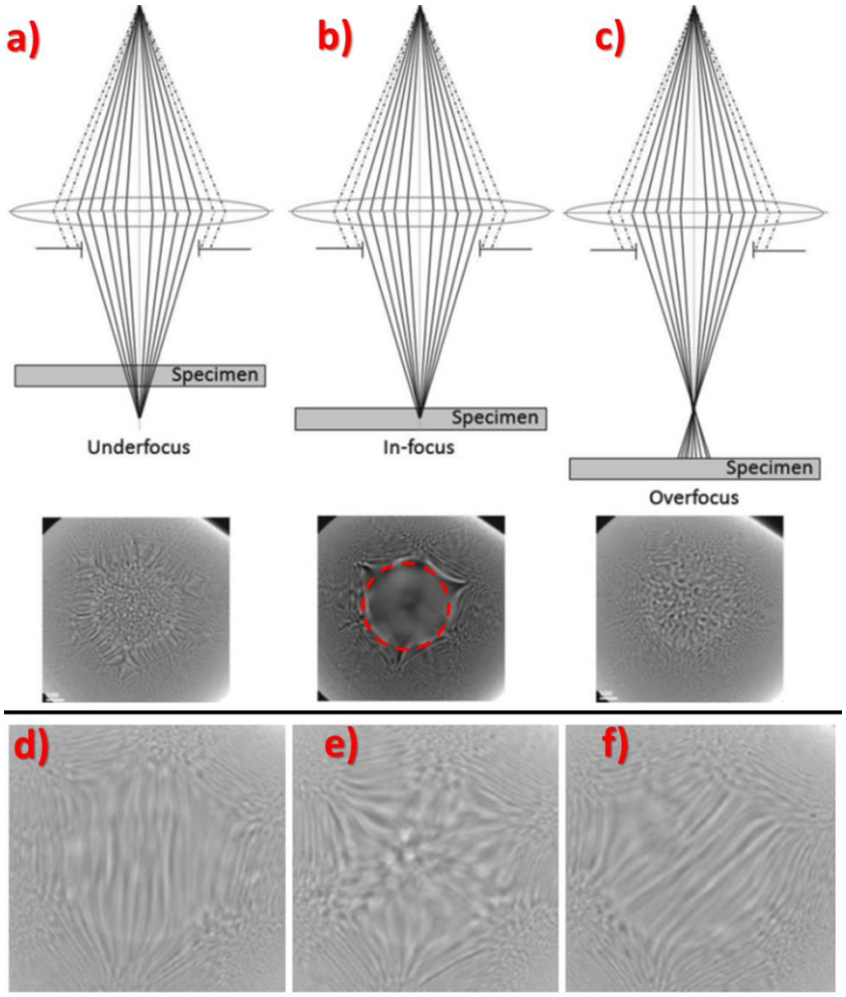

Figure 6 Ronchigrams recorded with *a)* an underfocus, *b)* optimal defocus and *c)* overfocus electron probe on an amorphous specimen. The aberration free region is enclosed by dashed circle so that the CL aperture can pick that region to have aberration free probe. Correction of the astigmatism in STEM; *d)* induced astigmatism by *x*, *e)* no astigmatism and *f)* induced astigmatism by *y*. Adapted from (46)

2.2.2 Interaction

After getting an aberration-free probe, the next important step in a TEM is the interaction between the incident beam, namely the probe, and the specimen. As shown in Figure 4*c)*, the interaction creates different kinds of signal. After interaction with the local atomic potential, some of the incident electrons may be scattered by these interactions, changing the direction of their momentum and often transferring energy to the sample. Elastic scattering involves interaction with the atomic nuclei, and electrons can either be scattered through very high angles, if they approach close to the nuclei, or by small angles, if they pass further from the nuclei. Elastically scattered electrons typically lose negligible amounts of energy. On the other hand, inelastic scattering occurs when the electrons interact with the atomic electrons that surround the nucleus. This interaction can occur with inner-shell electrons, in which case the inner-shell electron can be promoted to an unoccupied state. The energy required for this is typically hundreds or thousands of electron volts (eV) and the incoming electron must lose this amount of energy in order to conserve total energy. The interaction can also occur with outer-shell electrons. Single electron processes typically involve inter-band transitions, for example between the valence and conduction bands across the band gap in a semiconductor or insulator. The amount of energy lost by the beam during the interaction after these excitations or the x-rays created after the excitations can be used for chemical analysis. Electron energy-loss spectroscopy (EELS) and energy-dispersive X-ray spectroscopy (EDX) measures these inelastic scattering events and will be discussed later.

In elastic scattering, the reciprocity theorem was introduced long time ago, which states that the electron intensities and ray paths in the microscope (including a specimen) remain the same if their direction is reversed and the source and detector are interchanged (i.e., the electrons trajectories and elastic scattering processes have time reversal symmetry).(51) It has been pointed out that this implies that bright field CTEM and bright field STEM should produce the same image(39, 52) regardless of the thickness of the specimen. The scattering stems from the coulomb interaction of the electrons with the atomic nuclei in the sample. The negatively charged incident electrons are merely deflected by the relatively high charge concentration in the nucleus due to the small mass of the electron when compared to the nuclei. However, the incident electrons can be scattered through angles of up to 180° while the majority of incident electrons are scattered forward by only a few degrees and thereby contribute to TEM bight field image formation.

2.2.2.1 Diffraction

The basic property of a crystal is that its inner potential, *V(r),* is periodic. We can, therefore, express this potential as

$$V(\vec{r}) = V(\vec{R} + \vec{r}) \qquad 2.4$$

where $\vec{R}$ represents any lattice vector of the crystal and, as usual, $\vec{r}$ represents any real-space vector. Similar to what occurs when waves are scattered from a diffraction grating, diffraction from a three-dimensional periodic structure, such as atoms in a crystal is called Bragg diffraction. It is a consequence of interference between different waves reflected

from different crystal planes. The condition of constructive interference is given by Bragg's law: $n\lambda = 2dsin(\theta)$, where λ is the wavelength, d is the distance between crystal planes, θ is the angle of the diffracted wave, and n is an integer known as the order of the diffracted beam. The scattering distribution is represented by the diffraction pattern. Figure 7 shows the incident beam, scattered by a set of lattice planes, forming a diffraction pattern. The process can be described mathematically by a Fourier transform and is fully reversible. One should keep in mind that Fourier transform of a real image possess more information than a diffraction pattern since Fourier Transform has phase information in complex space in addition to intensity at each diffraction spot. To understand why we use the reciprocal lattice, one should remember that we can always write Braggs law as

$$\frac{2\sin\theta_B}{\lambda} = \frac{n}{d} = |K| \qquad 2.5$$

Thus the vector K is reciprocally related to d and vice versa.(53) In real space, we can define any lattice vector, r_n, by the equation

$$\vec{r_n} = n_1\vec{a} + n_2\vec{b} + n_3\vec{c} \qquad 2.6$$

where n_1 n_2 and n_3 are all integers and the vectors $\vec{a}$, $\vec{b}$ and $\vec{c}$, are the unit-cell translations in real space. Similarly, any lattice vector, $\vec{r}$, in reciprocal space can be written as

$$\vec{r} = m_1\vec{a} + m_2\vec{b} + m_3\vec{c} \qquad 2.7$$

where m_1, m_2 and m_3 are all integers and the vectors $\overrightarrow{a`}$, $\overrightarrow{b`}$ and $\overrightarrow{c`}$ are the unit-cell translations in real space. The following equation gives the directions of these new unit cell translation vectors as

$$\overrightarrow{a`} = \frac{\vec{b} \times \vec{c}}{\vec{a} \cdot \vec{b} \times \vec{c}} \qquad 2.8$$

In general, we can define any vector in reciprocal space in terms of the new unit vector. Particularly $\vec{k}$ can be rewritten as

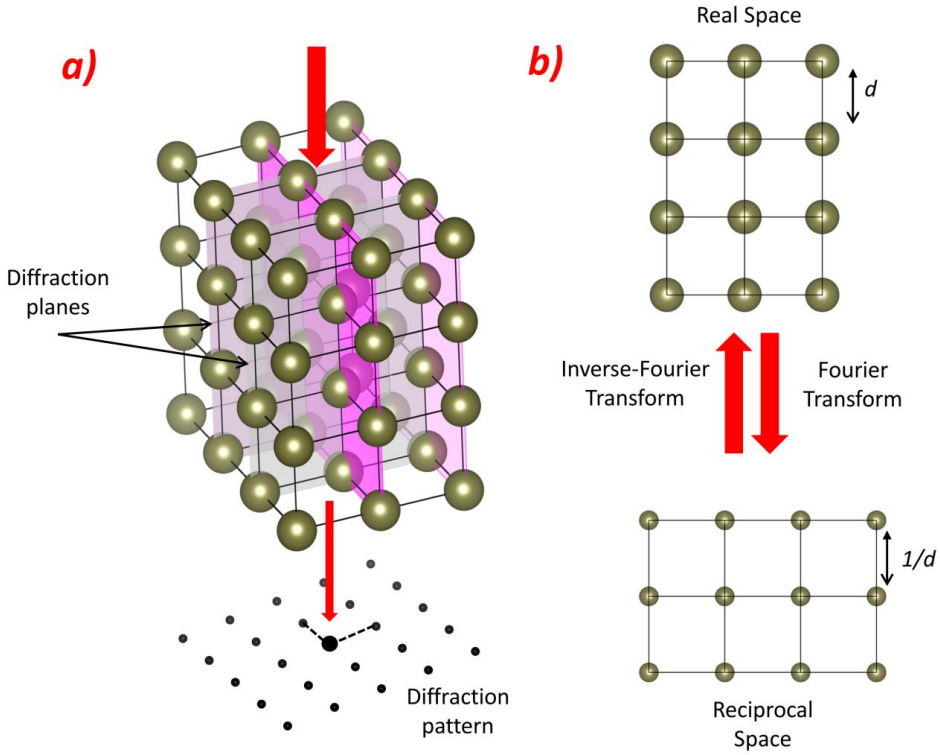

Figure 7 *a)* The Incident beam scattered from the atomic planes creates the diffraction pattern. *b)* Diffraction pattern is a reciprocal space representation of the atomic lattice. The process can be undertaken mathematically by a Fourier transform

$$\vec{k} = \xi\vec{a} + \eta\vec{b} + \zeta\vec{c} \qquad 2.9$$

Here ξ, η and $\zeta \in \mathbb{R}$. Now we can define an important reciprocal lattice vector, $\vec{g}_{hkl}$, as following

$$\vec{g}_{hkl} = h\vec{a} + k\vec{b} + l\vec{c} \qquad 2.10$$

where *h, k* and *l* are all now integers and together define the plane *(hkl).*

One special diffraction condition, which will be utilized during this thesis, should be mentioned here, namely two beam condition. This condition can be achieved by tilting the sample, or the beam, slightly from a zone axis orientation to the direction where only one diffraction spot, namely *g*, is excited in addition to the undiffracted beam. In the two beam condition, we can simplify the math of the scattering and diffraction process. Let`s assume that a plane incident wave, which has a wave function

$$\psi = \psi_0 \, e^{-i2\pi kr} \qquad 2.11$$

is scattered by local atom where ψ_0 is the amplitude and the $2\pi kr$ is the phase. For simplicity, we can apply particular initial conditions and simplify the wavefunction as the following:

$$\psi = \psi_0 \sin(2\pi kz) \qquad 2.12$$

After elastic scattering, the wave function gets an extra phase φ and the total wavefunction becomes as follows:

$$\psi = \psi_0 \sin(2\pi kz + \varphi) = \psi_0 [\sin(2\pi kz)\cos(\varphi) + \cos(2\pi kz)\sin(\varphi)] \quad 2.13$$

If φ is small, we can take $cos\varphi \sim 1$ and $sin\varphi \sim \varphi$. Then the total wavefunction can be written as

$$\psi = \psi_0 \sin(2\pi kz) + \psi_0 \varphi \sin\left(2\pi kz + \frac{\pi}{2}\right) \quad 2.14$$

Therefore, the total wavefunction after scattering can be interpreted as linear combination of two wavefunctions, namely undiffracted beam and diffracted beam, which has a relative phase shift π/2 with respect to undiffracted beam.

After incident beam and the interaction between the sample and the beam, I will next talk about the detection of the final states of the elastic and inelastic scattering experiment occurring in the electron microscope.

2.2.3 Detection

2.2.3.1 STEM imaging

Multiple signals can be acquired simultaneously in a STEM, including high angle annular dark field (HAADF) images, low angle annular dark field (LAADF) image, annular bright field (ABF) image and spectroscopic images using the inelastically scattered electrons. Figure 8a) gives a schematic representation of the direct and scattered beams emerging from the sample in a STEM. The direct beam is composed of electrons that emerge from the sample at relatively small angles. These electrons pass directly through the hole of the ADF detector and are detected using the BF detector directly behind. On the other hand, the electrons scattered from a heavier nucleus to higher angles, which is detected by an annular detector, called the high angle annular dark field (HAADF) detector. At high scattering angles, the cross section depends directly on the atomic number, Z, and images created by this signal as called Z-contrast images.

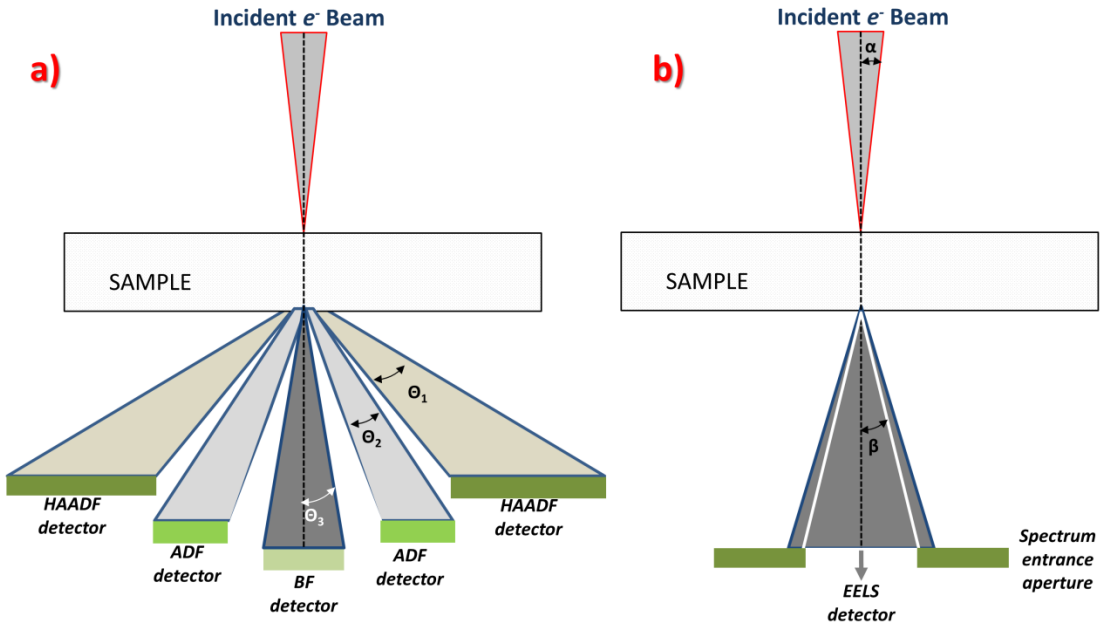

Figure 8 a) Schematic of the HAADF detector setup for Z-contrast imaging in a STEM. The conventional ADF and BF detectors are also shown along with the range of electron scattering angles gathered by each detector. b) Schematic diagram showing the setup of EELS data acquisition which indicates the convergence angle α, the collection angle β and the spectrometer entrance aperture. Adapted from (41).

2.2.3.2 High-angle annular dark-field (HAADF) imaging

The HAADF signal, typically spanning 80–200 mrad collection half-angle, is used to locate heavy atoms and to generate a map of the local atomic number. Additionally, the low-angle ADF signal (LAADF), typically 40 to about 80 mrad, can be used to probe elastic strains in crystalline samples. Decreasing the inner detector angle of the HAADF detector to 50 mrad gives stronger signal from light atoms in ultra-thin samples. At sufficiently large inner detector angle, the intensity in the image is related to the local atomic column composition in a simple fashion, namely Z^n, where Z is the atomic number and n is a constant ranging from 1.6 to 2 for different collection conditions [(54), (55)]. The HAADF

signal is incoherent and depends only atomic number of the illuminated atomic column. Therefore, the Z-contrast image contrast decreases monotonically with specimen thickness, only due to beam broadening,(56, 57) which makes them straightforward to interpret.(58), (59), (60), (61), (62). In contrast, the contrast in conventional phase contrast high-resolution imaging consists of a combination of diffracted beams emerging from the sample, resulting in interference effects that depend on sample thickness and local defocus. CTEM images are not directly interpretable and extensive image modeling is required. Finally, using the same aberrations and acceleration voltage, the incoherent Z-contrast image can provide a ~30% better spatial resolution compared to coherent CTEM imaging(56).

2.2.3.3 Annular Bright Field (ABF) imaging

Light elements like oxygen, carbon, nitrogen, even hydrogen, are difficult to identify in HAADF images due to their low atomic numbers and screening effects from neighboring heavy elements. As discussed earlier, HAADF images shows atomic columns as bright spots over wide ranges of probe-forming lens defocus and sample thickness (63). On the other hand, traditional BF imaging suffers from contrast reversal due to changes in the phase of the exit wave which depends on the specimen thickness or objective lens defocus.

ABF imaging it is a powerful complementary technique to HAADF imaging, since it allows for light elements to be imaged in a largely incoherent imaging mode. Moreover, the detector geometry allows for simultaneously data acquisition with HAADF images (64) (65-67). However, the ABF image is not as robust to defocus as to thickness. Figure 9

shows an ABF defocus-thickness map for $SrTiO_3$ viewed along the [011] direction. This map shows range of images centered around zero defocus where the image contrast does not change as a function of sample thickness. However, the range of defocus values defining this band is very narrow, extending to around ±40 Å((66), (68)). Beyond that, the residual aberrations (C_s) create obvious image artifacts. Another problem one should consider is that ABF images are very sensitive to the relative detector position. If the ABF detector is not centered properly, especially for the light elements, there is an artificial displacement of the atomic positions of light elements, as seen in Figure 10.

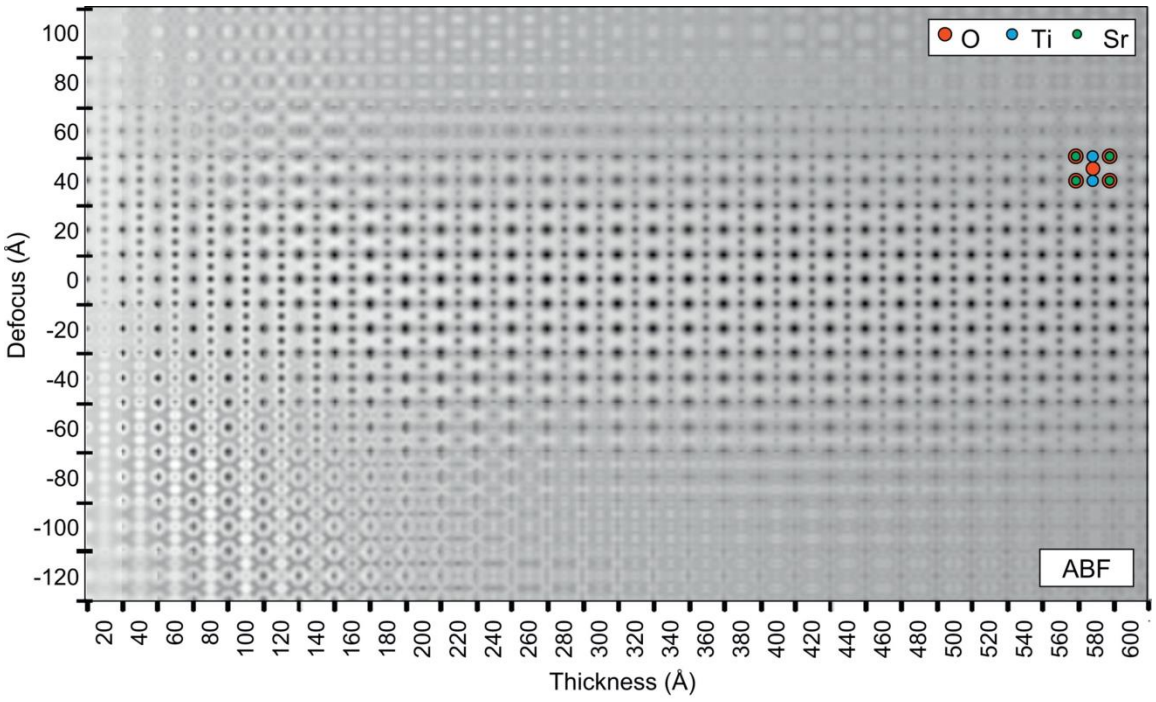

Figure 9 Simulated defocus-thickness map for ABF imaging of $SrTiO_3$ viewed along the [011] orientation. Taken from (66)

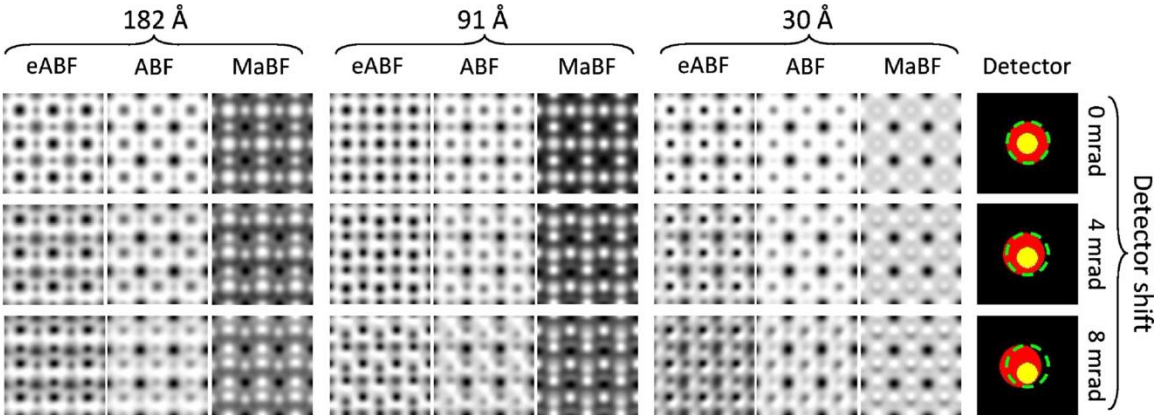

Figure 10 Middle angle bright Field (MaBF), ABF and the difference between the ABF and MaBF images(eABF) images of $LaAlO_3$ in [001] orientation for different thicknesses, exploring the effect of miscentering the detectors. The first row assumes perfectly centered detectors, while the second and third rows assume displacements of magnitude 4 mrad and 8 mrad, respectively. Taken from (69)

Next, I will discuss inelastic scattering, which can be utilized for elemental chemical maps and for acquiring information about the local density of states.

2.2.3.4 Inelastic scattering and electron energy-loss spectroscopy

Inelastic scattering is the foundation for electron energy-loss spectroscopy in a transmission electron microscope. As the beam of electrons passes through the sample, inelastic interactions occur with the inner shell core and outer shell atomic electrons. An incident electron with an initial energy E_0 and momentum P_0 can be scattered through a characteristic angle θ losing momentum ΔP and energy ΔE as it passes through the sample. As the initial beam energy was known, the amount of energy lost in the sample can be determined for each electron. An analysis of this distribution can yield information about the chemical composition since the excitations of electrons from the inner shell to outer unoccupied shells require well-known energies that depend on the particular element and bonding.

The main limitations of the accuracy of EELS is that we assume the incoming beam from the electron gun is mono-energetic, so that we can subtract the final energy from the initial one and we also assume that each incoming electron inelastically scattered by the atomic orbitals once. The first problem can be solved by a better gun, such as cold field-emission or monochromatic electron source. (70) However, even with commercially available TEM monochromators, the energy resolution is still not good as that achieved in EXAFS. (71) Using a cold field-emission gun, 0.35 *eV* energy resolution at 200 KV can be achieved while a monochromatic corrector can push the resolution up to 12 *meV* at 60 *kV*. (70) To avoid the second problem, namely multiple scattering, one needs to have samples thin enough.

Another thing to consider for EELS data acquisition is the convergence semi-angle, α, and the collection semi-angle, β, as seen in Figure 8b). The detailed intensity variations in the spectrum depend on the range of electron-scattering angles gathered by the spectrometer. Experimentally, the scattered electrons distribute wider when the collection semi-angle, β is equal to or smaller than α, This condition may lead a limitation in the accuracy. To avoid this, the collection angle β should be large enough. The collection angle β can be adjusted by changing the camera length or using different size of the spectrometer entrance aperture. On the other hand, a large entrance aperture, while it results in high spectrum intensity, will also degrade the energy resolution as a result of residual spectrometer aberrations at high angles. There is a characteristic or most probable scattering angle, namely $\theta_E = E_{edge}/2E_0$, where E_{edge} is the specific energy loss and E_0 is

energy of incoming beam. Using an entrance aperture large enough to satisfy $\beta > 2 \cdot \theta_E$ provides scattering angle independent spectrum (41)

.

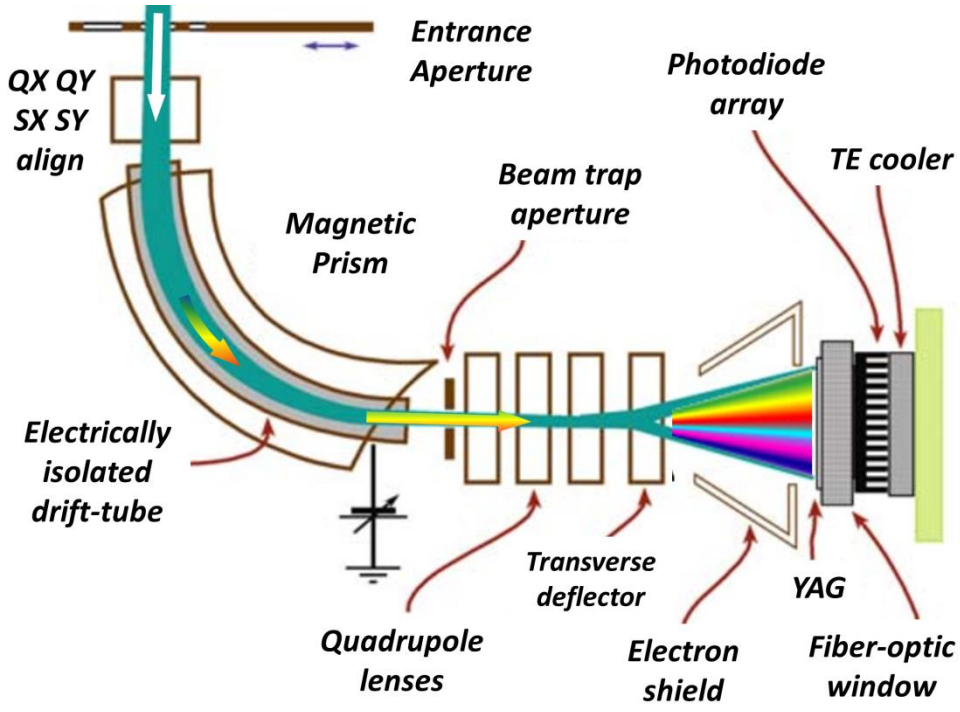

Figure 11 Cross-section through an EELS spectrometer. Adapted from (41)

2.2.3.5 The EELS Spectrometer

The cross-section of an EELS spectrometer is shown in Figure 11. Starting from the top of the diagram, multiple entrance apertures with different sizes (in general from 1 mm to 5 mm) can be used to limit the collection angle and also to lower the aberration. Due to the complex arrangement of the electron optical lenses, the spectrometer also suffers from lens aberration similar to those discussed earlier for the probe forming illumination system. The

proper aperture size will serve to limit the angle subtended by the spectrometer with respect to the objective lens cross over and thereby minimize the effects of aberrations on the spectrometer resolution. Generally, the energy resolution will increase with decreasing entrance aperture diameter. However, decreasing the size of entrance aperture will also increase the noise content in the spectrum due to the low electron intensity. The addition of quadrupole lenses at the exit side of the spectrometer allows us to vary the dispersion electronically. The electrons with different energy are dispersed in the magnetic prism according to the electron energy by using the QX, QY, SX, SY alignment coils and then focused into different lateral positions in the image plane defined by the optical system behind the prism. The quadrupole lenses can be used to focus the dispersed electrons onto a fiber-optically coupled yttrium aluminum garnet (YAG) scintillator. The kinetic energy of the fast electrons is absorbed by the scintillator materials and converted to visible or ultraviolet light. When the light strikes the charge-coupled device (CCD) surface and the counts are periodically read into a computer by the Digital Micrograph software package, which is used to control the automatic EELS acquisition, including qualitative and quantitative analysis.(72)

2.2.3.6 Spectrum imaging

In STEM mode, the fine probe scans across the sample while at each pixel the transmitted beam is passed through a spectrometer and a complete spectrum can be recorded. The spectrum image cube is then constructed column-by-column, as seen in Figure 12. This

way, imaging and EELS spectroscopy can be performed simultaneously using the ADF detector. Additionally, this allows for spectra to be compared directly to images, but it also provides a means for recording, correcting sample drift and improving spatial resolution. On the other hand, because of the strong focused beam to a point, the beam damage can be more significant.

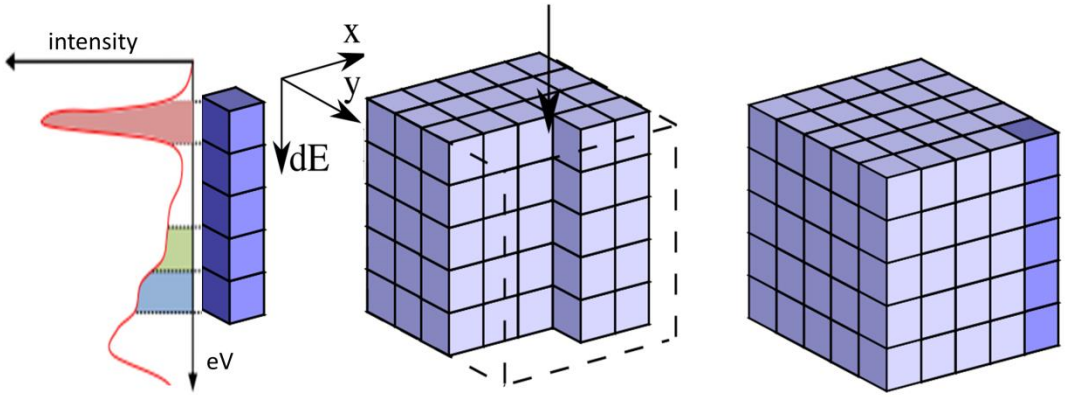

Figure 12 A spectrum image with x and y dimensions corresponding to the spatial dimensions in the sample and the z dimension (*dE*) being to the energy loss. Each column of pixels contains an entire energy loss spectrum and by scanning through the spatial *x* and *y* directions builds up the entire spectrum image in STEM mode

2.2.3.7 Electron Energy Loss Spectroscopy

The EEL spectrum can be sub-divided into three regions corresponding to different forms of excitation namely the valence band (low loss) region, the core loss (high loss) region and the zero loss peak. A characteristic EEL spectrum is seen in Figure 13. If the microscope gun creates a beam with 200,000 eV energy, the strongest peak, "zero-loss peak", is the result of the inelastically scattered electrons which do not lose any energy while passing through the specimen where the energy resolution can be found by the sharpness of this peak. The next feature is the "first plasmon peak," triggered by the

excitation of one plasmon in the sample at the energy loss *E = 25 eV*, which is detected by the electrons hitting the detector with energies of 199,975 *eV*. Increasing the thickness of the specimen may lead multiple scattering which excites multiple plasmons and peaks at multiples of 25 eV. The next feature is a Ni M_{23} absorption edge caused by the excitation of *3p* electrons out of Ni atoms at 68 *eV* is not a plasmon peak, but rather a core loss. Another core-loss excitation is O *K* absorption edge at 532 *eV* caused by the excitation of 1*s* electrons to unoccupied orbitals above Fermi level. The background in the EEL spectrum falls rapidly with energy (power law). At 855 eV, another excitation of Ni, the excitation of $2p^{3/2}$ electrons to outer empty orbitals can be seen in Figure 13 which is called the L_3 edge. Similarly, the next edge at 872 *eV*, namely, L_2 edge stems from the excitation of $2p^{1/2}$electrons out of the atom. These two peaks are called *white lines* and these excitations are very typical for transition metals.

Ionization edges are characteristic for each element, and depend on the crystallographic orientation or specific bonding state of the atoms. Moreover, the ionization edges display fine structure, known as energy-loss near-edge structure (ELNES), which can be explained in terms of the density of states (DOS) of the atom. The inner shell electrons do not excite to the empty outer orbitals with equal probabilities. Some available outer orbitals can be filled easier than others because of the higher number of states within certain energy ranges than in others. Therefore, the density of states (DOS) is the distribution of unfilled energy levels. The greater ELNES intensity is the indication of the greater probability of electrons exciting into certain unoccupied states, high DOS regions, above E_F. (In in Figure 14. E_F can be considered as the critical ionization energy E.)(41)

In transition metals and rare-earth metals which have high DOS just above the Fermi level, excitation into empty *d*- and *f* –states creates sharp features unlike many other absorption edges. This sharp features are the result of the dipole selection rule which dictates that the change in the angular momentum must be l=±1ħ. Because of the dipole selection rule, the intense white lines at L_{23} edges of transition metals with empty *d*-states, is observed which include transitions from core p-electrons, unlike L_1 edges, which involve excitations from s-electrons(38).

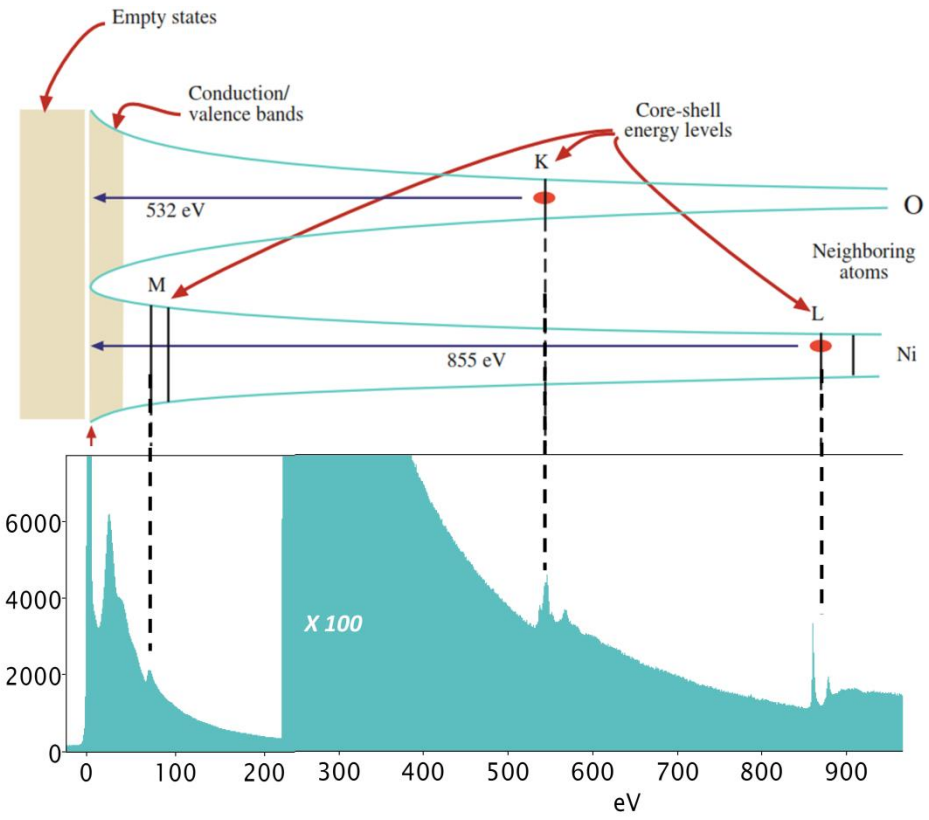

Figure 13 The relationship between the energy levels of electrons and the energy-loss spectrum is shown. The more energy is required to excite the electrons in the deeper potential well. The ZLP is above E_F, and the plasmon peak is at the conduction/valence bands To excite the electron from a particular inner shell, a critical ionization energy should be provided such as Ni L: 855 eV and O K: 532 eV. Adapted from (41)

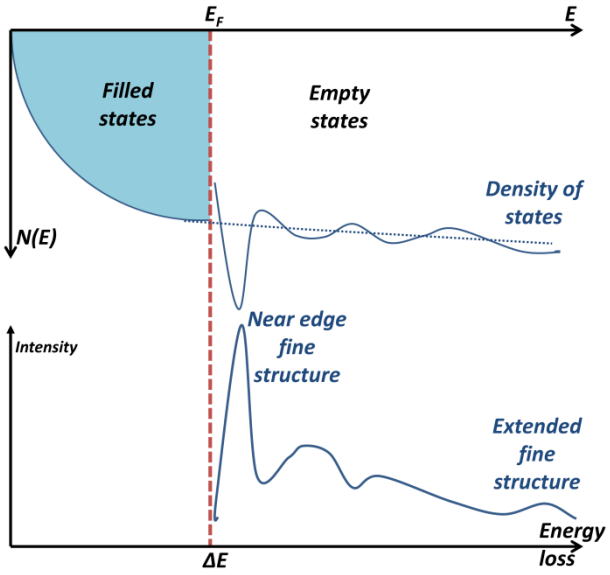

Figure 14 Relationship between the empty DOS and the ELNES intensity in the ionization edge fine structure. Adapted from (41)

2.2.3.8 Valance and Magnetic measurement in EELS

Since EELS probes the unoccupied orbital just above the Fermi level, any change on the Fermi surface, stemming from structural, electronic or magnetic changes, can be seen in the EELS signal. As a result, a plethora of information can be obtained from the dependence of the inelastic signal as a function of specimen orientation, and from the angular dependence of scattering. (73-75)

In this thesis, I concentrate on valance state and spin state transitions in transition metal oxides (76-79). For examples, in EELS, the Pr valence state can be determined using the M_5 edge at 931 *eV*, and the M_4 edge at 951 *eV*. More specifically, the fine structure in Pr^{3+} has a clear bump before M_4 edge. As the oxidation state of Pr increases this bump gets weaker and eventually disappears as the Pr valence state approaches 4+.*(26)*

Another very common method to determine the valance state of transition metals is the white line ratio. Transition metal L_2 and L_3 edges stems primarily from transitions of $2p^{3/2}$ and $2p^{½}$ core-shell electrons into unoccupied 3*d* orbitals such that *2p* core hole which has an orbital angular momentum *L=1* which then couples to the spin angular momentum *S=1/2* to produce *J = 3/2* and *J=1/2* final states which are directly observable in the *L-edge* spectrum as the two main peaks namely L_3 and L_2(80). Moreover, L_3/L_2-ratios can identify different oxidation states. If one considers only the occupancy of the initial states, then L_3/L_2-intensity ratio, white line ratio, should always be two, namely *4/2=2*. On the other hand, as a result of spin-spin coupling, the occupancy of the final 3*d* orbital alters the probability for the $2p^{3/2}\rightarrow 3d$ and $2p^{1/2}\rightarrow 3d$ transitions, respectively, and therefore, results in different L_3/L_2-ratios for different oxidation states. For different transition metals, the white-line ratio across the 3*d* series increases with *d* occupancy when $n_d<5$, and decreases when $n_d>5$,(79) as shown in Figure 15*a).* However, the corrected white line ratio and the *d* orbital population have an inverse relationship, as shown in Figure 15b*).* Another very interesting feature in transition metal oxides is shown in Figure 15*c)* (81). As the valance state of Co increases, the white line ratio shows an exponential decrease. However, results shown at the end of this thesis begin to cast some doubt on this traditional analysis of the transition metal valence using the white line ratio if an electron probe is used that is smaller in diameter than the interatomic spacing. It appears that the white line ratio depends very sensitively on the electron probe position and a detailed description of this new phenomenon is given in Chapter 6 of this thesis.

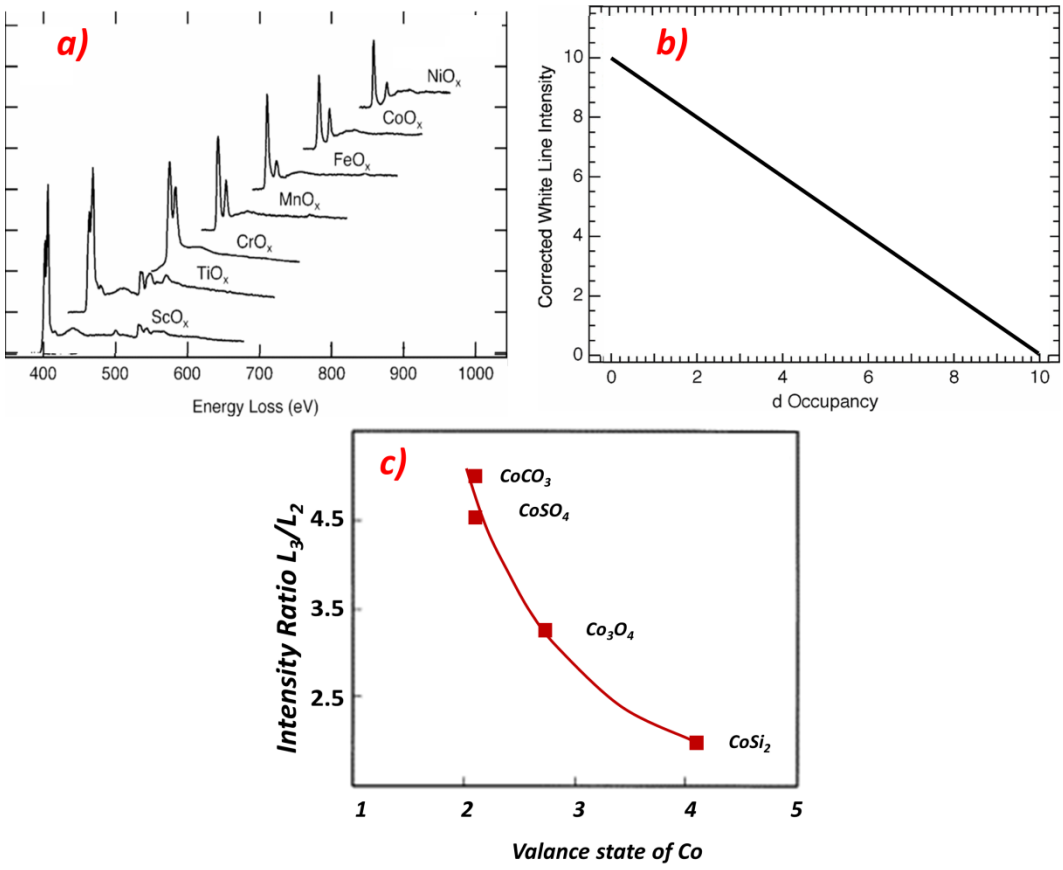

Figure 15 Energy-loss spectra of the transition-metal $L_{2,3}$edges from *a)* a series of transition-metal oxides and *b)* Normalized white-line intensity for a series of transition metals vs averaged *d* occupancy ,adopted from (79). Plots of the intensity ratios of L_3/L_2 calculated from the spectra acquired from: *c)* Co compounds as a function of the cation valence. A nominal fit of the experimental data is shown by a solid curve. Adopted from (81)

2.2.3.9 Electron Energy-Loss Magnetic Circular Dichroism (EMCD)

When an atomic electron is excited by an electron beam, the excitation occurs from filled inner shell orbitals to unoccupied outer shell orbitals above the Fermi level. With the proper detection ability, we can now probe the states above Fermi level or the occupied outer shell. If we had control over additional incident beam properties, such as angular momentum, spin, helicity, it would be possible to study properties of the initial state of the specimen.

One good example is x-ray magnetic circular dichroism (XMCD) spectroscopy, which probes spin and orbital quantum numbers in such a way that two photon beams having opposite circular polarization are used in a magnetic field. In transition metals, the *d* valence shell can hold up to 10 electrons, which are filled up to the Fermi level and the number of filled states is therefore *10–N,* where *N* is the number holes. For a magnetic material the *d* shell has a spin moment which is given by the imbalance of spin-up and spin-down electrons or equivalently (except for the sign) by the imbalance of spin-up and spin-down holes. Since spin flips are forbidden in electric dipole transitions, spin-up (spin-down) photoelectrons from the *p* core shell can only be excited into spin-up (spin-down) *d* hole states, in order to measure the difference in the number of *d* holes with up and down spin, we need to make the x-ray absorption process spin dependent. This is done by using right or left circularly polarized photons which transfer their angular momentum to the excited photoelectron. The photoelectron carries the transferred angular momentum as a spin or an angular momentum, or both. If the photoelectron originates from a spin-orbit split level, e.g. the $p_{3/2}$ level (L_3 edge), the angular momentum of the photon can be transferred in part to the spin through the spin-orbit coupling. Right circular photons (RCP) transfer the opposite momentum to the electron as left circular photons (LCP) photons, and hence photoelectrons with opposite spins are created in the two cases. Since the $p_{3/2}$ (L_3) and $p_{1/2}$ (L_2) levels have opposite spin-orbit coupling, the spin polarization will be opposite at the two edges. If we subtract the edge intensity of both spectra, the XMCD signal can be acquired as seen in Figure 16.(82)

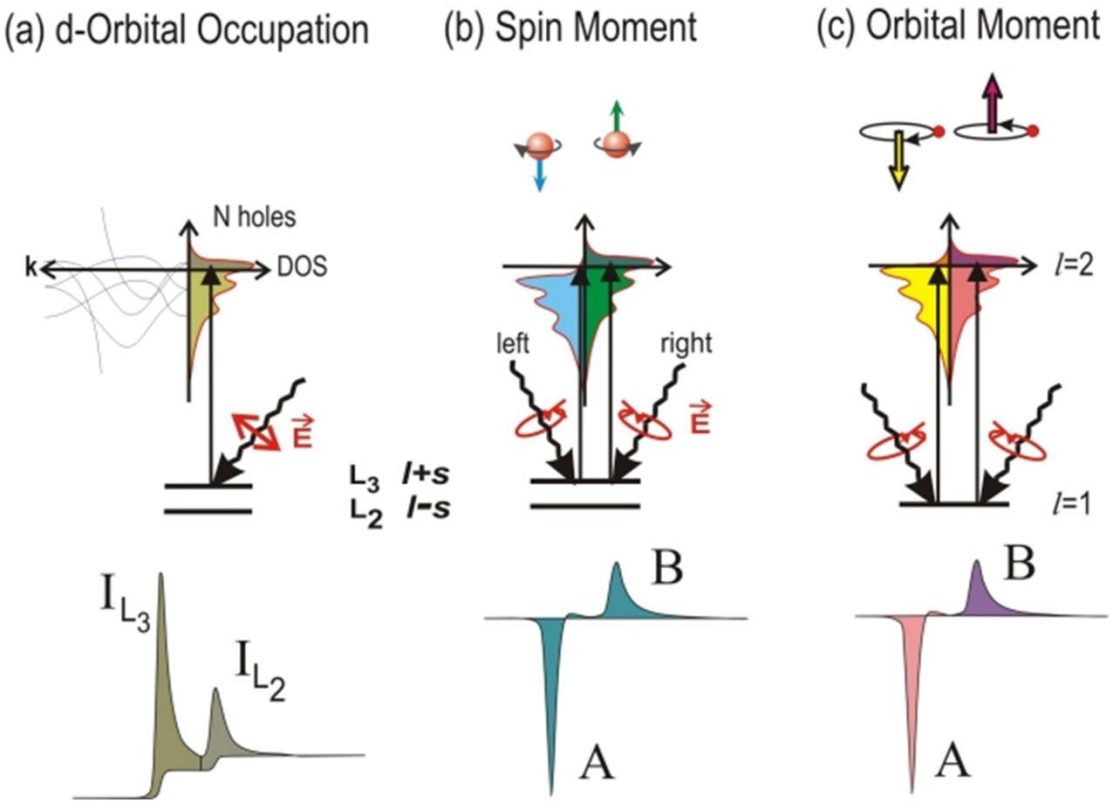

Figure 16 a) Electronic transitions in conventional L-edge X-ray absorption, (b) and (c) X-ray magnetic circular dichroism, illustrated in a one-electron model. The transitions occur from the spin-orbit split 2p core shell to empty conduction band states above the Fermi level. In conventional X-ray absorption the transition intensity measured as the white line intensity $I_{L3}+I_{L2}$ is proportional to the number of d holes, *N*. By use of circularly polarized X-rays the spin moment (b), and orbital moment (c), can be determined from the dichroic difference intensities *A* and *B.* Adapted from (82)

In light optics, creating circular polarized beam is trivial. However, in electron microscopy we need to follow a harder path to achieve the polarized electron beam with nonzero angular momentum. One way to do it is by using an electron vortex beam aperture which generates an electron beam with a phase singularity propagating in free space, by passing a plane electron wave through a spiral phase-plate.(83) However, this method lowers the beam current dramatically and it has been reported that the dichroic signal is undetectable for nanoparticles smaller than ~1 nm (84). Another alternative approach has been recently

explored, using an aberration corrector to manipulate the rotational symmetry of the electron probe phase to obtain an EMCD signal (85). The method I will use in my PhD research is different from either approach and was introduced by Schattschneider (86).

The conditions required by circular polarization are i) two coherent, ii) mutually perpendicular electron beams where the phase is iii) preferably shifted by $\pi/2$. Using a sample in the two beam condition, two diffraction vectors are excited, namely the central [000] spot and the first diffracted spot g with a phase shift $\pi/2$, as seen in Figure 17. The area labeled *-1* on the *Thales circle* is the spot where there are contributions from non-diffracted central spot, (000), q_1, and from the diffracted spot, q_2, are mutually orthogonal in momentum space. At this particular spot, the incoming beam acts like a circularly polarized beam, as seen in Figure 17*b)*, since the momentum transfer vectors, which are parallel to electric field, are perpendicular and we can assume that they have a phase shift of $\pi/2$, as discussed in chapter 2 with a simplest model. On the other hand, if we move to opposite side on the *Thales circle*, the +1 position, everything but the directions is the same which makes the beam acts like having opposite circular polarization. The magnetic signal is contained in the difference of the L edge intensities which are acquired from these two spots. In order to substract two spectra properly, first, the background signal at the pre-edge region should be subtracted from both spectra in a same manner. Background signal generally looks like the power-law function of AE^{-r}, in which E represents the energy loss, A and r are the fitting parameters. After two spectra are normalized, by the integration of the intensity in a post-edge window, they can be subtracted from each other to get the proper EMCD signal.

In addition to simplest model, suggesting scattering electron beam from a single electron as discussed in Chapter 2, more realistic model suggests a more complicated situation for EMCD signal intensity. In the Bloch wave approach, the intensity of the diffraction spots oscillates over the thickness of the specimen as a result of overlapping Bloch waves, which changes the expected phase shift. To understand the effect of the thickness and the tilt angles, the EMCD signal intensity is calculated by using the Bloch wave simulation code developed by Löffler and Schattschneider (87). The EMCD signal as a function of thickness of $La_{0.7}Sr_{0.3}CoO_3$ in two beam condition which is achieved by tilting the sample from pseudo-cubic [011] zone axis through the direction of pseudo-cubic $[2\bar{1}1]$ orientation is shown Figure 17d). Taking into consideration of the minima at the thickness around 30 nm, we can achieve to acquire dichromatic signal for this particular sample.

Since the first paper by Schattschneider, several other EMCD geometries have been suggested, such as the 3 beam symmetric case (88), the energy spectroscopic diffraction (ESD) (89), (E,q) spectra, (90), LACDIF (Large-Angle Convergent DIFfraction) (91), and STEM EMCD.(92) The general principle of all those methods is, however, the same. (42)

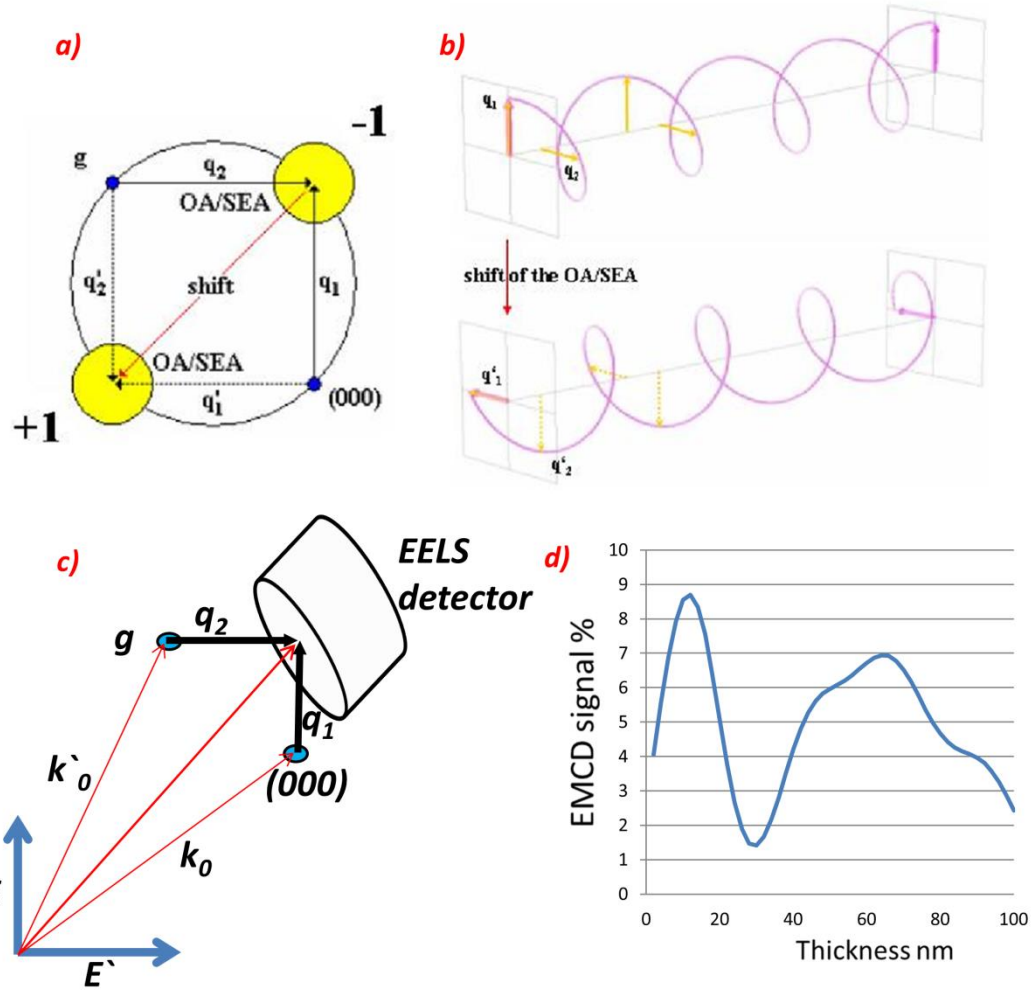

Figure 17 EMCD standard geometry. Adapted from [42].

2.3 JEOL JEM-ARM200CF

The JEOL JEM-ARM200CF is equipped with a spherical aberration corrector for the probe forming electron optical system, which now routinely provides an image resolution of 70 pm spatial resolution. The cold field emission electron source allows for a 350 *meV* energy-resolution in the energy range between 80-200 kV, using a 1 μA beam current and the

Gatan Enfina post-column EELS spectrometer. For EDX analysis the JEOL ARM200CF is equipped with a windowless Oxford X-max 100TLE SDD X-ray detector. Five different STEM image detectors allow for simultaneous acquisition of HAADF, LAADF and ABF images. Figure 18 shows an ABF image of $La_{0.95}Sr_{0.05}CoO_3$ in the pseudo-cubic [110] orientation, and the corresponding FFT as an insert, which clearly contains the $[\bar{1}1\bar{5}]$ peak, corresponding to a spatial resolution of 89 pm.

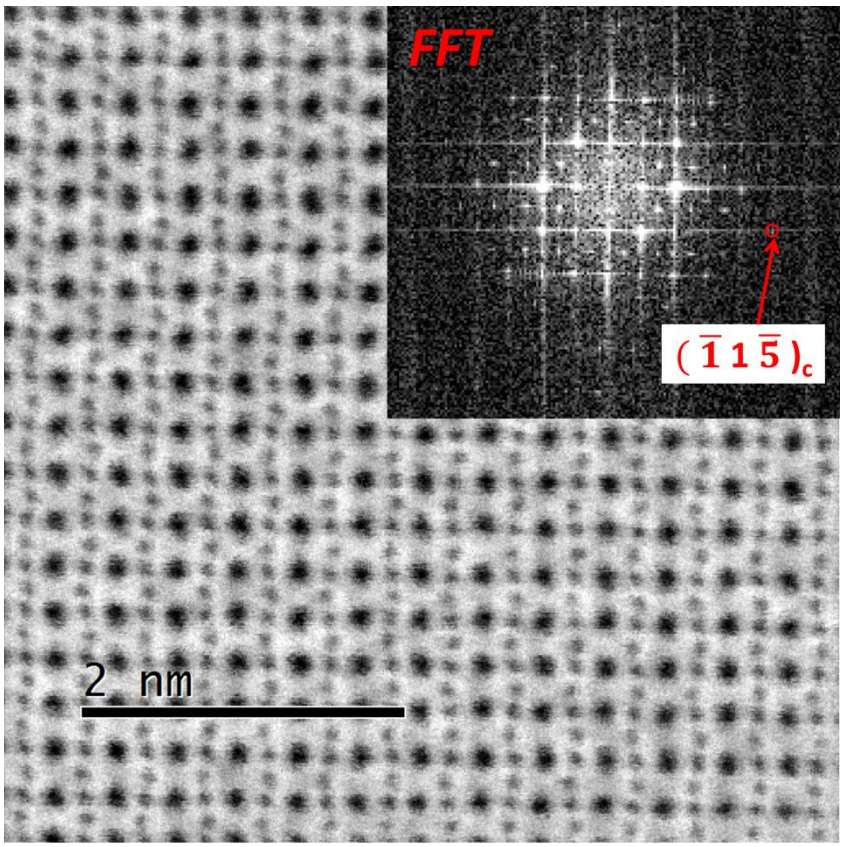

Figure 18 ABF image of $La_{0.95}Sr_{0.05}CoO_3$ in pseudo-cubic [110] orientation taken at JEOL JEM-ARM200CF at UIC with FFT inserted where [$\bar{\mathbf{1}}$ 1 $\bar{\mathbf{5}}$] spot is visible

2.4 Cooling stage

For *in-situ* cooling experiments, the Gatan Liquid Nitrogen (LN_2) double tilt sample stage is used, while maintaining atomic-resolution imaging conditions at liquid nitrogen temperatures. The Gatan 636 cold stage is cooled using a well-insulated liquid nitrogen dewar. Precise temperature control of the specimen is achieved through a conductor rod connecting the specimen holder to the LN_2 dewar. Excellent thermal contact between the specimen and the beryllium specimen cradle is achieved using beryllium washer. For better stabilization, the dewar needs to be connected to vacuum pump and baked at 373 K for two hours to reach low pressure of dewar insulation before the holder is installed to microscope. Prior to image acquisition, the LN_2 holder was allowed to stabilize for 4-5 hours to reach thermal equilibrium after initial cooling. The lowest temperature indicated by the thermo-couple of the double tilt holder is 85 K. Due to the thermal instabilities and sample drift, any experiment between room temperature and that minimum temperature is extremely difficult to achieve. Atomically resolved images can only be acquired if the samples are allowed to reach thermal equilibrium.

3 SPIN STATE TRANSITION OF $La_{1-x}Sr_xCoO_3$

Primarily due to their exceptional magnetic transitions which are related to changes in the Co^{3+}-ion spin states, $LaCoO_3$-based perovskite oxides have been studied for a long time. More specifically, bulk $LaCoO_3$ shows two temperatures dependent transitions occurring below 100 K and above 500 K. Below 100 K, bulk $LaCoO_3$ exhibits nonmagnetic behavior while after the first transition it becomes a semiconducting insulator and after the second transition above 500 K, it turns metallic.(4, 93) Both transitions are believed to be the result of changes in the Co-ion spin states. These spin states transitions are related to the competition between the crystal-field splitting (Δ_{CF}) of the Co *3d states* into e_g and t_{2g} orbitals, which encourages the lower spin states, and the Hund's exchange rule, which is responsible for higher spin configurations. The first magnetic transition is believed(4),(5),(6) to be due to a change in the Co^{3+}-ion spin state from a LS ($t^6_{2g}\, e^0_g\, S=0$) state to combination of the HS ($t^4_{2g}\, e^2_g\, S=2$) and LS states(7) or alternatively an IS ($t^5_{2g}\, e^1_g\, S=1$) state.(8, 9),(94) The high-temperature transition stems from a change in the Co^{3+}-ion spin-state to a HS state. Due to the relatively small difference between the crystal-field splitting energy (Δ_{CF}) and the intra-atomic Hund`s rule exchange energy, magnetism can be tuned in various ways including: i) changing the grain size of powder sample(10), ii) epitaxial tensile strain via the properly chosen substrate,(11, 12) iii) external pressure(13, 14) or iv) doping with an alkaline rare-earth ion, such as Sr, having a different ionic radius.

Bulk $La_{1-x}Sr_xCoO_3$ (LSCO) has been intensively studied by various techniques, such as extended x-ray absorption fine structure (EXAFS), Neutron Pair Distribution Function (PDF)(15), NMR(16, 17), Small-Angle Neutron Scattering (SANS)(18), and Inelastic Neutron Scattering (INS), Electron Spin Resonance (ESR)(19). It was reported that with increasing Sr-doping concentration, $La_{1-x}Sr_xCoO_3$ changes from a non-magnetic insulator which undergoes a thermally induced Co^{3+} ion spin state transition at low temperature, to a spin glass at low Sr-doping and a ferromagnet at higher doping. As the Sr-doping concentration increases, spin polarons which are caused by substituting divalent Sr^{2+} ions for trivalent La^{+3} ions merge and form short-range FM clusters, since the neighboring mixed valance Co ions interact ferromagnatically via double exchange mechanism(17). At the critical doping of $x \approx 0.17$, the clusters percolate, leading to a crossover from short- to long-range FM and the system simultaneously undergoes a percolative insulator-to-metal transition (IMT)(17).

Using EXAFS and neutron PDF measurements, *Sunduram et al.(15)* reported large Jahn-Teller distortions of the Co-O bond in Sr-doped $LaCoO_3$ samples with doping concentrations as high as 35%. However, intermediate spin states, corresponding to the presence of singly occupied Co e_g orbitals was not observed. *Smith at al(16, 17)* utilized NMR and theoretical modeling to show that the Co ion spin state transition coincides with nanoscale hole–poor regions of the inhomogeneous doped $LaSrCoO_3$. For lightly hole doped $LaCoO_3$, *Podlesnyak et al(19)* conclude that INS, ESR and NMR data provide evidence for two regimes, one dominated by spin polarons at low temperature and one by thermally activated magnetic Co^{3+} dominated at higher temperature. However, all these

studies mentioned above rely on probe sizes that are significantly larger than the nano-scale feature they are trying to characterize. Aberration corrected transmission electron microscopy can provide sub-Angstrom spatial resolution with in-situ cooling capabilities and sufficient energy resolution to resolve the local doping and spin state variations.

Recently, atomically resolved Z contrast imaging combining with EELS has been used to examine electronic and magnetic properties of epitaxial $LaCoO_3$ thin films (95)·(95, 96). For example, *Kwon et al.(95)* and *Biškup et a(96)l* report the presence of a superstructure, which shows itself as dark stripes, is found in epitaxially strained $LaCoO_3$ thin film grown on $SrTiO_3$ substrate. Using EELS of the cobalt *L*-edges and oxygen *K*-edges, *Kwon et al.*[16] conclude that the superstructure is caused by cobalt spin state ordering rather than the oxygen vacancy ordering previously reported in $SrCoO_3$,(97) as well as strained $LaCoO_3$. However, both oxygen vacancies and changes in the Co-ion spin states result in similar changes in the oxygen K-edge fine-structure and a systematic study of the effects of hole doping on the local Co-ion spin state transition has not yet been reported. Moreover, the effects of hole doping on the O K-edge pre-peak intensity, as well as the local Co-ion spin state will lay the foundation for any future work focusing on the spatial distribution of magnetic clusters near the critical hole doping concentration of 17%.

In this part of my thesis, I use high-angle annular dark field (HAADF) imaging in combination with electron diffraction, angular-resolved EELS, and *in situ* cooling experiment in an aberration-corrected scanning transmission electron microscope (STEM), the UIC JEOL ARM200CF, to study $LaCoO_3$ single-crystals with 5%, 17% and 30% Sr

doping. I will demonstrate that by using these techniques which provide local probe, only $La_{0.95}Sr_{0.05}CoO_3$ single-crystal samples exhibits the signs of a low temperature spin-state transition upon *in-situ* cooling that was previously observed in NMR measurements of spin relaxation rates.(16) The JEM-ARM200CF is equipped with a probe aberration corrector, a cold field emission source allowing for 0.35eV energy resolution and a Gatan Enfina electron energy loss spectrometer. The *in-situ* cooling experiments are performed by using the Gatan double-tilt liquid nitrogen (LN_2) cooling stage (model 636 cryogen). During the cooling experiment the sample experiences spacial drifting and other mechanical instabilities. The objective lens creates a local magnetic field of several Tesla and will contribute to spin alignment of the sample during the STEM measurements.

Figure 19 shows selected area electron diffraction patterns (SADP) taken from the three different samples in the [110] orientation at room and LN_2 temperatures. The effects of *in-situ* cooling are shown in green and red for room and LN_2 temperature, respectively, with the overlap region shown in white and the background in blue. None of the samples are found to have any kind of structural phase transition during cooling experiment. The 5% and 17% doped samples show an isotropic increase in the diffraction

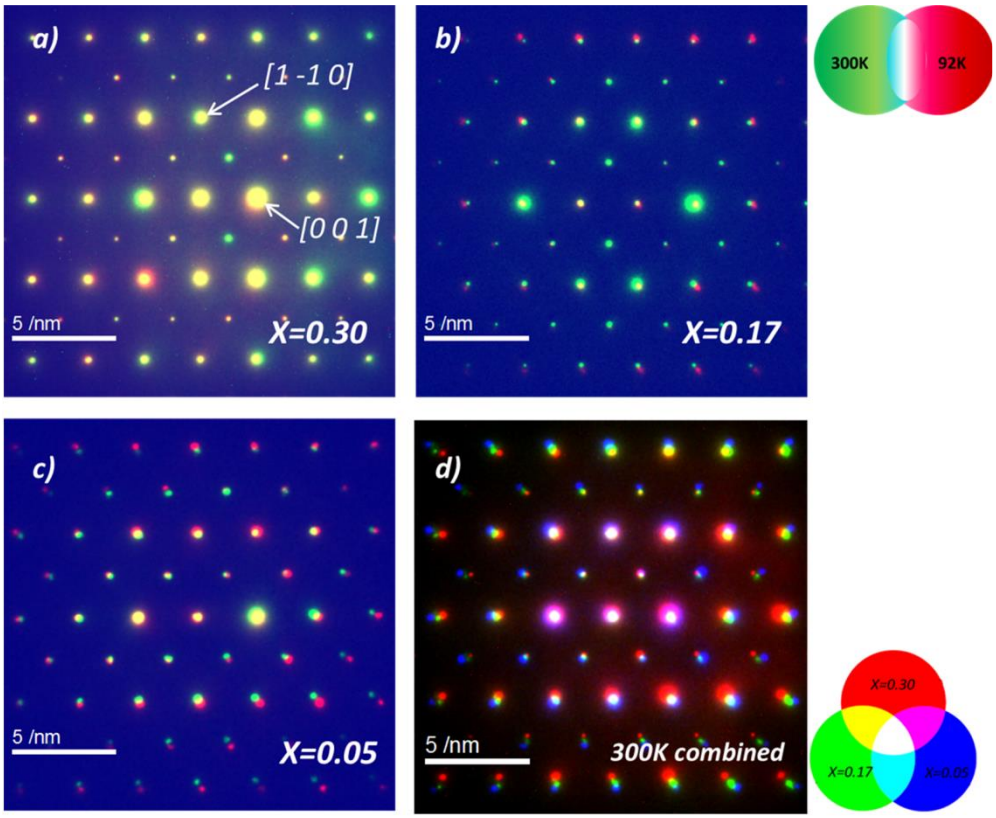

Figure 19 Combined selected area diffraction pattern (SADP) of $La_{1-x}Sr_xCoO_3$ at room temperature (RT) in green color and liquid nitrogen temperature (LNT) in red color after in situ cooling in [011] direction *a) for x=0.30 b) x=0.17* and *c) x=0.05*. *d)* SADP of three samples combined in room temperature in same orientation where x=0.30, x=0.17 and x=0.05 are shown in red, green and blue, respectively.

patterns at low temperature, corresponding to an overall shrinkage in crystal structure volume, while the 30% Sr-doped sample shows no detectable change in the diffraction patterns. A comparison of the diffraction patterns for all three doping concentration at room temperature is also shown in Figure 19d) and reveals that the overall unit cell volume increases with the increase in Sr-doping from 5% to 30%. This is consistent with previous

reports for the parent $LaCoO_3$ and different amount of *Sr* doping concentrations.(98), (99), (100)

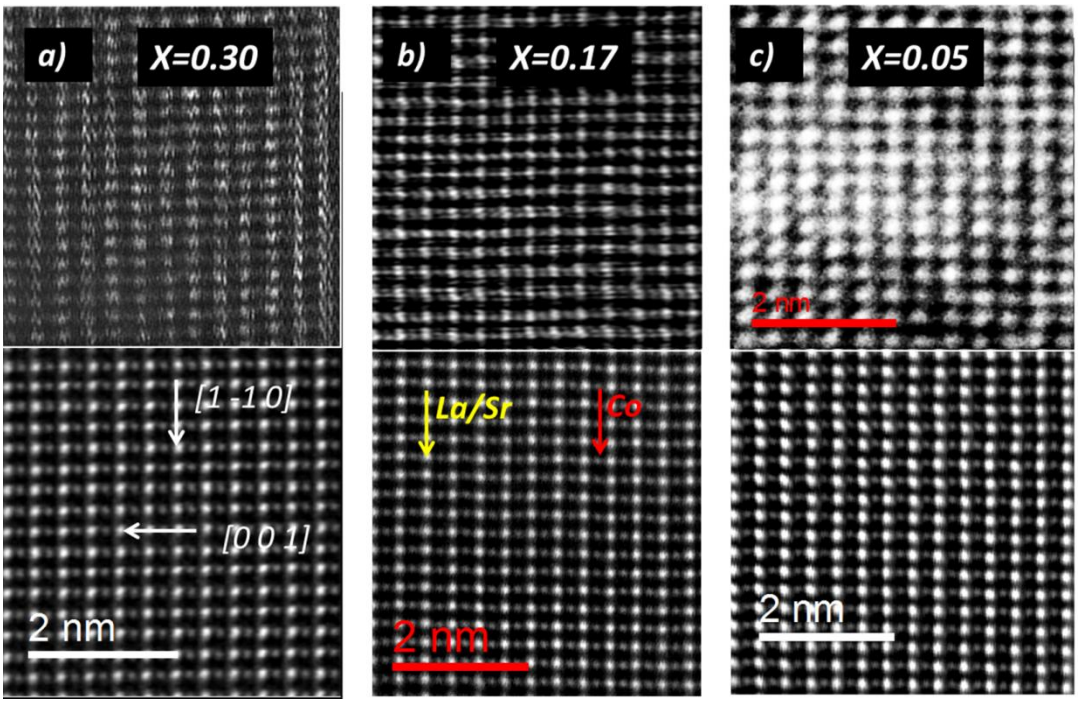

Figure 20 HAADF images taken at [110] pseudo cubic orientation at LNT at the top and HAADF images taken at RT in the bottom in the same orientation are shown for *x=0.30, x=0.17* and *x=0.05* respectively.

Atomic-resolution high-angle annular dark-field (HAADF) STEM images of single crystal $La_{1-x}Sr_xCoO_3$ in the pseudo cubic [110] orientation are shown in Figure 20, both at room temperature and at liquid nitrogen temperature (LNT). Since the HAADF image contrast is highly sensitive to atomic columns with higher Z elements, imaging of oxygen columns cannot be achieved due to its low atomic number and screening effects of heavier neighboring atoms. In Figure 20, the lower image intensity stems from the Co atomic

columns while higher intensity columns consist of La\Sr atoms. The image resolutions appear worse during *in-situ* cooling due to mechanical instabilities associated with LN_2 boiling off and spatial sample drift. For *x=0.05*, I show a TEM high-resolution phase-contrast image instead of a HAADF and the Co column not resolved here. In the single crystal samples studied here, I do not observe any superstructure at either room temperature or at low temperature, such as darker or lighter stripes which were reported earlier for $LaCoO_3$ thin films on different substrates due to the presence of spin state or vacancy ordering. However, having extra spots at diffraction pattern at $\left[\frac{1}{2} - \frac{1}{2}\frac{1}{2}\right]$ in the pseudo-cubic directions for all doped samples (as seen in Figure 19 at both temperature and low temperature) can be interpreted as a modulation in the size of unit cell in the pseudo cubic [110] orientation as the result of CoO_6 octahedral distortion. Since TEM and HAADF imagining techniques used here are not sensitive to imaging light elements, such as oxygen, I will not able to confirm or quantify this distortion. However, I have not observed any structural symmetry change as a function of temperature other than the overall decrease in unit cell volume based on our electron diffraction analysis.

It has been shown that EELS of the O K-edge can be utilized to measure the Co-ion spin-state transitions by quantifying the O K-edge pre-peak intensity(9). In addition, the transition metal L_2 and L_3 edges, which are results of transition of an electron from the transition metal *2p* states to unoccupied *3d* orbitals, can be utilized to determine the occupancy of the transition metal *3d* orbitals.(101) (12) While the L_3/L_2 intensity ratio, or so called white line ratio, is an indication of valance states of Co atoms, the energy

resolution of non-monochromated electron guns is not sufficient to resolve changes due to spin-state transitions of the Co ions. X-ray absorption spectroscopy has demonstrates the ability to resolve those changes, but suffers from significantly lower spatial resolution. (7)

Error! Reference source not found. shows the EELS of single-crystal $La_{1-x}Sr_xCoO_3$ samples oriented in the pseudo cubic [110] direction, both at room temperature and liquid nitrogen temperatures. In **Error! Reference source not found.**a-c), the O *K*-edges is shown at room temperature (solid line) and liquid nitrogen temperature (dashed line), exhibiting three peaks near the edge onset, labeled *a*, *b* and *c*. I use these peaks to identify a possible Co-ion spin state transition as a function of temperature and Sr-doping. The O K-edge intensity is normalized to the continuum intensity above 560 eV. The O K-edge pre-peak, labeled *a*, stems from the hybridization of *O 2p* with *Co 3d*, whereas peaks *b* and *c* can be assigned to the hybridization of *O 2p* with *La 5d* and *Co 4sp*, respectively. At room temperature, the increase in the Sr-doping concentration increases the Co^{4+} concentration resulting in an increased number of available Co 3d states, which manifests itself as a relative increase in the *O K*-edge pre-peak intensity, as seen in **Error! Reference source not found.**. At low temperature, there is an increase in the pre-peak intensity, labeled *a*, for 5% doped sample while a similar change is not observed for critically doped, 17% sample and for the 30% doped sample. This observed increase in the pre-peak intensity can be either due to the creation of oxygen vacancies or any change in the electron distribution at Co e_g and t_{2g} orbitals which origins a Co-ion spin state transition. However, the *Co L*-edge structure, which is sensitive to the valence state of the Co atom, and thus also the presence of Co or O vacancies, does not indicate any significant change at room

and LN_2 temperature not only for 5% doped sample but all other doping concentrations as shown in lower corner of Figure 3 for each sample.

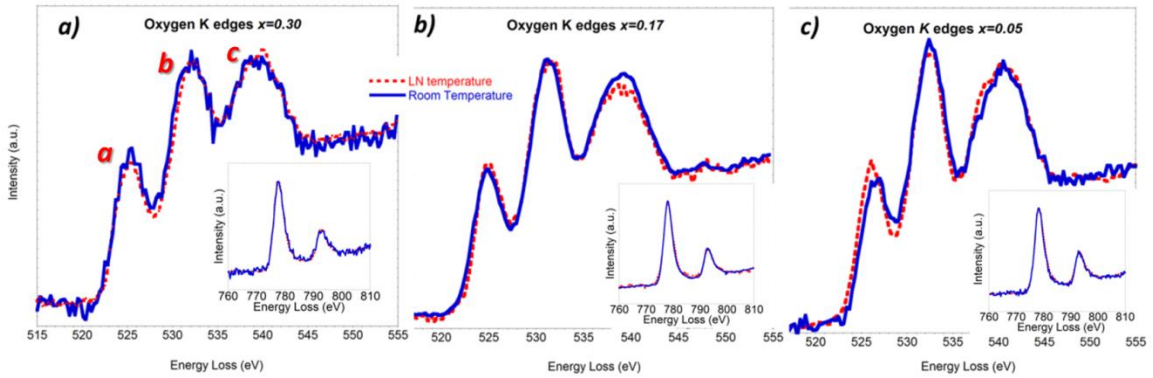

Figure 21 EELS of O K edge taken in room temperature in solid line and liquid nitrogen temperature in dashed line of *a)* $La_{0.70}Sr_{0.30}CoO_3$ $La_{0.95}Sr_{0.05}CoO_3$, *b)* $La_{0.83}Sr_{0.17}CoO_3$ and *c)* $La_{0.95}Sr_{0.05}CoO_3$. Similarly EELS data of *Co L* edges both at room temperature and at liquid nitrogen temperature for each sample is inserted at right lower corner.

Assuming that the stoichiometry of the samples remains unchanged during the in-situ cooling experiments, one can explain the change in the O K edge pre-peak intensity as follows: In the LS-state configuration, the Co^{3+} e_g energy levels are solely responsible for the pre-peak intensity, since all the t_{2g} orbital are filled with the $3d^6$ electrons. On the other hand, in the higher spin-state configurations, while the Co oxidation state remains unchanged, but the Co e_g orbital are no longer completely empty, thus reducing the number of available states in the e_g orbitals for exited electrons, while simultaneously increasing the number of available t_{2g} orbitals. Therefore, one should expect an increase in the O K-edge pre-peak intensity at low temperature for samples that have undergone a transition to the Co-ion low spin-state. I conclude that the observed decreased intensity of O *K*-edge

pre-peak in the sample doped with 5% Sr is due to a thermally induced Co-ion spin state transition, similar to that reported in undoped $LaCoO_3$.(9)

Kwon et a[95] reported that spin state ordering in $LaCoO_3$ film grown on $SrTiO_3$ substrate results a superstructure of ordered darker stripes found perpendicular to film/substrate interface, and concluded that the increased atomic distances in the dark stripes are responsible for smaller hybridization between *Co* and O atoms, and, therefore, for a higher Co-ion spin state. Moreover, this structural change also lowers the peak ***c*** of the O K-edge, which stems from the hybridization between spherically symmetric *O s* state and *Co d* states. However, in the data shown in here, I do not observe any crystal symmetry change other than the decrease in unit cell volume as the result on *in-situ* cooling. If the change in the O *K*-edge fine structure was purely structural, then I should have seen an increase in intensity of peak ***c*** through cooling in both 17% and 5% doped samples as a result of the decrease in the unit-cell volume at lower temperature. However, the intensity of peak *c* remains unchanged in the 5% doped sample, while a decrease is seen at low temperature for the 17% doped sample. Therefore, I conclude that this spin state transition is temperature driven rather than structural, since the change in exchange energy is more dominant than the change in the crystal splitting as the result of sample cooling. On the other hand, not having the spin-state transition at higher doping concentration (e.g. 17% and 30%) can be explained by the fact that a single La^{3+} atom has 8 *Co* neighbors which will be affected the substitution with a divalent Sr atom. Thus, increasing the doping concentration from 5% to 17% will increase the number of the Co^{4+} ions in a higher spin state (due to the presence of Sr^{+2}), so that the doping-driven spin state transition to higher

spin state is dominant and the thermally driven spin-state transition can no longer be observed.

In summary, with a local probe provided by STEM and EELS, I find a Co-ion spin state transition in 5% doped $La_{1-x}Sr_xCoO_3$ through in-situ cooling experiments, while 17% and 30% doped samples do not show any indication for such transitions. In samples below the critical doping concentration of x=17%, atomic resolved HAADF images and SADP do not show any indication of a changes in crystal structure symmetry during the in-situ cooling which can possibly be responsible of the observed changes in the *O K*-edge fine-structure. For higher doping concentration, such as the 17% and 30% doped samples studied here, the doping driven spin state transition is dominant over thermally driven spin state transition at low temperature. These results now allow me to distinguish for the effects of oxygen vacancy ordering from Co-ion spin state ordering, as previously reported for $LaCoO_3$ thin films. This will be essential in studying the percolative nature of the magnetic ordering in hole-doped $LaCoO_3$ samples both thin films, as well as single crystal. It was previously suggested that the phase transition in Sr-doped $LaCoO_3$ is associated with merging of magnetically ordered clusters of the length-scale of a few unit cells. Due to the lack of spatial resolution of many magnetic probes, EELS in a STEM appears to be the ideal candidate to study this transition and the work reported here lays the foundation for such an experiment. Using the reported changes in the O K-edge pre-peak intensity and the anti-correlation with the Co $L_{3,2}$-ratio, the spin state transition can now be clearly distinguished from a change in local Co valence due to oxygen vacancies or local chemical inhomogeneities.

4 STRUCTURE AND SPIN STATES OF $La_{1-x}Sr_xCoO_3$

4.1 Introduction

$LaCoO_3$-based perovskite oxides have been studied for decades, primarily due to their exceptional magnetic transitions which are related to changes the Co^{3+}-ion spin states. Bulk $LaCoO_3$ has a temperature dependent transition from a nonmagnetic to a semiconducting insulating state, which occurs below 100 K and another transition from semiconducting to metallic phase above 500 K. Cobalt spin states transitions are strongly correlated to the competition between the crystal-field splitting (Δ_{CF}) of the Co *3d states* into e_g and t_{2g} orbitals, which encourages the lower spin states, and the Hund's exchange rule, which is responsible for higher spin configurations. The first magnetic transition is believed to be due to a change in the Co^{3+}-ion spin state from a LS ($t^{6}_{2g}\, e^{0}_{g}\, S=0$) state to combination of the HS ($t^{4}_{2g}\, e^{2}_{g}\, S=2$) (5) and LS states(102) or alternatively an intermediate spin ($t^{5}_{2g}\, e^{1}_{g}\, S=1$) IS(8)(9) state as seen in Figure 22a). In addition to the Δ_{CF} and the exchange energy, the bandwidth *W*, resulting from the σ-bonding Co-O-Co interaction, and the reduction in the energy difference between e_g and t_{2g} orbitals favors the higher spin states(13).

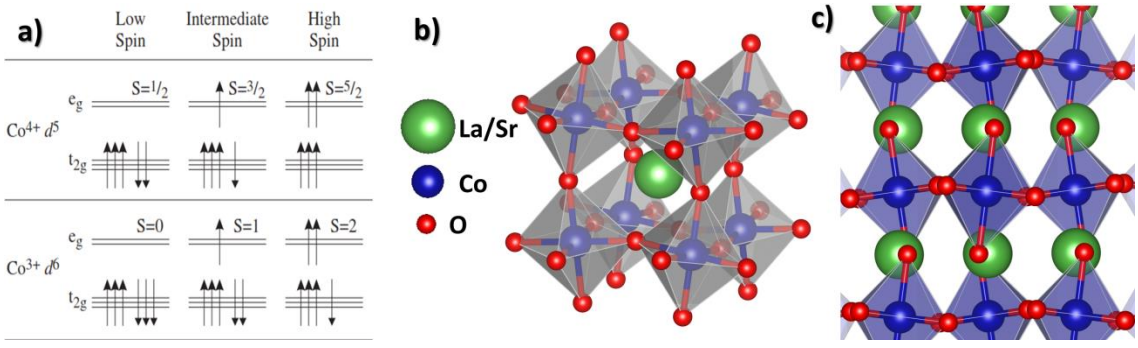

Figure 22 ***a)*** *P*ossible spin state configurations of Co^{3+} and Co^{2+}. ***b)*** Crystal structure of $La_{1-x}Sr_xCoO_3$. c*)* Projection of $La_{1-x}Sr_xCoO_3$ in pseudo-cubic [011] orientation.

The small difference between the crystal-field splitting and the interatomic Hund`s rule exchange energy allows the magnetism of $LaCoO_3$ and related materials to be altered by changing the particle size of powder sample(10), epitaxial tensile strain on thin film sample via the properly chosen substrate(11),(12), applying external pressure to bulk sample(13),(14) or hole doping with a alkaline rare-earth ion having a different ionic radius, such as *Sr*. Introducing external, strain or chemical pressure by doping with suitable ion can lead to a change in the lattice parameters and to CoO_6 distortions, which will affect the Co-O bond distance, the Co-O-Co bond angle, and ultimately the magnetic ordering(24). Therefore, substituting divalent Sr^{2+} ions for trivalent La^{+3} ions does not only increase the average Co oxidation state and spin states but also changes the structure of CoO_6 environment which can directly alter the spin state and spin ordering of Co ions. A schematic of a rhombohedrally distorted crystal structure for $La_{1-x}Sr_xCoO_3$ and te projection of the pseudo-cubic [011] orientation are seen in Figure 22*b)* and *c)*, where the distortion of the CoO_6 octahedra is visible. Recently, first principles calculations revealed that the cubic octahedral environment is more stable for magnetic states than non-magnetic ones while introducing rhombohedral distortion lowers the non-magnetic ground states and insulating character.(25)

Various techniques from Extended X-ray Absorption Fine Structure (EXAFS), Neutron Pair Distribution Function (PDF)(15), NMR(16),(17) , Small-Angle Neutron Scattering (SANS)(18), and Inelastic Neutron Scattering (INS), to Electron Spin Resonance

(ESR)(19) have been used to study $La_{1-x}Sr_xCoO_3$ (LSCO). It is generally accepted that with increasing Sr-doping, $La_{1-x}Sr_xCoO_3$ changes from a non-magnetic insulator, which undergoes a thermally induced Co^{3+} ion spin state transition at low temperature, to a spin glass at low Sr-doping and a ferromagnet at higher doping. As the Sr-doping concentration increases, spin polarons, which are caused by substituting divalent Sr^{2+} ions for trivalent La^{+3} ions, merge and form short-range FM clusters, since the neighboring mixed valance Co ions interact ferromagnatically via double exchange mechanism(17). At the critical doping of $x \approx 0.17$, the clusters percolate, leading to a crossover from short- to long-range FM(26) and the system simultaneously undergoes a percolative insulator-to-metal transition (IMT).(17)

In this chapter, I will use HAADF imaging in combination with ABF imaging, angular-resolved EELS, EMCD(86) and *in situ* cooling experiment in an aberration-corrected STEM. More specifically, the UIC JEOL ARM200CF will be used to study $LaCoO_3$ single-crystals with 5%, 17% and 30% Sr doping. I will demonstrate the power of real space probes with atomic resolution and sensitivity to magnetic properties.

4.2 Results and Discussions

4.2.1 Imaging results

In Figure 23, an atomic-resolution HAADF image of $La_{0.95}Sr_{0.05}CoO_3$ in pseudo cubic [011] direction is presented. Figure 23a) shows the original image, and the Fast Fourier transform (FFT) and a proposed model of the CoO_6 octahedra as an insert. The FFT shows additional spots at [1/2 1/2 1/2] of the pseudo cubic orientation (marked by arrow). To

understand the origins of these extra spots, I apply a k-space mask and the resulting inverse FFT is shown in Figure 23b), which clearly shows the modulation as a result of the superlattice peaks. In Figure 23 *c)*, the inverse-FFT filtered image is added three times to raw data to demonstrate the effects of the superlattice spots on the atomic structure of $La_{0.95}Sr_{0.05}CoO_3$. The exaggerated modulation can now be clearly seen, as indicated by the two arrows in adjacent La/Sr columns. Arrows in similar locations are placed in the atomic model shown in Figure 22b). I attribute this modulation to the rotation of two neighboring CoO_6 octahedra, which will create a zigzag pattern and thus horizontal and vertical contraction in the Co-O interatomic spacing. Even though HAADF is sensitive to atoms with higher atomic numbers, and is generally not able to directly image oxygen atomic columns, one can observe the effect of CoO_6 distortion by using HAADF imaging.

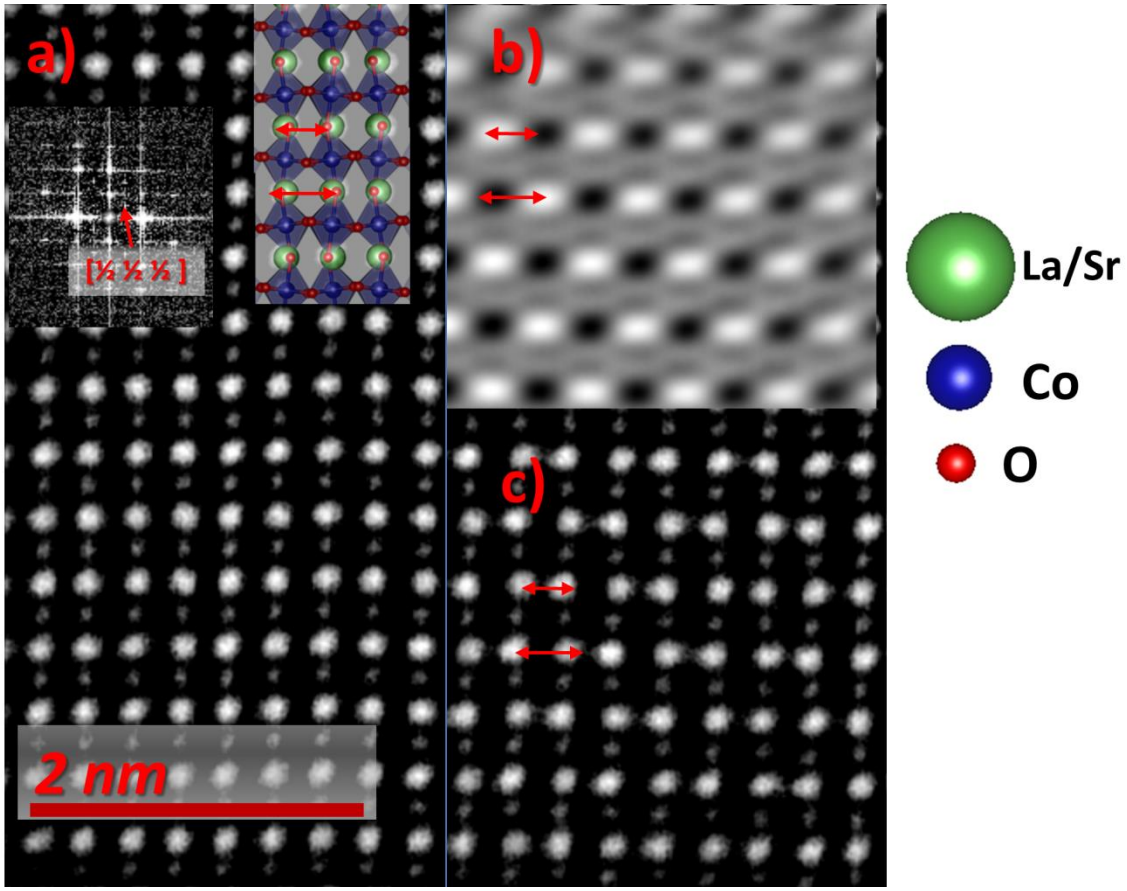

Figure 23 HAADF image of $La_{0.95}Sr_{0.05}CoO_3$ in pseudo cubic [011] direction: a) the raw data and FFT of the whole image (insert). Extra spots in [1/2 1/2 1/2] pseudo cubic orientation is indicated by the arrow. The model indicates the atoms in this orientation. b) Filtered inverse FFT highlighting the effects of the superlattice peaks. c) Inverse-FFT filtered extra spots are strengthened by 3 times and added to raw data. The exaggerated modulation can be seen by the help of two arrows between succeeding La/Sr columns. Similar corresponding arrows are placed in the model structure shown in a).

Next, these CoO_6 distortions will be measured using ABF imaging which is sensitive to lighter elements, such as oxygen or even hydrogen. In Figure 24, an ABF image of $La_{0.95}Sr_{0.05}CoO_3$ in pseudo cubic [011] direction is shown and the corresponding ball and stick model is shown as an insert. Displacement of the oxygen columns in the vertical direction is clearly seen in the image. The CoO_6 octahedra distortion manifests itself by the

zigzag pattern in horizontal direction (the [0-11] pseudo cubic orientation). In Figure 24*b)*, the quantitative analysis of the oxygen column displacement in y direction is shown. The accurate position of each oxygen column is estimated by calculating the center of mass over the areas where the oxygen signal is present. Each rectangle shows the displacement of corresponding oxygen atomic column in vertical direction with respect to average position of two neighboring Co columns on the right hand side and the left hand side of the particular oxygen column. The results exhibit an ordered checkerboard pattern, confirming the presence of a periodic CoO_6 distortion. The average magnitude of the displacement of oxygen columns in y direction is measured to be 19 pm ±14 pm over the entire area of the image while the average displacement is 3 pm ±24 pm. In Figure 24*c)*, the histogram of the displacement map is shown. The histogram shows the frequency of the individual displacement value. If the oxygen columns have the perfect zigzag pattern, the histogram should be symmetrical around zero. The symmetry in Figure 24*c)* shows that 5% Sr doped $LaCoO_3$ distortion is very close to a perfect zigzag pattern.

Figure 25 shows a similar analysis for the $La_{0.83}Sr_{0.17}CoO_3$ sample. The checkerboard pattern Figure 25*b)* confirms the regularity of CoO_6 distortion. However, the average absolute value of oxygen column displacement in vertical direction with respect to neighboring cobalt atomic columns is reduced to 15 pm ±11pm while the average displacement is -8 pm ±18 pm. Similarly, the histogram of the oxygen displacement map is shown in Figure 25c*)*. The effect of increasing the Sr doping concentration from 5% to 17% on the local crystal structure is that at higher hole doping, the structure resembles

more closely the cubic unit cell even though the center of the histogram is shifted towards slightly negative side by 8 pm.

For the $La_{0.7}Sr_{0.3}CoO_3$ sample, similar experiments and analysis were completed and the results are shown in Figure 26. In contrast to the lower doping concentrations, the $La_{0.7}Sr_{0.3}CoO_3$ sample exhibits irregularities in the oxygen column displacements. In certain areas, the displacement of oxygen columns does not adhere to the checkerboard-like pattern, while other areas show a strongly distorted structure in one specific direction and while another area exhibits distortion in a different direction. However, the majority of the $La_{0.7}Sr_{0.3}CoO_3$ sample exhibits the more regular, albeit smaller, octahedral distortion compared to the samples with lower Sr-doping concentrations. The average magnitude of the displacement of oxygen columns in y direction is measured to be 37 pm ±23 pm over the entire area of the image while the average displacement is 13 pm ±42 pm. In Figure 26*c)*, the histogram of the displacement map is shown. The biggest difference between 30% doped sample and the other samples studied here can be found in areas with irregular and large oxygen displacements as shown in Figure 26. Looking at the displacement histogram analysis of three samples, one can conclude that in lower Sr dopant concentration, the displacement distributions are more symmetrical, such that the average displacement is closer to zero and histogram looks more symmetrical around zero. On the other hand, in 30% doped sample the heavily distorted area, which can be identified as the region with two dark stripes in the displacement map in Figure 26*b)*, is compensated by weaker distortion over the rest of the area. It also can be seen in the histogram as the separation of the signal into two statistically independent areas.

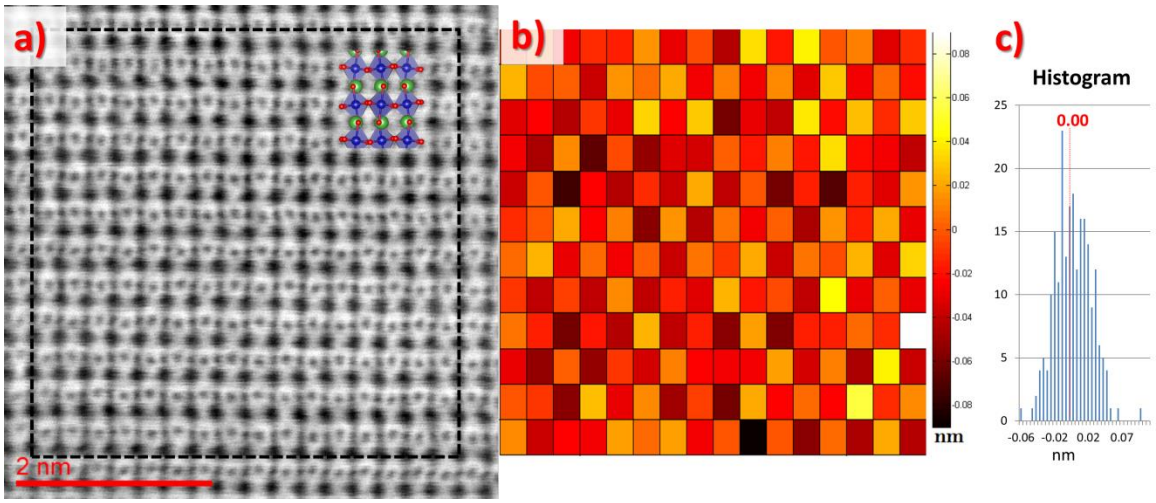

Figure 24 a) ABF image of $La_{0.95}Sr_{0.05}CoO_3$ in pseudo cubic [011] direction with a model structure shown as an insert. The biggest dark spots are A site of the perovskite and in *x* direction ([0 -1 1] pseudo cubic orientation) Co and Oxygen columns are seen. b) Displacement of individual Oxygen column in y direction with respect to neighboring Co columns measured from the dashed area on the ABF image is shown. The histogram of O column displacement map is shown in c).

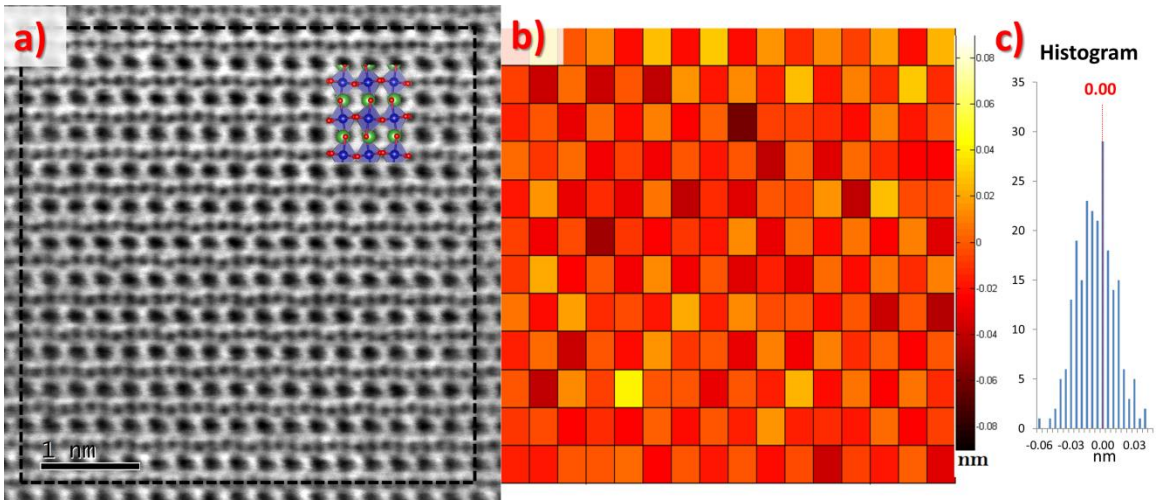

Figure 25: a) ABF image of $La_{0.83}Sr_{0.17}CoO_3$ in pseudo cubic [011] direction with a model structure shown as an insert. b) Displacement of individual Oxygen column in y direction with respect to neighboring Co columns measured from the dashed area on the ABF image is presented. The histogram of O column displacement map is shown in c).

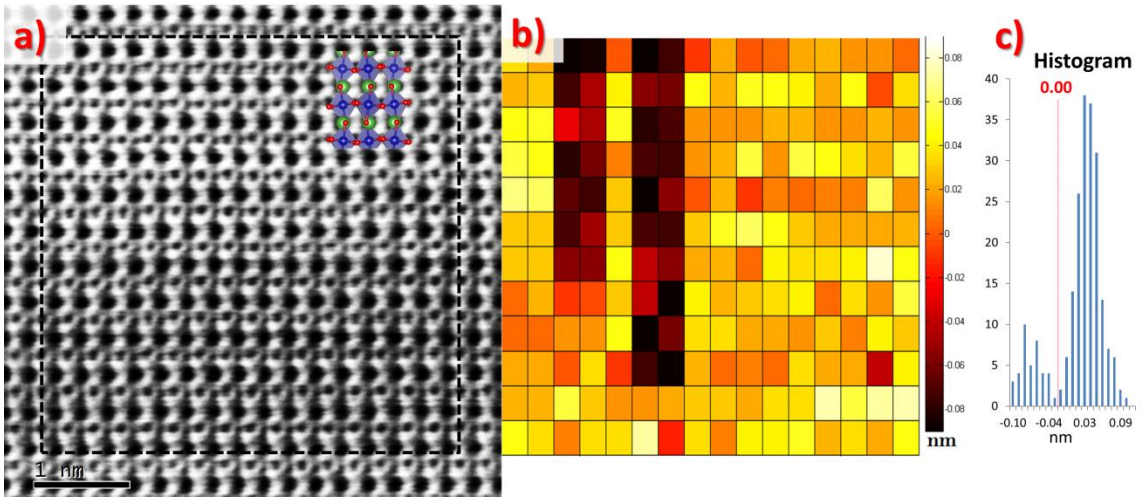

Figure 26: a) ABF image of $La_{0.70}Sr_{0.30}CoO_3$ in pseudo cubic [011] direction with a model structure shown as an insert. *b*) Displacement of individual Oxygen column in y direction with respect to neighboring Co columns measured from the dashed area on the ABF image is presented. The histogram of O column displacement map is shown in c).

4.2.2 EELS results

In addition to ABF imaging, atomic-column resolved EELS can be used to examine the displacements of the oxygen columns in pseudo-cubic [011] orientation. In Figure 28 three EELS maps are shown, one for each Sr-doping concentration. In top row, integrated *O K-edge* intensity maps are shown, while the integrated *Co L-edge* intensity map and the combination of *O K-edge*, *Co L-edge* and *La M-edge* maps are also shown. *O K-edge* intensity integrated over 80 eV energy window centered at 521 eV after background subtraction. Similarly, *Co L-edges* are integrated over 55 eV energy window centered at 785 eV and *La M-edges* intensity is integrated over 37 eV energy interval centered at 850 eV after background subtractions. For $La_{0.95}Sr_{0.05}CoO_3$, the regular distortion of the O columns is clearly shown and as the Sr-doping concentration increases, the distortion of the CoO_6 is visibly weakened which confirms our previous ABF results.

In perovskite oxides, the oxygen K-edge EELS has been shown to reveal the hybridization of the transition metal and the oxygen states in oxides, since it probes the transition from the *O 1s* to *O 2p* states to selectively measure the density of unoccupied states with *O 2p* symmetry. On the other hand, the *O K-edge* pre-peak originates from transitions into the hybridization between *O 2p* and transition metal *3d* states. It has been previously shown that the *O K-edge* pre-peak intensity is very sensitive to the oxygen stoichiometry and the transition metal oxidation state(12). At the same time, several studies have shown the correlation between the *Co L-edge* energy onset (and intensity ratio) and the local Co valence(81). More specifically, for $LaCoO_3$ systems, hole doping increase the intensity of *O K-edge* pre-peak intensity which probes the population and the distribution of the electron at unoccupied t_{2g} and e_g energy levels as shown in Figure 27, while Co L_3/L_2 intensity ratio, so called white line ratio, decreases for higher Co oxidation state.

In Figure 27, O K-edge intensities are shown for 3 different doping concentrations, namely 30%, 17% and 5%. It can be clearly seen that the O K-edge pre-peak intensity increases with increasing Sr concentration, due to the formation of the additional unoccupied oxygen ligand hole states i.e. depopulation of the t_{2g} levels as well as a transfer of electrons from the e_g spectral weight. At the same time, the pre-peak energy shifts to lower energy for $x \geq 0.17$.

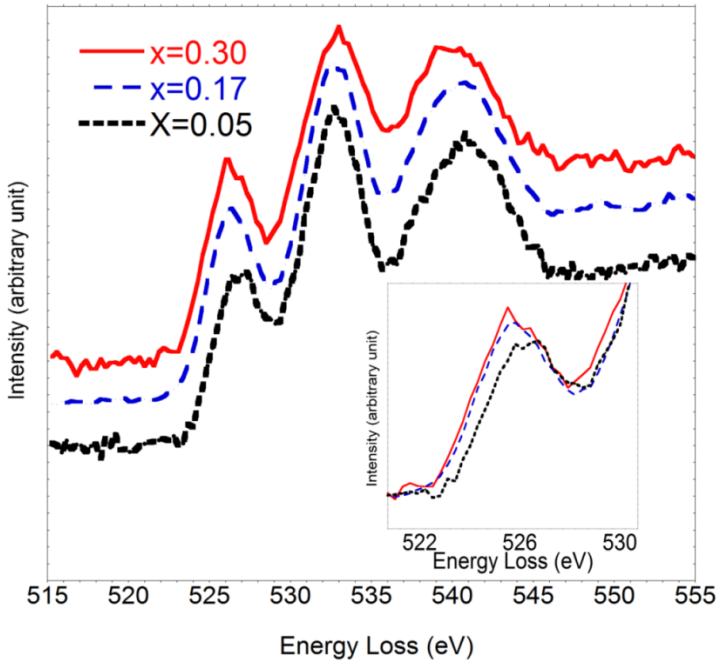

Figure 27 O K-edge EELS of 3 different Sr doping concentration. Normalized pre-peak intensities are inserted.

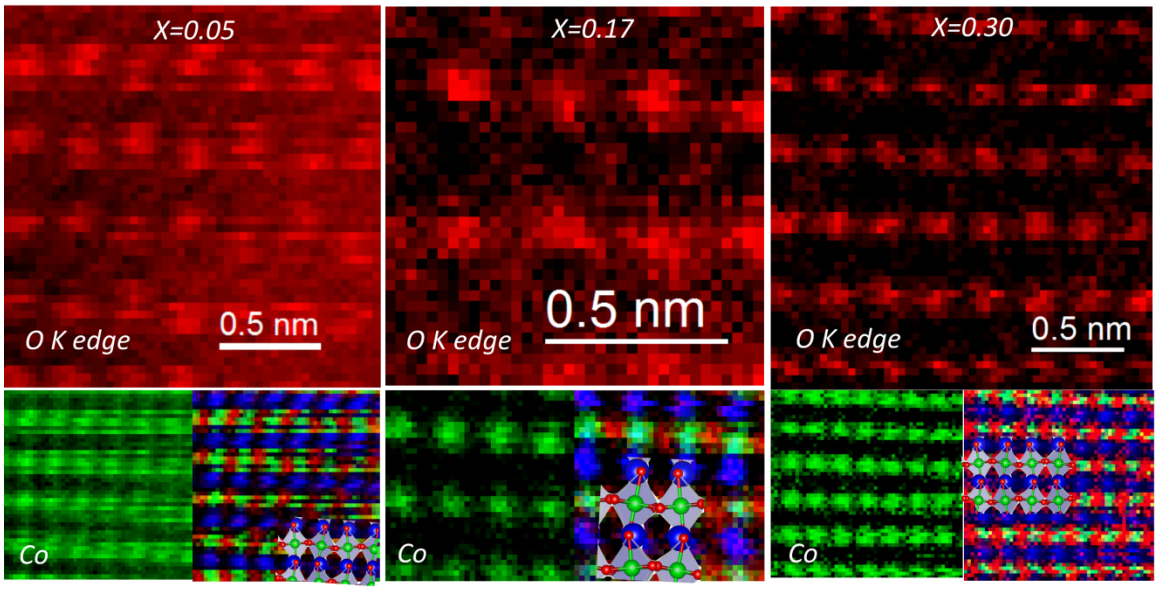

Figure 28 Atomic resolved EELS maps are shown for three different sample from x=0.05 to x=0.30 right to left. On top, *O K-edge* maps are shown with *Co L-edge* maps on the lower left corners. On the lower right hand side, *La M-edge*, *Co L-edge* and *O K-edge* maps are combined with the cartoon identifying the atoms inserted.

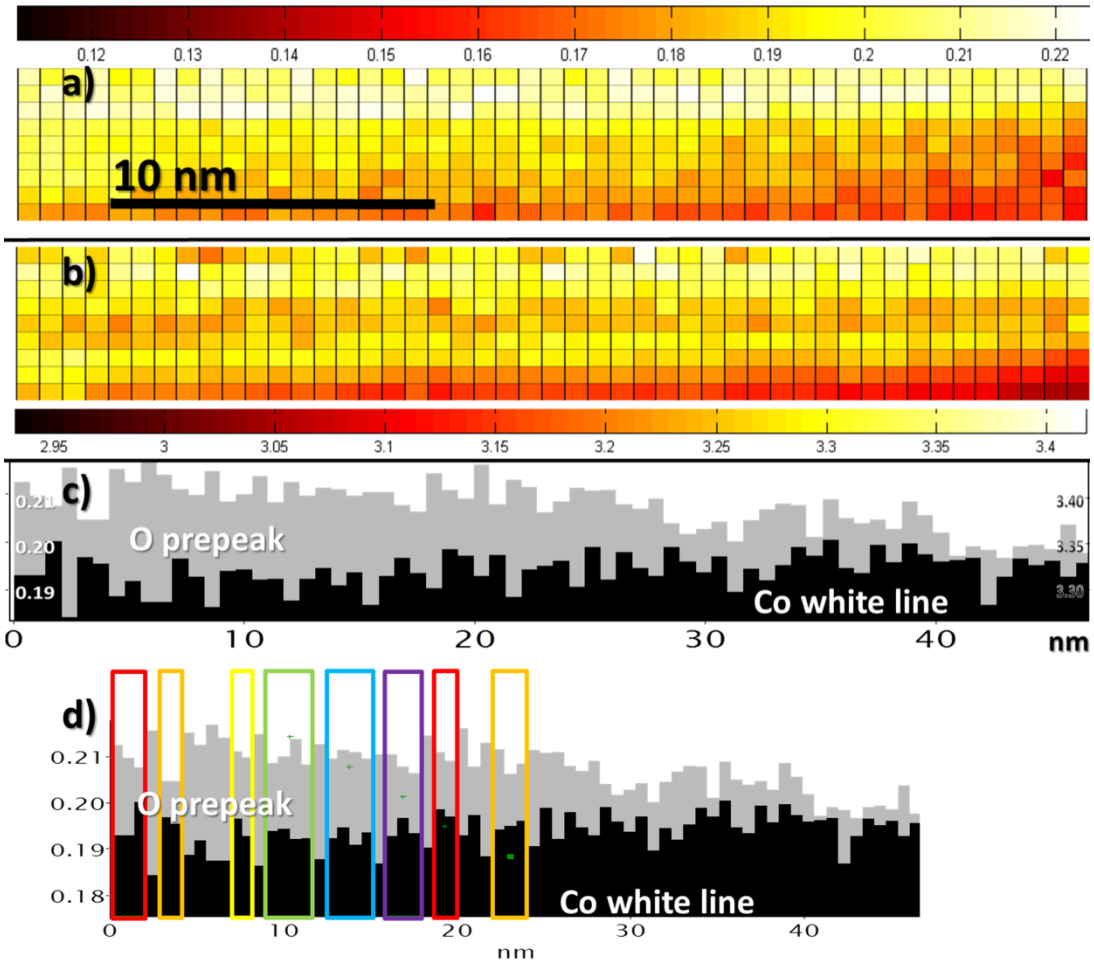

Figure 29 EELS maps at [011] pseudo cubic orientation of a) *O K-edge* pre-peak intensity normalized by the total *O K-edge* intensity, ***b)*** the Co white line ratio in $La_{0.83}Sr_{0.17}CoO_3$ at room temperature. ***c)*** Comparison of O pre-peak intensity and Co white line ratio profiles which are integrated over top three pixels in y direction is shown. *d)* Deviation in white line ratio and the O K edge pre-peak at intensity *c)* alteration is labeled.

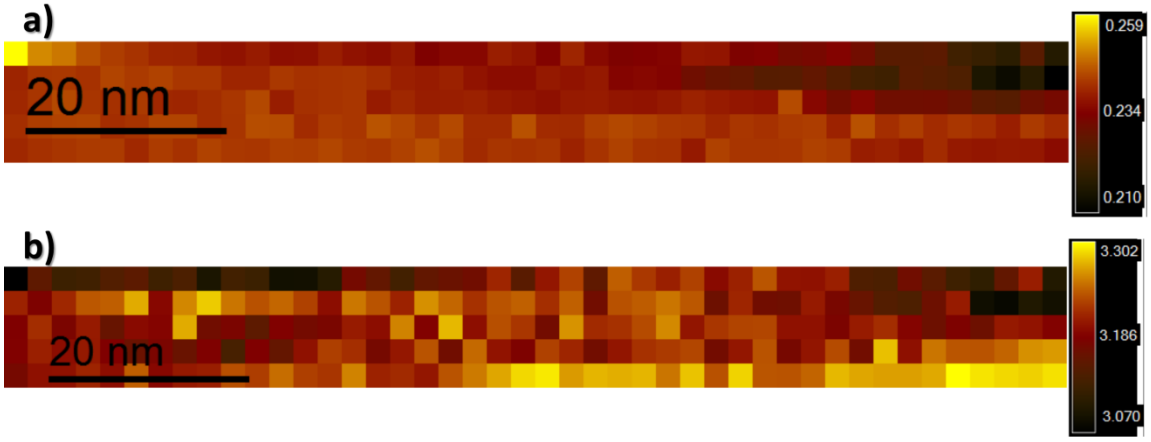

Figure 30 EELS maps at [0 1 1] pseudo cubic orientation of a) *O K-edge* pre-peak intensity normalized by the total *O K-edge* intensity, ***b)*** Co white line ratio in $La_{0.83}Sr_{0.17}CoO_3$ at Liquid Nitrogen temperature. Co white line ratio map shows that the Co oxidation state is not homogenous through the sample.

Since, $La_{0.83}Sr_{0.17}CoO_3$ exhibits a MIT at ~80 K, which is above the in-situ cooling temperature, the effects of chemical and magnetic inhomogeneities on the transition can also be examined(17). Due to the negative correlation between the white line ratio and Co valance state, one should expect that a decrease in white line ratio (increase in Co oxidation state) should increase the *O K-edge* pre-peak intensity, if the Co ion simply loses an electron. Therefore, by mapping the Co white lines and O K-edge pre-peak intensity throughout the sample, I can determine the chemical homogeneity within a grain. However, if one does not observe the negative correlation between Co white line ratio and *O K-edge* pre-peak intensity, this observation cannot be explained by a simply change in the electron population of the unoccupied t_{2g} and e_g states. The explanation requires the redistribution of these electrons in the t_{2g} and e_g levels, which results in a change of the Co-ion spin state.

In Figure 29, the integrated *O K-edge* pre-peak intensity and Co L_3/L_2 ratio of $La_{0.83}Sr_{0.17}CoO_3$ are plotted as a function of position through the sample at room temperature. To map the peak intensities, we use the second derivative method (103)·(104) which provides a background independent result by just taking the positive contribution of the second derivative of the spectra under the specific peak. Since multiple scattering can affect the relative peak intensities, we choose an area with an average thickness of 0.14 inelastic mean free path. Each pixel has the size of *0.7 nm* and the sample is viewed along the pseudo cubic [011] orientation. Figure 29b) shows the white line ratio map which clearly contains areas with different cobalt oxidation state. One can identify two competing regimes within the mapped region. First, the top left hand side of the region has higher O *K-edge* pre-peak intensity and higher white line ratio compare to lower right hand side corner. Since a higher white line ratio can be read as low oxidation state, one should expect a lower O *K-edge* pre-peak intensity due to the lower number of empty *d* state to excite. This can be seen in Figure 27, such that the pre-peak intensity increases as the average oxidation state of Co rises from 3.05 to 3.3. However, in Figure 29, the same area does have higher *O K-edge* pre-peak intensity. Therefore, one should take into account not only the population of electrons in the *d* levels but also their distribution, namely total spin state, to explain this situation. In the lower right corner, the cobalt oxidation state is lower, resulting in a higher number of electrons in the t_{2g} and e_g levels. On the other hand, to have higher O *K-edge* pre-peak intensity, the e_g levels should be less occupied compared to the other corner of the sample. Co ions have lower spin states when e_g levels are not occupied as seen in Figure **22**a). Moreover, there are more available states for inner *p* level electrons

to excite into *d* orbitals during the incoming electron and atomic electron interaction. Therefore, these two opposing corner of the map have different oxidation states and spin states. Another variation in the white line intensity ratio and *O K-edge* pre-peak intensity can be seen in the upper part of the map. Figure 29c) shows the integrated intensities of both *O K-edge* pre-peak intensity and Co white line ratio which exhibits a periodic signal every 3 pixels, or 1.4 nm as shown in Figure 29*c)* and *d)*. But these clusters show a lower white line ratio (high Co oxidation state) and a higher *O K-edge* pre-peak intensity as expected for changes in the cobalt valence states associated with changed in the Sr-doping concentration.

Similar analysis was performed during in-situ cooling experiments and is shown in Figure 30. Figure 30a) shows the integrated *O K-edge* pre-peak intensity, exhibiting fluctuations through the sample while the Co white line ratio fluctuations shown in Figure 30b). Due to the instabilities of the in-situ cooling stage, I was not able to see any possible small range fluctuation as seen at room temperature. However, the chemical and spin state inhomogeneities appearing in the white line ratio and the *O K-edge* pre-peak intensity are obvious. Therefore, cooling cannot overcome the chemical inhomogeneities, such that hole dopants do not migrate at the MIT temperature. The variation in spin state suggests that long range ferromagnetism has not achieved at the temperature, which the cooling holder utilized could reach during the experiment.

4.2.3 EMCD results

The Co-ion spin state and magnetic ordering can also be measured using the electron energy loss magnetic chiral dichroism (EMCD) of transition metal white lines(86). As described in the methods chapter and also in the literature, the Co *L*-edges are measured from two conjugated spots in reciprocal space using the two beam tilting condition. This setup will mimics the two beam polarizations used in X-ray magnetic circular dichroism (XMCD) measurements. The dichroic signal is obtained from the difference between two white line spectra which we name plus and minus here.

First, I perform EMCD measurements in diffraction mode over an area around 100 nm in diameter at room temperature and LN_2 temperature for all three different doping concentrations. In Figure 31, the results of these experiments are shown. In top row, the room temperature results of *x=0.30, 0.17* and *0.05* are shown, while the bottom row shows the LN_2 temperature results. A strong dichroism is observed in the $La_{0.7}Sr_{0.3}CoO_3$ sample at room temperature. As I decrease the doping concentration, the strength of the dichromatic signal decreases at room temperature. On the other hand, lowering the temperature increases the dichromatic signal for all three samples. The $La_{0.7}Sr_{0.3}CoO_3$ sample shows a clear EMCD signal at both temperatures while the weak EMCD signal in the $La_{0.83}Sr_{0.17}CoO_3$ sample at room temperature increases during the in-situ cooling experiment. Finally, the $La_{0.95}Sr_{0.05}CoO_3$ sample does not show any EMCD signal at room temperature while the at LN_2 temperature, there appears to be a very weak EMCD signal.

The observed increase in the EMCD signal upon cooling can be explained by the following. In spite of the existence of the external magnetic field, created by objective lens of the microscope, at above LN_2 temperature, the spin orientations are random. Therefore, at low temperature, I can detect a more dichromatic signal. However, the Sr-doped $LaCoO_3$ system undergoes a spin state transition at low temperature from higher to lower spin state when the doping concentration is less than critical value, $x=0.17$ where the MIT occurs (16). Since the thermally driven spin state transition at low doping concentrations, including $La_{0.95}Sr_{0.05}CoO_3$, is not abrupt, one should still expect to see some Co ion in a higher spin state at LN_2 temperature for $x=0.05$. Additionally, at low temperature, the magnetic field of the objective lens can easily overcome the thermal fluctuations of the overall spin alignment, resulting in a small EMCD signal as shown in Figure 31 for $x=0.17$.

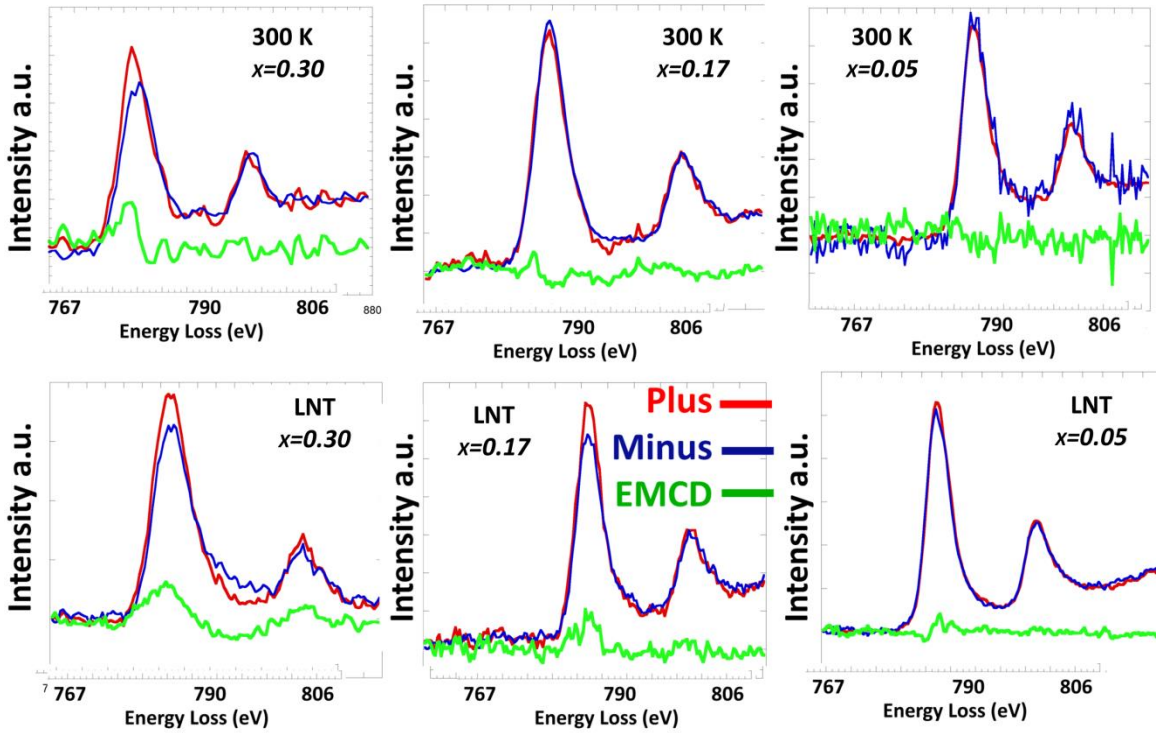

Figure 31 EMCD measurements of *x=0.30*, *x=0.17* and *x=0.05* from left to right at room temperature, at the top row and the Liquid Nitrogen temperature at the bottom row.

To investigate the spatial distribution of the magnetic signal, I combine energy filtered TEM (EFTEM) and EMCD on a nm-scale(105). For the acquisition of the EMCD maps, the single-crystal sample is tilted into the 3 beam condition. Then, the objective aperture is inserted in the back focal plane of the objective lens in order to select the chiral transitions. The elemental maps are taken at three different energies, namely, at Co L_3 pre-edge, at Co L_3 itself and at the post-edge in 2 different reciprocal space positions, as previously described. Pre-edge map is used as the background signal to subtract form L_3 intensity. And the post edge is used to normalize the signal. After this normalization of each signal taken from corresponding reciprocal space position, the magnetic signal is calculated as

the difference between these normalized signals taken from 2 different diffraction positions. An additional normalization is introduced by taking the difference between 2 normalized signals and divided by the summation of the intensities taken from these positions which is given by:

$$\cdot \frac{Intensity_{Plus} - Intensity_{Minus}}{Intensity_{Plus} + Intensity_{Minus}}$$

The result can be seen in Figure 32 for $La_{0.83}Sr_{0.17}CoO_3$ at room temperature. I choose the edge of the sample, as seen in Figure 32a), to avoid the effect of the thickness on the EMCD signal. Figure 32b) shows the EMCD map over the selected region shown in Figure 32a), while Figure 32*c)* and *d)* show a closer look at a selected area and the line intensity profile taken from the EMCD map. Again, two distinct magnetic regimes can be seen in the map: firstly, one region in upper right hand side of the map exhibiting lower EMCD signal. Secondly, the local fluctuations or nonmagnetic islands with the size of more than couple of nm can be seen easily in Figure 32*c)* and *d).*

After excluding random signal distribution from the vacuum, the EMCD signal distributions and the histogram of the sample are shown in Figure 33. I fit the histogram graph with 4 Gaussians and we map their spatial distribution. The center of the first Gaussian, which has 4027 pixels (29% of the sample) is centered around the origin of the EMCD signal axis with *FWHM=0.062*. Similarly, there is second Gaussian is centered at 2.4% EMCD signal with *FWHM=0.032* and represents around 6% of the total sample area. The largest Gaussian, which constitutes around 62% of the entire area that was sampled,

(or 8488 pixel) is centered at 5.3% EMCD signal with *FWHM=0.068*. Lastly, there is fourth Gaussian, centered at 14.1% EMCD signal with *FWHM=0.045*, which makes up 3% of the sample area. This peak is mostly found at the edge of the samples, which I attribute to an artifact of the EMCD measurements. In this analysis, I used Gaussian fit for two reasons: Firstly, the Gaussian distribution is practical and simple since it requires two variables, the average and variance. Secondly, many independent errors stemming from experimental setup and instrumentation, mostly from CCD camera, such as photon noise, digitization noise etc., exhibit a random distribution. Therefore, they are expected to have normal distribution. The three Gaussian fits in the histogram in Figure 33a) suggest the existence of three possible spin states within the sample such that the first fit centered at zero EMCD signal can represent the area with zero spin states while the other two Gaussian curves can responsible for IS and HS states respectively. Therefore, the sample has non-magnetic areas, mostly at upper right corner but also distributed lightly in the rest of the sample, and magnetic areas with different magnetic strengths. This is also a verification of the ELLS map shown in Figure 29.

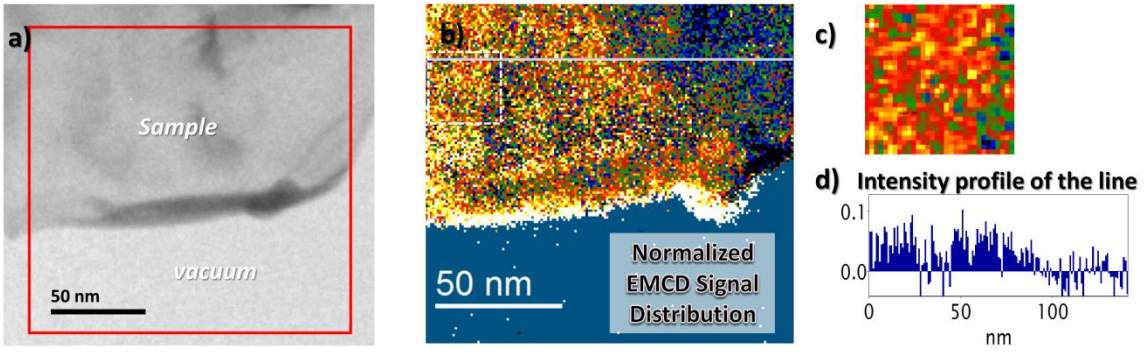

Figure 32 Specially resolved EMCD map of $La_{0.83}Sr_{0.17}CoO_3$

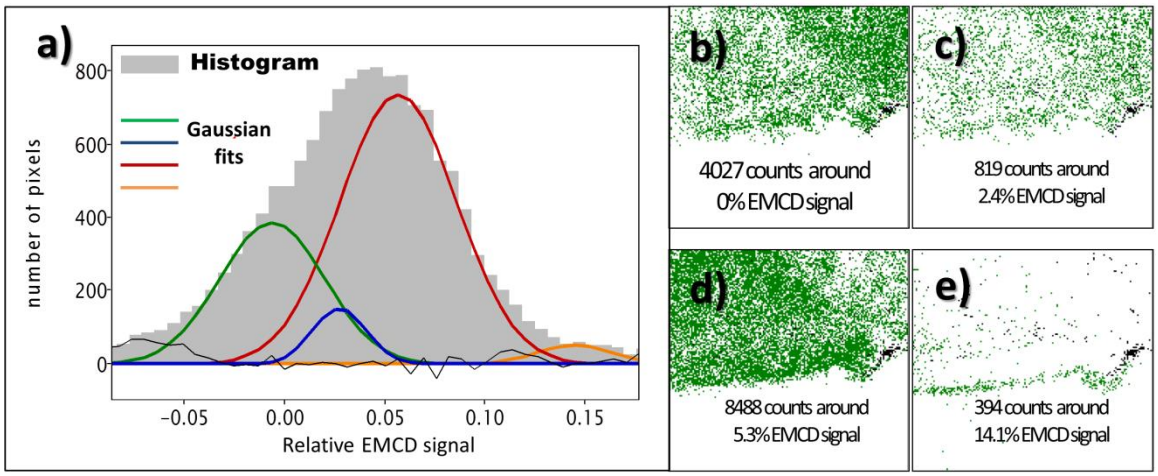

Figure 33 EMCD signal distribution

4.3 Conclusion

In this work, I used different experimental techniques in electron microscopy, namely EELS, HAADF, ABF and EMCD and examined the magnetic transitions and ordering in Sr-doped $LaCoO_3$. I have shown that the CoO_6 octahedral distortions can be measured using HAADF and ABF imaging. I observed that increasing the hole doping changes the octahedral distortion. However, at high dopant level, 30%, material has some areas where the distortions are strong but not well ordered like a checkerboard pattern. Additionally, the atomic-column resolved EELS maps show the oxygen displacement directly. The critically-doped sample, *x=0.17*, shows chemical and magnetic inhomogeneities at room temperature and liquid nitrogen temperature. I utilized the *O K*-edge pre-peak intensity and the Co $L_{3,2}$ intensities to examine these non-uniform distributions. At room temperature, the negative correlation of the short range ordering is the sign of valance ordering in neighboring areas which happens when the sample has relatively homogenous Sr^{2+}

distribution. On the other hand, the larger scale fluctuations in the O *K*-edge pre-peak intensity and the white line ratio stems from the difference in spin states. At liquid nitrogen temperature for *x=0.17*, two kinds of deviation mentioned for room temperature measurement are still observed, which is a sign that the long range ferromagnetic ordering has not been established at the temperature the cooling holder can reach.

Finally, I apply the EMCD method to measure magnetism and find that samples measure at lower temperature and higher hole doping concentrations exhibit a higher dichromatic signal. The EELS maps shows the inhomogeneous nature of the critically doped sample, *x=0.17*. On the other hand, to examine the spin state distribution of 17% doped sample at room temperature, I utilize spatially-resolved EMCD and show the coexistence of LS, IS and HS states. The EMCD signal distribution shows that there are changes in the dichroic signal at two different scales. At the larger scale there are nonmagnetic and magnetic areas, while at the smaller scale the presence of different spin states, such as LS, IS and HS, results in local magnetic clusters. The intermediate spin state is favorable when the t_{2g} e_g crystal splitting symmetry is broken, such that the energy of two t_{2g} and e_g levels becomes comparable and transitions between two levels becomes possible. This is the result of changes in the Co-O bond lengths, of distortions in the CoO_6 octahedra.

5 OXIDATION STATE TRANSITION OF $(Pr_{1-y}Y_y)_{0.7}Ca_{0.3}CoO_3$

5.1 Introduction

So far, doped perovskite cobaltites, such as $La_{1-x}Sr_xCoO_3$, which show rich spin states and electronic configurations, have been studied. Due to energy difference between the crystal splitting and Hund coupling energy, perovskite cobaltites exhibit a spin state transition from intermediate or high spin state (IS; $t^5{}_{2g}e^1{}_g$, $S=1$ or HS; $t^4{}_{2g}e^2{}_g$, $S=2$) to low spin state (LS; $t^6{}_{2g}e^0{}_g$, $S=0$).(8) Recently, the observation of a first-order magnetic/electronic transition in certain Pr-based perovskite cobaltites, such as $Pr_{0.5}Ca_{0.5}CoO_3$, has attracted attention. More specifically, a simultaneous metal to insulator transition (MIT), a sharp drop in magnetic moment upon cooling and a change in the electronic structure has been reported to occur at around 90 K (27) (28). It was suggested that the low-temperature phase in $Pr_{0.5}Ca_{0.5}CoO_3$ is stabilized by a shift of the mixed valence Co^{3+}/Co^{4+} toward pure Co^{3+}, enabled by a valence change of some Pr^{3+} ions to Pr^{4+}, such that these sites absorb some of the holes originally associated with Co sites, or conversely, that electrons are transferred from the Pr *4f* levels into hybridized Co *3d*-O *2p* orbitals.(29) The small difference in energy of the two Pr valence states makes this transition possible. This hypothesis has been confirmed by the occurrence of a Schottky peak in heat-capacity measurements(37) and x-ray absorption spectroscopy at the Pr L_3 edge.(106) (107)

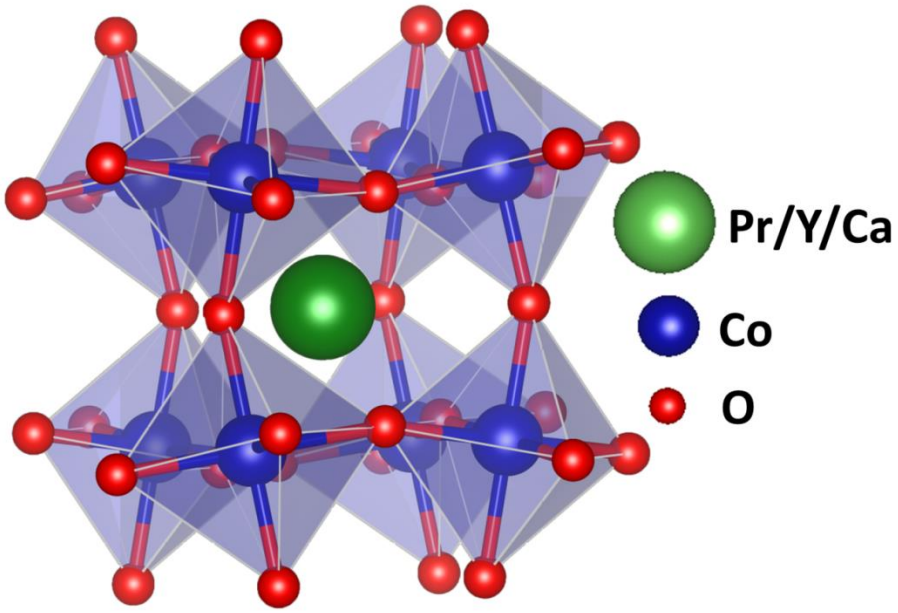

Figure 34 Crystal structure of $(Pr_{1-y}Y_y)_{0.7}Ca_{0.3}CoO_3$

Here, I focus on $(Pr_{1-y}Y_y)_{0.70}Ca_{0.30}CoO_3$ (PYCCO), which exhibits a transition temperature T_{MIT}~*135K* for *y=0.15*(36). Moreover, this particular doping concentration is relatively easy to synthesize since oxygen deficiency and better stoichiometry can be achieved. I will use HAADF imaging in combination with ABF imaging, angular-resolved EELS and *in-situ* cooling experiment in an aberration-corrected scanning transmission electron microscope (STEM), the UIC JEOL ARM200CF, to study $(Pr_{0.85}Y_{0.15})_{0.70}Ca_{0.30}CoO_3$ poly-crystalline samples. I will demonstrate that the electron transfer occurs from the *A* site to the *B* site upon cooling below the transition temperature using in-situ cooling experiment. Furthermore, I will show that oxygen vacancy ordering is closely related to the local Co oxidation state, which changes as a function of temperature.

5.2 Results and Analysis

5.2.1 Room temperature imaging and chemical maps

As suggested by earlier x-ray diffraction measurements,(33) (34) (35) $(Pr_{1-y}Y_y)_{0.70}Ca_{0.30}CoO_3$ has a *(Pbnm)* structure with heavily distorted CoO_6 octahedra (shown in Figure 34). In one of the earliest papers written on this system, *Fujita et al.(36),* proposed that the smaller volume of the CoO_6 octahedra and larger tilting angle of the octahedra increase the MIT temperature. However, direct verification of this hypothesis has been lacking. ABF imaging now provides the opportunity of probing the octahedral environment and identifies the positions of the individual oxygen columns. Atomic-column resolved STEM images are shown in Figure 35 a-c) in the pseudo-cubic [001] and [011] orientations, respectively. In Figure 35*a),* simultaneously acquired HAADF, LAADF and ABF images are combined into a single image where the oxygen columns are seen in yellow. A model of the crystal structure based on the results by *Knizek et al.*(35), is shown as an insert. Atomic-columns resolved EELS maps of Ca, O, Co and Pr in the pseudo-cubic [001] orientation are shown in Figure 35*b).* The combined chemical map of O, Pr and Co in red, green and blue, respectively, is also shown in Figure 35b). Similarly, in Figure 35*c),* an ABF image taken in the pseudo-cubic [011] orientation is shown, highlighting the position of the oxygen atomic columns within the CoO_6 octahedra. The biggest dark spots, labeled in green in the cartoon image inserted, are the A site atomic columns and between the horizontal A site atomic columns Cobalt and Oxygen atoms which create a zigzag pattern due to the octahedral distortion are also clearly resolved.

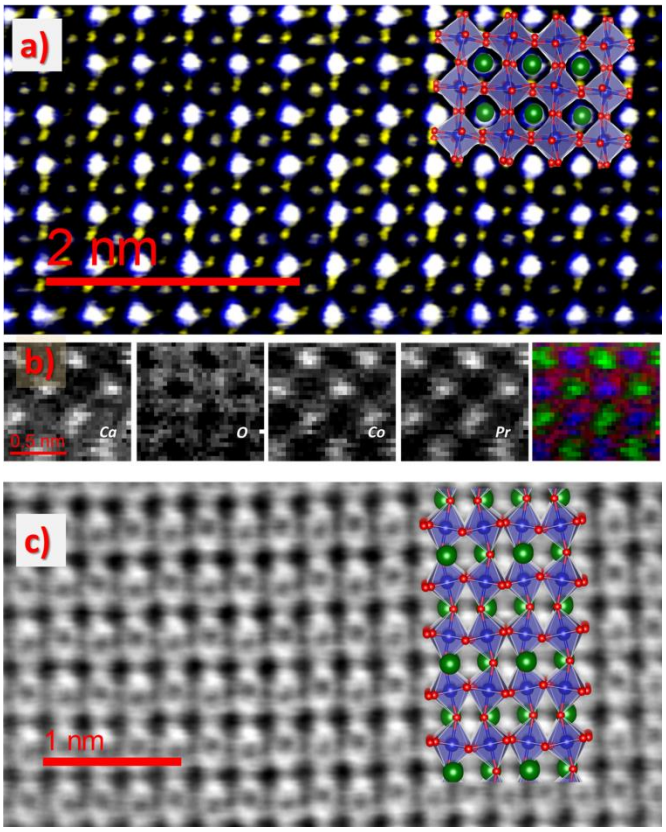

Figure 35 Atomic resolved images of $(Pr_{0.85}Y_{0.15})_{0.70}Ca_{0.30}CoO_3$ in two different orientation, namely [0 0 1] and [0 1 1] pseudo-cubic is shown in *a)* and *c)* respectively. In *a)* HAADF, LAADF and ABF imaging techniques are combined into a single image where the Oxygen columns are in yellow. Atomic resolved EELS map of Ca, O, Co and Pr in [0 0 1] pseudo-cubic orientation are shown in part *b)* respectively from left the right. And the combined chemical map of O, Pr and Co in red, green and blue respectively is in the last window on the left. In *c)* ABF image of $(Pr_{0.85}Y_{0.15})_{0.70}Ca_{0.30}CoO_3$ in pseudo cubic [011] direction. The cartoon which has *Pbnm* crystal symmetry identifying each column inserted is shown. The Octahedral rotation can be seen in the ABF image clearly.

Figure 36*a)* shows the HAADF image of $(Pr_{0.85}Y_{0.15})_{0.7}Ca_{0.3}CoO_3$ in the pseudo-cubic [001] orientation. In this particular area, the crystal lattice exhibits a superstructure, where the *A* site atomic column distances changes periodically from ~0.320 *nm* to ~0.430 *nm* and creates a modulation in intensity along the (010) and (100) pseudo-cubic directions. This observation is confirmed by selected area electron diffraction (SAED), inserted in Figure

36*a)*, where extra diffraction spots at the $[0\,\frac{1}{2}\,0]$ and $[\frac{1}{2}\,0\,0]$ positions are clearly visible, suggesting a modulation with half the frequency of regular atomic spacing in the same direction. On the other hand, the average *A* site bond length perpendicular to the modulation direction remains unchanged at 0.375 *nm*.

In epitaxially strained $LaCoO_3$ thin film grown on $SrTiO_3$ substrate, *Kwon et al.(95)* and *Biškup et al(96)* have report the presence of a similar superstructure. Using electron energy-loss spectroscopy (EELS) of the cobalt *L*-edges and oxygen *K*-edges, *Kwon et al. (95)* conclude that the superstructure is caused by cobalt spin state ordering rather than the oxygen vacancy ordering previously reported in $SrCoO_3$,(97) as well as strained $LaCoO_3$, *(96)*.

To identify the origins of atomic distance modulation in my sample, I examined the local electronic structures using EELS. This kind of modulation has been previously associated with the formation of oxygen vacancies(108) (96) (109) and the origin of magnetic and spin state ordering in other cobaltites.(95) Figure 36*b)* shows the averaged EEL spectrum image of the integrated intensities for the *O K-*, *Pr M-*, *Ca L-* and *Co L*-edges. The map is acquired from the area shown in Figure 36*a)* and integrated vertically to get a horizontal line map. It can be clearly seen that the Pr, Co and Ca signals oscillate periodically as the electron beam probes the respective atomic columns in the [001] direction. However, the *O K*-edge signal appears to decrease significantly at the location of the dark stripes, indicating the presence of oxygen vacancies in the dark stripes. In addition to the lower *O* signal, a comparison of *Co L-edge* fine structure taken from Co atomic position in the dark and the brighter stripes is shown in Figure 36 *d),* exhibiting a clear change in the Co L_3/L_2

intensity ratio, which probes the Co oxidation state(9). At the dark stripes, the white line ratio is higher which is associated with lower oxidation state, and at the bright region, oxidation state of Co is higher which verifies the oxygen vacancy ordering at the dark stripes. Therefore, my EELS map reveals that the observed *A* site distance modulation and B-site intensity modulation is due to oxygen vacancy and Co oxidation state ordering. The observed structure resembles that of the well-known brownmillerite structure,(110) where oxygen vacancies order in every second CoO plane that lies parallel to the pseudo-cubic [001] planes. The oxygen deficient CoO planes contain tetrahedrally coordinated Co while the other planes remain stoichiometric and Co remains octahedrally coordinated. However, no sign of the spin state ordering in the superstructure is found.

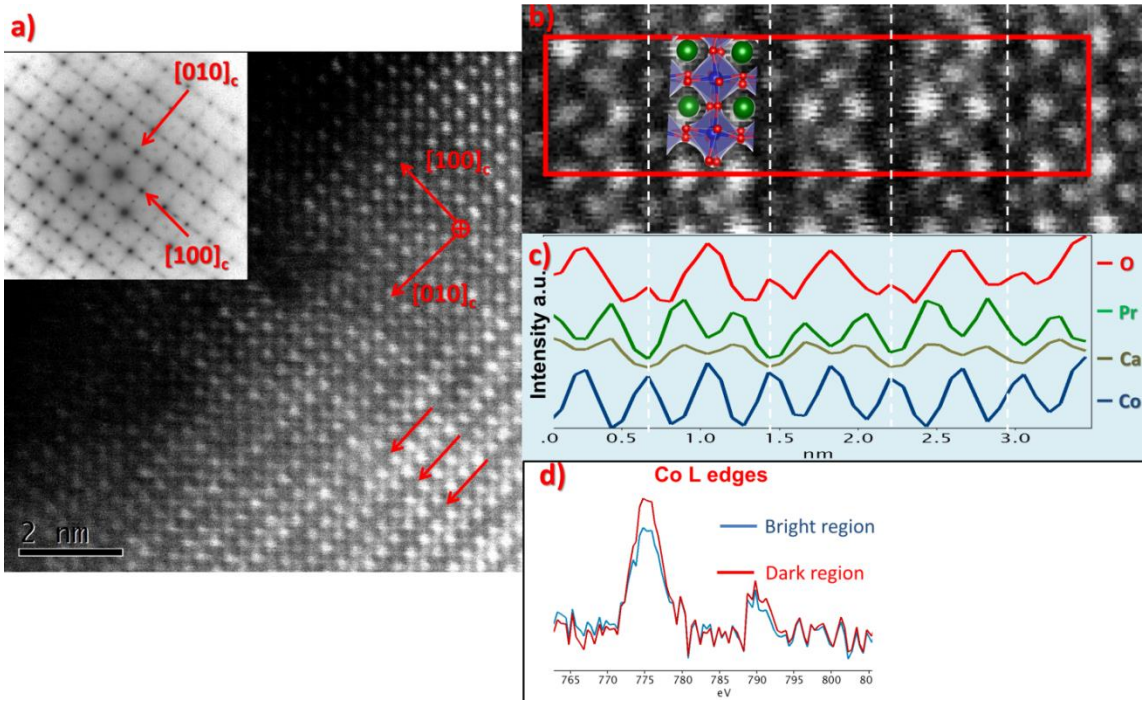

Figure 36 Some local dark stripes are seen in the HAADF image in pseudo-cubic [001] zone axis in *a)* with the SADP inserted where the extra satellite spots are visible in [1/2 0 0] and [0 1/2 0] directions stemming from the dark stripes. In *b)* a closer look to the dark stripes where an EELS map taken inside the rectangle and integrated over the vertical direction as shown in part c*)*. The

comparison of *Co L-edges* taken from the dark stripes and bright region which shows that L_3 intensity is lowered in bright region is represented in part *d)*.

5.2.2 Cooling experiment results

Atomic-column resolved HAADF and ABF images in the pseudo-cubic [001] direction during the in-situ cooling experiments to liquid nitrogen temperature are seen in Figure 37. Due to the thermal instabilities of the cooling stage, the image resolution is degraded slightly and the ABF images do not show the oxygen atomic columns. However, the Co atomic columns are clearly resolved during the in-situ cooling experiment, and some contrast modulations of the CoO planes are still visible. For a more reliable approach to quantifying the structural changes especially at low temperature, where the sample vibration prevents an accurate determination of the atomic column location, we use selected area diffraction (SAD). Figure 38 shows the structural changes as the result of the in-situ cooling of an area that exhibited a high concentration of oxygen vacancy ordering at room temperature. In Figure 38 *a)*, the SADP is shown in the pseudo-cubic [001] direction before the cooling experiment, showing the regular *Pbnm* symmetry diffraction spots, as well as the extra spots associated with the observed oxygen vacancy ordering. SADP taken at LN_2 temperature is shown in Figure 38 *b)*, where the Pbnm symmetry remains unchanged but the intensity of the superlattice spots is greatly decreased, indicating the oxygen vacancy ordering is less prominent below the MIT. To demonstrate the reproducibility of the room temperature oxygen vacancy ordering, additional SADP are taken at room temperature following the in-situ cooling experiments. As can be seen in Figure 38 *c)*, the superlattice spots appear strong again, indicating the oxygen vacancies

are again ordering at room temperature. In addition to the superlattice reflections, we also notice a change in the lattice parameter as a function of temperature. It has been reported that the unit cell volume decreases abruptly below the MIT temperature(35). In Figure 38 *d),* intensity profile of SADP along pseudo-cubic [100] orientation taken at room temperature and LN_2-temperature shows that the atomic spacing decreases at low temperature by around 1.8%, thus verifying that our sample has undergone the MIT, which is expected to occur at T_c=135 K.

My imaging and electron diffraction analysis, therefore, demonstrates that the oxygen vacancy and Co oxidation state ordering, which is observed at room temperature, decreases below the MIT, which has to be associated with the proposed charge transfer between the Co and Pr ions in PYCCO. The observed ordering appears again after the completion of the in-situ cooling experiments, which demonstrates that neither ordering of oxygen vacancies at room temperature, nor the dissolution of the ordered stripes at LN_2 temperature is induced by the electron beam. It is interesting to point out here that the observed effect is opposite of the commonly observed vacancy ordering at low temperature and indicates that the oxygen mobility in PYCCO below the MIT has to be sufficiently large to enable the diffusion of oxygen vacancies from the tetrahedrally coordinated planes to the fully stoichiometric planes.

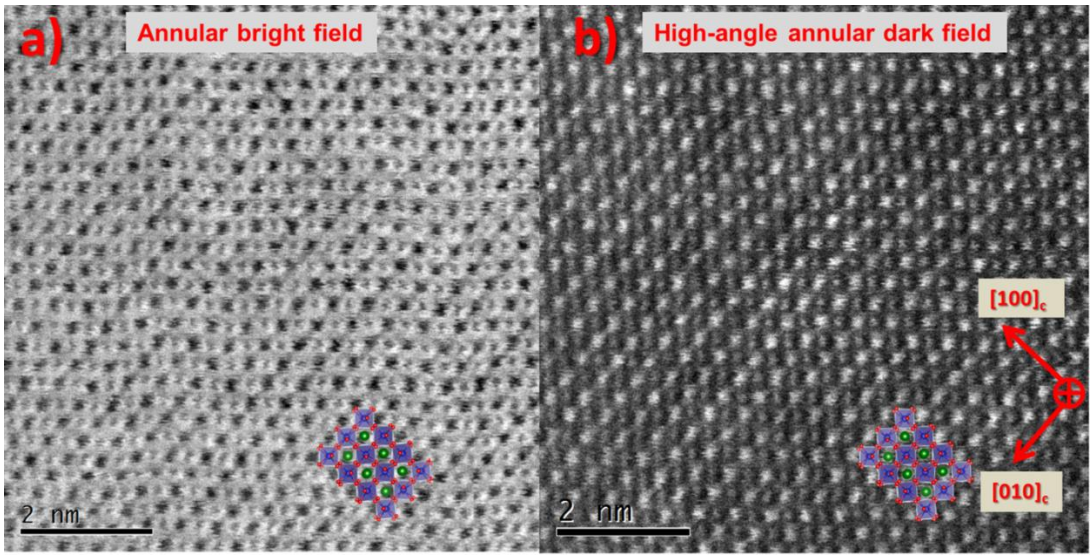

Figure 37 Atomic resolved images of $(Pr_{0.85}Y_{0.15})_{0.70}Ca_{0.30}CoO_3$ in [0 0 1] pseudo-cubic orientation *a)* ABF and *b)* HAADF are shown respectively.

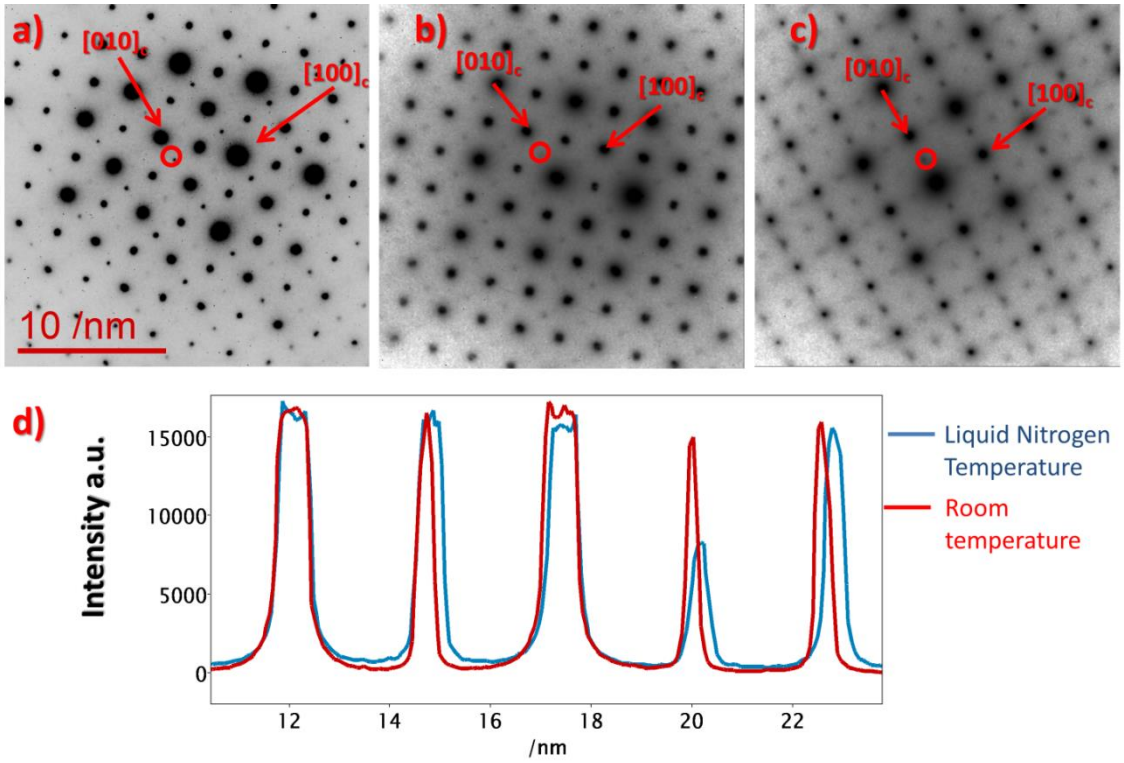

Figure 38 SADP in pseudo-cubic [0 0 1] orientation in the same grain near the dark stripes *a)* before the cooling starts, *b)* when it reached the minimum value, around 90 K, and *c)* after the sample heated up to room temperature are shown. The extra spot which are responsible for the dark stripes are labeled by the circle. In part *d)*, intensity profile of SADP along pseudo-cubic [1 0 0]

orientation taken at room temperature and liquid Nitrogen temperature shows that atomic spacing decreases in low temperature by around 1.8%.

5.2.3 EELS near edge fine structure analysis

To examine the chemical and electronic changes during the cooling experiment, I analyze the ELNES of the Co L-, Pr M and O K-edges (Figure 39). All the EELS spectra shown below are taken from a grain in the pseudo-cubic [001] orientation to avoid any changes in the fine-structure due to the anisotropy of the crystal structure. In perovskite oxides, the O *K*-edges exhibit three peaks near the edge onset, the pre-peak, first and second peak respectively. The O K-edge pre-peak stems from the hybridization of *O 2p* with *Co 3d*, whereas the first peak and the second peak can be assigned to the hybridization of *O 2p* with *Pr 4f* and *Co 4sp*, respectively(9). In Figure 39*a)*, the O *K*-edge spectrum shows two distinct features through cooling. Firstly, the intensity of the first peak increases indicating that there are more available states in the hybridized *O 2p - Pr 4f* orbitals. That is to say, I find that there are fewer electrons in the *Pr 4f* orbital at low temperature. Secondly, the O K-edge pre-peak intensity increases at low temperature and shifts by 0.7 *eV* towards to higher energy. The increase in the pre-peak intensity corresponds to a decrease in the number of electrons in the Co *3d* orbitals. The Co *L*-edge intensities are shown in Figure 39*b)* and can be used to determine the occupancy of the transition metal *3d* orbitals.(101) However, the changes in the Co L_3/L_2 ratio are relatively small as a function of sample temperature. On the other hand, the Pr M_5 at 931 *eV*, and M_4 at 951 *eV* fine structures probe the occupancy of the Pr 4f orbitals as shown in Figure 39c). The Pr *M*-edge fine structure of Pr^{3+} has a shoulder on the low energy side of the M_4 edge, as indicated by the arrow in Figure 39*c)(26).* As the oxidation state of Pr increases to 4+, this shoulder disappears. As

shown in Figure 39c), the Pr M-edge fine-structure clearly shows that the Pr oxidation state increases at low temperature. However, since the changes in the Co L-edge fine-structure are very subtle, I cannot use the Co L_3/L_2 ratio to define the local Co valance state and quantify the Co valence state transition. On the other hand, the O K-edge fine-structure in PYCCO is affected by the valence state transitions of both Pr and Co, and a straight-forward interpretation is not possible. Therefore, I use a series of reference samples to calibrate changes in the O K-edge pre-peak intensity as a function of Co oxidation state.

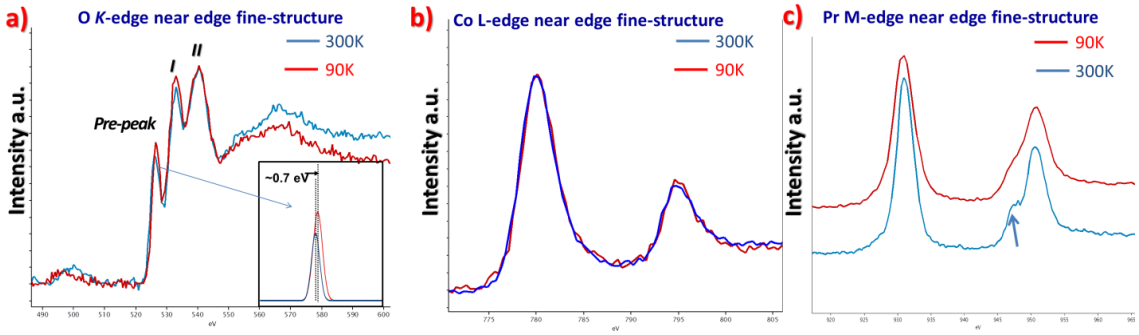

Figure 39 Temperature dependent EELS of $(Pr_{0.85}Y_{0.15})_{0.70}Ca_{0.30}CoO_3$ are shown.

5.2.4 $Pr_{1-x}Ca_xCoO_3$ reference samples

Four reference systems are studies here, namely $Pr_{1-x}Ca_xCoO_3$ for *x=0.3, 0.2, 0.1* and *0.* Above the MIT temperature, I assume that Co oxidation state of $Pr_{1-x}Ca_xCoO_3$ is *(3+x)*, where *x* is the Ca doping concentration. This series of reference samples will now enable me to quantify the changes in the O K-edge fine-structures above the MIT temperature as a function of Ca doping concentration, as thus Co valence state. Figure 40 shows the atomic-column resolved HAADF images of $Pr_{1-x}Ca_xCoO_3$ for *a) x=0.30, b) x=0.20* and *c) x=0.10* respectively. For *x=0.3* and *0.2*, I observe areas with superlattice feature similar to

those found in PYCCO, which we demonstrated to be due to oxygen vacancy ordering. However, as the Ca doping concentration decreases, the concentration of oxygen vacancy ordered domains decreases noticeably. I do not see any indication of existence of this kind of superstructure for *x=0.1* and *x=0*. Similarly, quantitative EELS analysis reveals that higher Ca concentration introduce non-homogeneous oxygen distribution throughout the sample. For *x=0.3* and *0.2*, I observe different oxygen content within the same sample. In Figure 41, the change of the O *K-edge* fine structure is shown as a function of oxygen vacancies. Within the same grain and similar thickness, I found four different areas where oxygen/Co atomic density varies from 2.81 to 3.11. Due to the possible inhomogeneous spatial distribution of Ca and Pr, I choose Co to normalize the oxygen content. To avoid beam damage, I continuously scan the electron probe and make sure there is no beam damage occurs while acquiring the EELS data since O *K-edge* fine structure is very sensitive to beam damage. After background subtraction, the spectrums are aligned with respect to Co L_3 edge peak. As seen in Figure 41*a),* the O *K*-edge fine structure does not show any significant change in first and second peak while there is a systematic change in integrated pre-peak intensities and pre-peak positions. Gaussian fits for the pre-peak intensities are shown as inserts figure at Figure 41*a).* In the case of higher oxygen vacancy the pre-peak intensity increases and the pre-peak shifts to lower energy. Figure 41*b)* shows the relationship oxygen vacancy and the pre-peak energy with respect to the first peak and the integrated pre-peak intensity. One should note that during the cooling experiment of $(Pr_{0.85}Y_{0.15})_{0.7}Ca_{0.3}CoO_3$, I observe a similar increase in O K edge pre-peak intensity as if there was an increase in oxygen vacancy concentration, however the pre-peak position

shifts towards energy shift at low temperature as opposed to lower energy in the case of oxygen vacancies. Therefore, the result of the cooling experiment cannot be read as an increase of oxygen vacancy concentration.

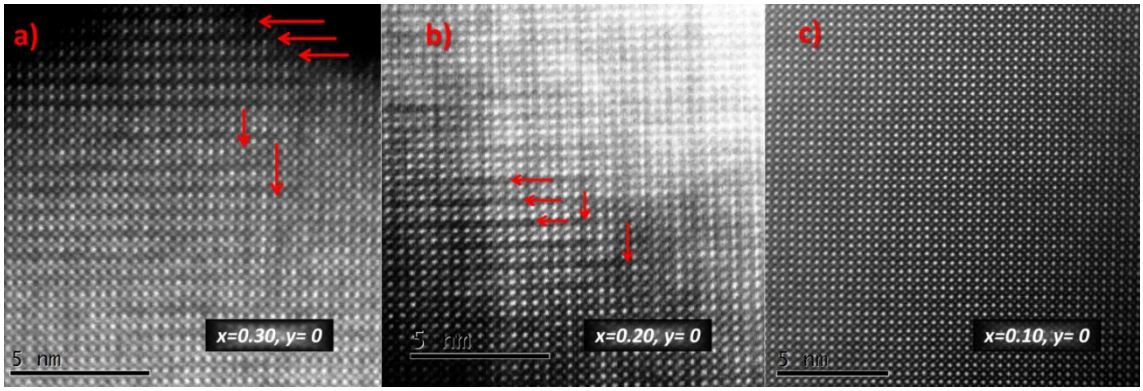

Figure 40 Atomic resolved HAADF images of $Pr_xCa_{1-x}CoO_3$ in pseudo-cubic [001] orientation taken from the areas with dark stripes. For *a) x=0.30, b) x=0.20* and *c) x=0.10*. 10% Ca doped sample does not have dark stripes.

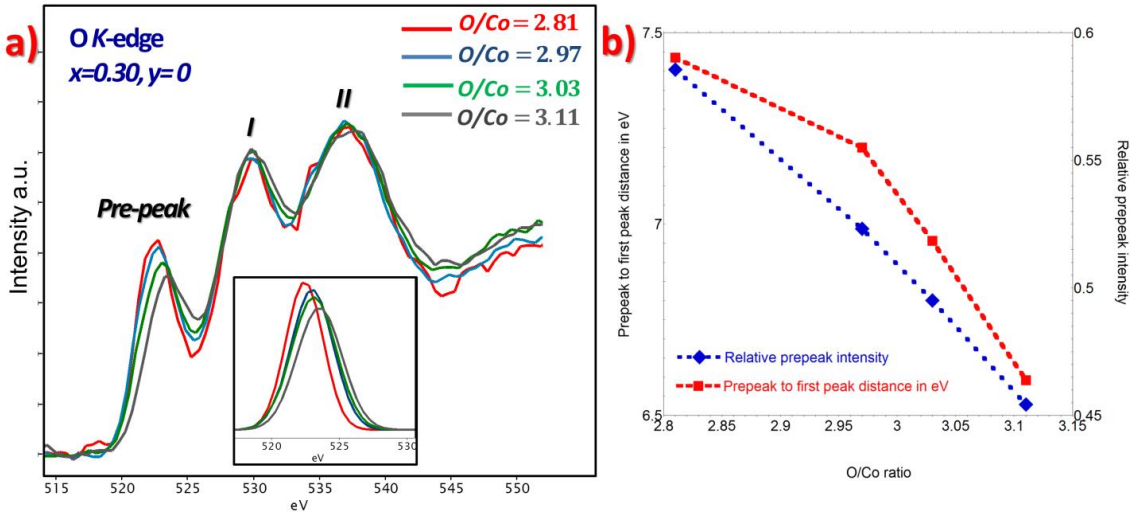

Figure 41 *O K-edge* fine structure of $Pr_{0.7}Ca_{0.3}CoO_3$ as a function of oxygen cobalt atomic ratio is shown in part *a)* where the Gaussian fits for the pre-peak intensity graph is inserted at the lower corner. In part *b)*, integrated *O K-edge* pre-peak intensity *versus O/Co* atomic ratio and the distance between the pre-peak and first peak in *eV versus O/Co* atomic ratio graphs are shown.

I acquired sets of EELS data for the other $Pr_{1-x}Ca_xCoO_3$ samples, and applied an analysis similar to what was shown above for the sample with x=0.3. Since the *O K-edge* fine structure is very sensitive to the oxygen vacancies as shown above, I only pick EELS data with an O/Co atomic ratio of 3.00±0.02 and the results are shown in Figure 42*a)* and Figure 42*b)*. As an effect of the decrease in average Co oxidation state from +3.3 (for *x=0.3)* to *+3.0* (for *x=0)*, the O K-edge pre-peak shifts higher in energy by 0.8 *eV*, while the integrated pre-peak intensity increases. Therefore, I can use this result as a reference to define the Co valence state in $(Pr_{0.85}Y_{0.15})_{0.7}Ca_{0.3}CoO_3$ during the in-situ cooling experiment as summarized in Figure 42*c)*. At room temperature, the *O K-edge* fine structure of $(Pr_{0.85}Y_{0.15})_{0.7}Ca_{0.3}CoO_3$ is almost identical with the $Pr_{0.7}Ca_{0.3}CoO_3$ with $Co^{3.3+}$, while at liquid nitrogen temperature, the O K-edge fine-structure is very close to $PrCoO_3$ with Co^{3+}. Therefore, the transition from $Co^{3.3+}$ to Co^{3+} through in-situ cooling is verified.

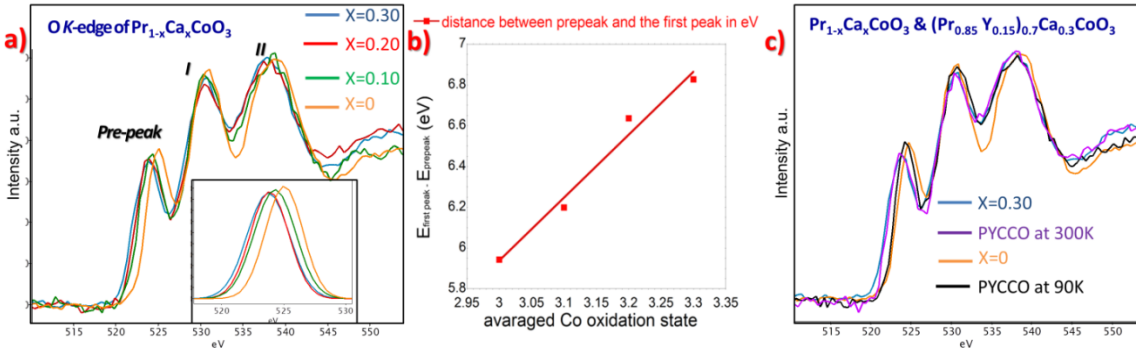

Figure 42 *O K-edge* fine structure of $Pr_{1-x}Ca_xCoO_3$ as a function of Ca doping is shown in part *a)* where the Gaussian fits for the pre-peak intensity graph is inserted at the lower corner. In part *b)*, the distance between the pre-peak and first peak in *eV versus O/Co* atomic ratio graph is shown. Finally in part *c)* the comparison of *O K-edge* fine structures of $(Pr_{0.85}Y_{0.15})_{0.7}Ca_{0.3}CoO_3$ and $Pr_{1-x}Ca_xCoO_3$.

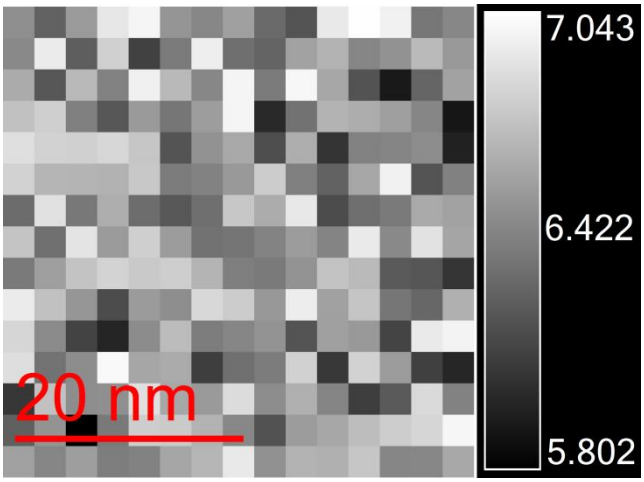

Figure 43 Map of distance between the *O K-edge* pre-peak and the first in *eV* at liquid Nitrogen temperature with average 6.5 *eV* with standard deviation=0.3*eV*.

5.2.5 EELS fine structure map at liquid Nitrogen temperature

Finally, I examine the homogeneity of the valance state transition and the stoichiometry in the bulk of a grain. I applied STEM/EELS mapping of grain in the pseudo-cubic [001] orientation to search for changes in the Co oxidation state at LN_2 temperature. In Figure 43, the map plots the distance between the *O K-edge* pre-peak and the first peak in *eV* over an area 41 *nm* by 41 *nm* in size and 2.7 *nm* pixel step size is shown. Due to spatial drift as a result of the thermal instabilities, the pixel size might be locally different from what is stated above. Nevertheless, the image in Figure 43 clearly shows changes in the O K-edge pre-peak position and thus the local Co oxidation state. That is to say, below the MIT temperature, valance state of the Co ions is not homogeneous through the grains in PYCCO.

5.3 Conclusion

In this work, I utilized different TEM techniques to study changes in the structural and electronic properties of $(Pr_{0.85}Y_{0.15})_{0.70}Ca_{0.30}CoO_3$ across the metal-insulator transition. I directly probe the distortion of CoO_6 octahedra, which stabilize the MIT at higher temperature,(36) by using ABF imaging. My results are in a good agreement with the *Pbnm* crystal symmetry at room temperature. I also observed oxygen vacancy ordering at room temperature, which is observed as a superlattice feature in grains along the [001] orientation. Below the MIT, the oxygen vacancy ordering nearly completely disappears and this process is fully reversed when the temperature reaches room temperature again. In addition, I find that the unit cell volume decreases during cooling which was reported as one of the characteristics of MIT(36) is also observed. The EELS results which show a clear increase in Pr oxidation state at low temperature based on the intensity of the minor peak before Pr M_4 *edg*e while no significant change in Co *L-edges* to determine the any change in Co oxidation state are observed.

Co^{3+} has a more stable electronic configuration than Co^{4+}. Therefore, without chemical or structural constraints, the Co ions tend to adopt the 3+ valance states rather than 4+. I have shown that there are two main changes in crystal structure namely, i) change in the superstructure during the transition which is responsible for oxygen vacancies at room temperature and ii) decrease in the unit cell size during the transition. The existence of vacancy ordering dictates the segregation of Co^{3+} and Co^{4+} and limits the charge transfer. Interestingly, the oxygen mobility in PYCCO below the MIT has to be sufficiently large to enable the diffusion of oxygen vacancies from the tetrahedrally coordinated planes to the

fully stoichiometric planes. Therefore, the sample becomes electronically and structurally more homogenous which reduces the constraints on the Co ions electronic state. Consequently, Co^{3+} becomes more favorable below MIT temperature.

Furthermore, the increase in the O*K-edge* pre-peak intensity can be explained by the following: There are two competing parameters for the pre-peak intensity, i) the electron population of the Co 3*d* levels as the result of a Co valence change and ii) the distribution of Co 3d-electrons in as the result of different Co spin states. At lower spin states, e_g levels are populated less which allows for more available states thereby increasing the O *K-edge* pre-peak intensity. Thus, the Co ions do not experience only valance state transition but also spin state transition.

6 EELS MAP OF TRANSITION METAL OXIDES

6.1 Introduction

The population of a cation's *d* orbitals and the distribution of electrons within those bands determine the physical properties of many oxides in transition metal oxides. To probe the unoccupied *d* band energy levels, one can utilize transition metal L_2 and L_3 edges stemming primarily from the electron transitions of $2p^{3/2}$ and $2p^{½}$ core-shell states into unoccupied 3d orbitals. The resulting *2p* core hole which has an orbital angular momentum *L=1* which then couples to the spin angular momentum *S=1/2* to produce *J = 3/2* and *J=1/2* final states that are directly observable in the *L-edge* spectrum as the two main peaks, namely L_3 and L_2(80). One useful feature of the 3d transition metal *L*-edges is that the L_3/L_2-ratios can be used to identify the oxidation states of the transition metal. If one considers only the occupancy of the initial states, then L_3/L_2-intensity ratio (or white line ratio) should always be two, reflecting the occupancy of the initial *2p* states (i.e. *4/2=2)* However, as a result of spin-spin coupling, the occupancy of the final 3*d* orbital alters the probability for the $2p^{3/2}\rightarrow 3d$ and $2p^{1/2}\rightarrow 3d$ transitions, respectively, and therefore results in different L_3/L_2-ratios for different oxidation states.(74) (75) (43) (101) For different transition metals, the white-line ratio across the 3*d* series increases with *d* occupancy when $n_d<5$, and decreases when $n_d>5$(79). In perovskite oxides, the transition metal *3d-O 2p* hybridization now allows for the *d* orbital occupancy to be probed also by the O *K*-edge, which stems from

transition of the O *1s* to the hybridized O *2p* orbitals (9). The O *K*-edges exhibit three peaks near the edge onset, the pre-peak, first and second peak. The first peak and the second peak of the O *K*-edge can be assigned to the hybridized *O 2p* orbitals with *A* site and transition metal *sp* orbitals, respectively.(9) (76) Additionally, transition metals oxidation states are also correlated to the excitation edge energy position which generally, shifts to a higher energy-loss for a higher oxidation state which is called chemical shift.(111) (112) (78) (77) (104) Furthermore, the local coordination and local crystal distortion have been reported to influence the white line ratio in various perovskite structure.(73) (113)

Atomic-resolution electron energy-loss spectroscopy (EELS) in the scanning transmission electron microscope (STEM) provides us with a direct probe of the structure, chemistry, and electronic properties of materials with single atom sensitivity which is provided by aberration correctors. Moreover, the sub-Å electron probes allow for the regions between two atomic columns to be examined(114). However, the EELS fine structure signal is made up of a complicated convolution of the local electronic states and dynamical electron scattering, such that the coupling with the STEM probe with local orbitals can probe transitions that nobody encountered in an electron microscopy prior to the use of aberration correctors. Recently, a pioneering study combined density functional theory and dynamical electron scattering to calculate the EELS near edge fine structure as a function of probe position.(115)

In this chapter, I will present experimental results showing that the EELS near edge fine structure varies depending on probe position in a variety of *3d*-transition metal perovskite

oxides. I use $(Pr_{0.85}Y_{0.15})_{0.7}Ca_{03}CoO_3$, $La_{1-x}Sr_xCoO_3$, $BiFeO_3$ and $SrTiO_3$ to compare different transition metals and CoO_6 environments. First, the methods utilized in this work are explained and then the experimental results and the conclusion follow.

6.2 Methods

I used the probe size of approximately *0.1 nm* (labeled as *6C)* and 62 *pA* probe current during the EELS maps for optimum current and spatial resolution. The TEM samples are prepared by conventional wedge polishing and low energy argon milling methods. For elemental maps, the exponential background is subtracted just before the individual edges and the integrated signal over 20 *eV* energy window is used. The white line ratios are calculated using the second derivative method, where the second derivative of the spectrum is taken and the total positive signal is integrated for individual edges in such a way that the continuous exponential background, which depends mostly on effective thickness of the sample, does not affect the result.

6.3 Results and Discussion

I will begin my discussion with cobalt oxides which have complex Co spin states and oxidation states. Combined elemental EELS map of $(Pr_{0.85}Y_{0.15})_{0.7}Ca_{03}CoO_3$ taken in the pseudo-cubic [001] orientation is presented in Figure 44*a)* where O, Co and Pr are labeled with blue, green and red respectively. Separate maps for the individual edge are shown in Figure 44*b), c)* and *d)* for O K-edge, Co-L edges and Pr-M edges, respectively. The map of Co L_3/L_2 ratio, white line ratio, is displayed in Figure 44*e),* where a clear dependence of the white line ratio is seen as a function of probe position. More specifically, the white line

ratio is higher at the Co atomic columns while the minimum is observed at Pr/Ca atomic columns. To further highlight these differences, Figure 44*f)* two raw spectra taken at the Pr/Ca and Co atomic column position, as indicated by the colored circles in Figure 44*e)*. The white line map and the Co elemental map look very similar, since the white line ratio has its maxima at Co atomic columns.

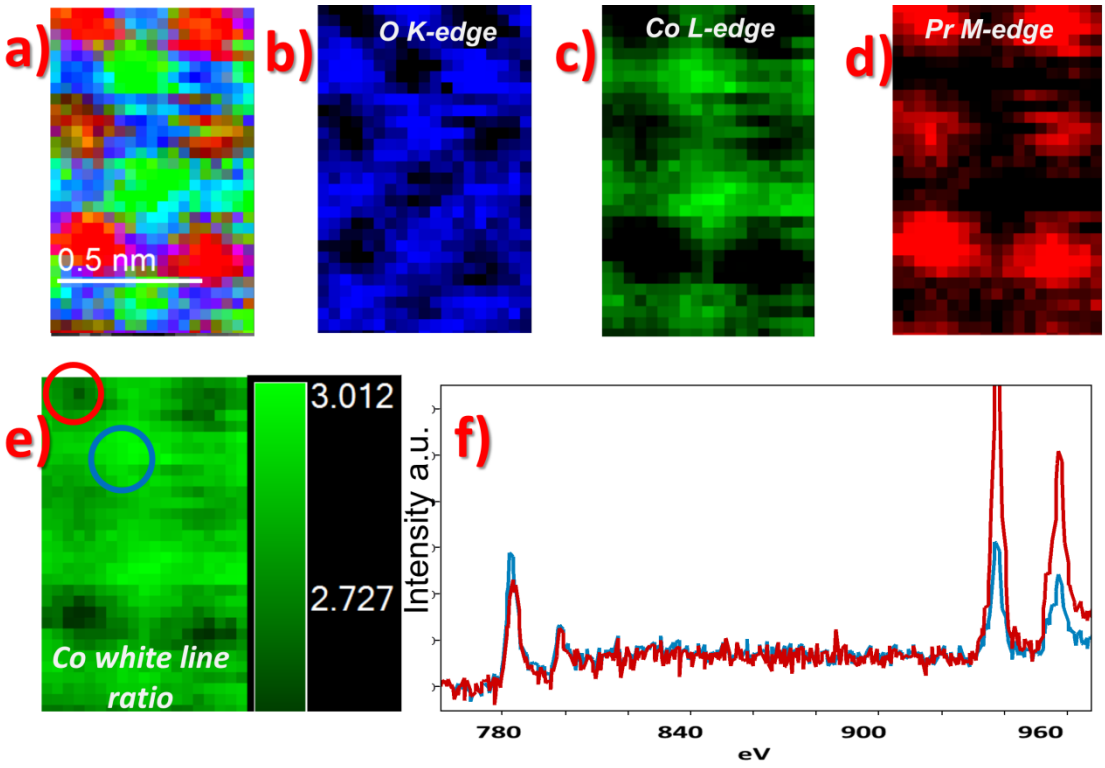

Figure 44 Atomic resolved EELS map of $(Pr_{0.85}Y_{0.15})_{0.7}Ca_{03}CoO_3$ in pseudo cubic [001] direction. The combined chemical map is shown in *a)*. EELS maps of O *K-edge*, Co L_{23} *edges* and Pr M_{34}*edges* are shown in *b), c)* and *d)* respectively. Co white line ratio deviation is displayed in *e)* while a comparison of Co and Pr edges taken from red and blue circles is shown in *f)*.

The other Co system I examined is $La_{1-x}Sr_xCoO_3$, which exhibits numerous temperature induced Co-ion spin state transitions, magnetic transitions, as well as changes in the valance states, depending on the Sr-doping concentration. For my purposes here, I took the

elemental EELS maps in pseudo-cubic [011] direction for *x=0.30* and the results are shown in Figure 45. Similar to the previous result, the combined map, O K-edge, Co-L edges and La-M edges are shown in Figure 45*a), b), c)* and *d)* with the color code that blue for O, green for Co and red for La. In this particular sample, the white line map, seen in Figure 45*f)*, does not show a strong contrast on and off the Co atomic columns although the white line ratio changes over the sample, such that it is lower at oxygen atomic columns and higher at mixed Co-La/Sr columns, which can be seen directly in Figure 45*g)* where two spectrum, red and blue, taken from an area shown in Figure 45f).

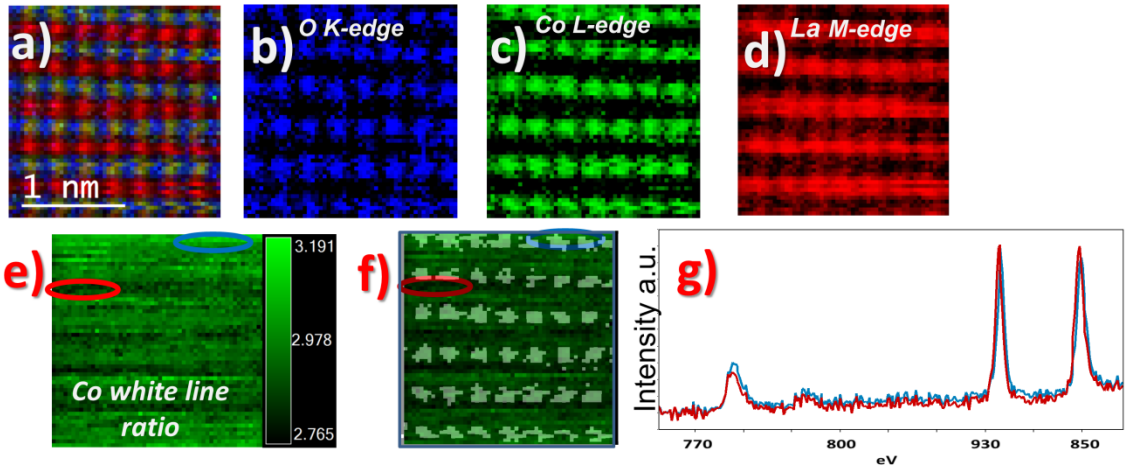

Figure 45 Atomic resolved EELS map of $La_{0.7}Sr_{0.3}CoO_3$ in pseudo cubic [011] direction. The combined chemical map is shown in *a)*. EELS maps of O *K-edge*, Co L_{23} *edges* and La M_{34}*edges* are shown in *b), c)* and *d)* respectively. Co white line ratio deviation is displayed in *f.* A comparison of Co and La edges taken from red and blue circles is shown in *g).* Finally in part *h)* the combined Co atomic columns and the white line ratio is shown.

In Figure 45h), a combined image of Co atomic position with Co white line map in the background is seen. Another feature observed in this sample which is shown in Figure 45*e).* I map the O K-edge pre-peak intensity which is normalized with respect to the total O K

edge intensity as seen in Figure 45e*)*. The O K-edge pre-peak intensity exhibits an intensity minimum at the O atomic columns and creates circular minima.

The next Co oxide is $La_{0.83}Sr_{0.17}CoO_3$ of which results are shown in Figure 46. Similarly, the combined elemental map, O K-edge, Co-L edges and La M-edges maps are shown in blue for O, green for Co and red for La in Figure 46*a), b), c)* and *d).* In Figure 46 *e)* and *f),* Co white line ratio map and individual spectra are shown. Similar to the $PrCaCoO_3$ sample, the white line ratio has local maxima at Co atomic columns. Finally, in Figure 46*g),* the O K-edge intensity normalized by the total O K-edge signal is shown. Again, the O atomic columns have the lowest relative pre-peak intensity.

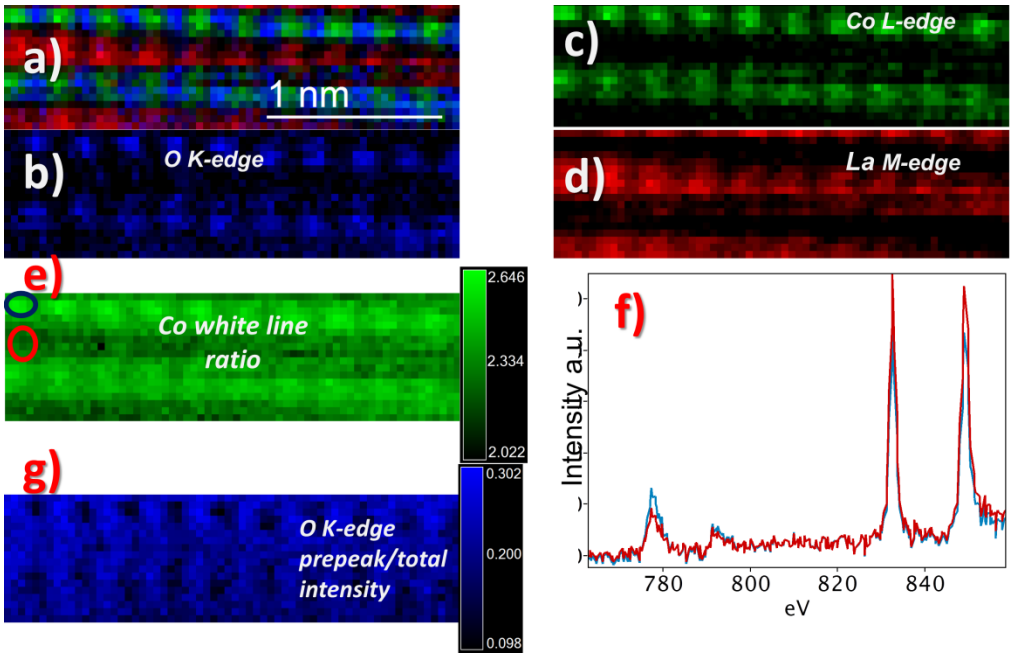

Figure 46 Atomic resolved EELS map of $La_{0.83}Sr_{0.17}CoO_3$ in pseudo cubic [011] direction. the combined chemical map is shown in *a).* EELS maps of O *K-edge*, Co L_{23} *edges* and La M_{34}*edges* are shown in *b), c)* and *d)* respectively. Co white line ratio deviation is displayed in *e)* while a comparison of Co and La edges taken from red and blue circles is shown in *f).* Finally in part *g)* the relative O*K-edge* pre-peak intensity map normalized by total *K-edge* is displayed.

The final cobalt oxide example is $La_{0.95}Sr_{0.05}CoO_3$, which is shown in the pseudo-cubic [011] direction in Figure 47. The combined elemental map, shown in Figure 47 *a)*, consisting of O *K*-edge, Co *L*-edge and Pr *M*- edge maps, labeled in blue, green and red color, respectively. O and Co chemical maps are also displayed separately in Figure 47*b)* and c*).* Figure 47*d)* shows a map of the relative O *K*-edge pre-peak intensity which is normalized by the total O K edge intensity. The pre-peak is minimum around the O atomic columns, while the Co L_3/l_2 ratio varies depending on the probe position, as seen in Figure 47 *e)* and *f).* The minima of the white line ratio map coincide with the Co atomic columns in this case. The line profile of Co intensity and the white line ratio taken from the gray line at Co elemental map and white line ratio map is shown in Figure 47 *f).* The maximum of white line ratio signals coincides with the O atomic columns. On the other hand, La/Sr atomic columns have the minima in the Co white line ratio which can be seen in Figure 47 g).

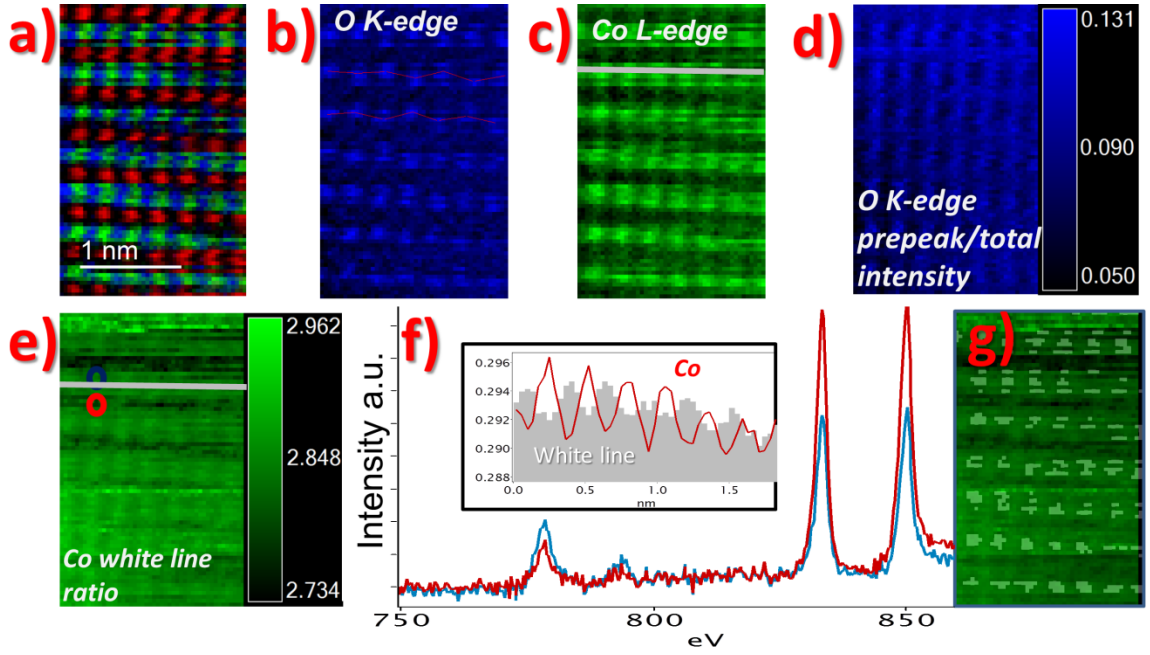

Figure 47 Atomic resolved EELS map of $La_{0.95}Sr_{0.05}CoO_3$ in pseudo cubic [011] direction. The combined chemical map is shown in *a)*. EELS maps of O *K-edge*, and Co L_{23} *edges* are shown in *b)*, and *c)* respectively. In part *d)* the relative O*K-edge* pre-peak intensity map normalized by total *K-edge* is displayed. Co white line ratio deviation is displayed in *e)* while a comparison of Co and La edges taken from red and blue circles is shown in *f)*. The line profile of White line ratio and co elemental intensity taken from the gray line in *c)* and *e)* is inserted into *f)*. In part *g)*, a combined map of Co atomic column and the white line ratio.

The next perovskite oxide is $BiFeO_3$, which is shown in the pseudo-cubic [001] orientation in Figure 48. An elemental map of O K-edge and Fe L-edges and Fe white line map are displayed Figure 48 *a)*, *b)* and *c)* respectively. In this sample, there is a difference in the total O *K*-edge total intensity, but I do not observe any change in fine structure of the O *K*-edge, as seen in Figure 48*d)* as a function of probe position. However, the Fe white line ratio fluctuations are clearly observed in Figure 48*e)*.

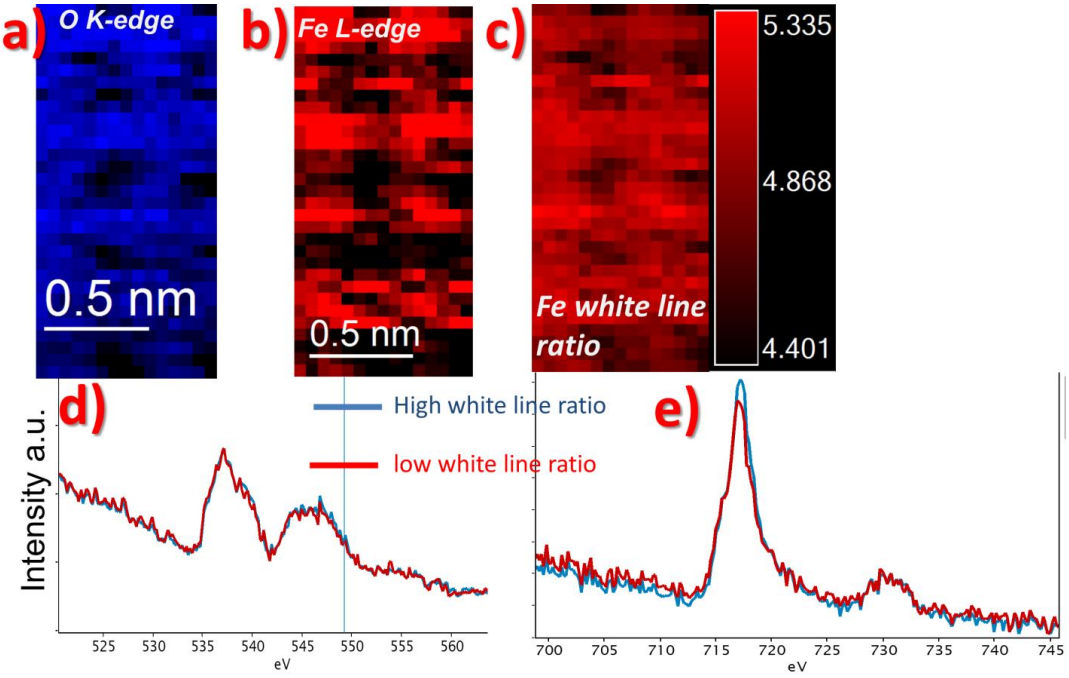

Figure 48 Atomic resolved EELS map of $BiFeO_3$ in pseudo cubic [001] direction. EELS maps of O *K-edge*, and Fe L_{23} *edges* are shown in a*)*, and *b)* respectively. Fe white line ratio deviation is displayed in *d)* while comparisons of O and Fe edges taken from regions with high white line ratio and low white line ratio are shown in *d)* and *e)* respectively.

Finally, I examine $SrTiO_3$, which is shown in the [001] projection in Figure 49. The integrated Ti L-edge intensity map and individual spectra are shown in Figure 49 *b)* and *c)*, respectively. As seen in *c)*, there is no significant difference in fine structure of Ti L-edges taken at Ti, Sr and O atomic columns.

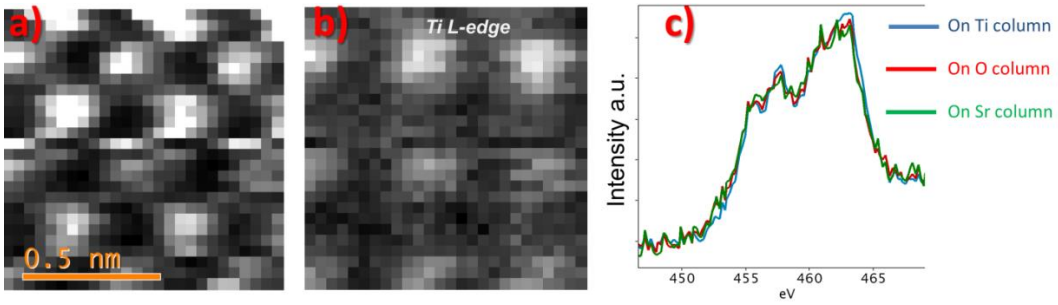

Figure 49 Atomic resolved EELS map of $SrTiO_3$ in [001] direction. Annular dark field (ADF) image taken simultaneously with the EELS data is shown in *a).* EELS map of Ti L_{23} *edges* is shown in b*).* Normalized Ti *L-edges* taken from three different columns are shown in *d).*

To begin this discussion, I will focus on the changes in the normalized *O K* edge pre-peak intensity. In $La_{1-x}Sr_xCoO_3$ system, the low normalized O K-edge pre-peak intensity on O atomic columns can be explained as follows: In the perovskite environment, the pre-peak intensity stems from transitions into the hybridized O *2p* and transition metal *3d* orbitals. For the O *2p* orbitals, the electron wave function is zero at the nucleus. At same time, the initial state for the transition measured by the O K-edge is the symmetric *1s* orbital which is closest to the nucleus and expected to be the most localized. However, the relative pre-peak intensity is at its minima at the O atomic columns. Therefore, I must be probing the final state of the excitation related to pre-peak intensity, namely *O 2p-Co* 3d hybridization. However, in multilayered complex cobalt oxides, it has been reported that the relative pre-peak intensity is localized at the O atomic columns in one layer and completely delocalized in the other one.(116) In my thesis, I can clearly see that the relative O *K*-edge pre-peak intensity is not localized. The result suggests that the relative O *K*-edge pre-peak intensity may provide free electron-hole motion between neighboring Co ions which can be related to double-exchange or super-exchange mechanisms associated with ferromagnetic or anti-ferromagnetic ordering. It is also interesting to see that as the Sr doping increases, the O *K*-edge pre-peak intensity gets more symmetrical around the O atomic columns.

Until now, the white line ratio of transition metal *L*-edges was considered the ideal measure for its oxidation state. In lower spatial resolution, this approached has worked perfectly, as

also shown in earlier chapters of this thesis. As explained in previous chapters, EELS probes the unoccupied orbitals above Fermi levels. On the other hand, with a sub-atomic spatial resolution, the understanding of the oxidation state map needs to be reexamined. Intuitively, the average oxidation state over a region with multiple atoms, or even a single atom is easy to understand. When we take atomic-column resolved EELS elemental map, or EDS elemental map, we generally detect elemental signal from all parts of the region of interest. However, at the atomic columns, the corresponding elemental edge signal is much higher than other part of the map, which results in the elemental chemical maps shown before. Therefore, in atomic-column resolved EELS maps, we still obtain the La M edge signals from anywhere on the sample, including the on the pure Co columns, oxygen columns or inter atomic region, in the case of $LaCoO_3$. Talking about oxidation state of an ion at a point, where that particular ion is not supposed to be located, appears puzzling. However, we know that atomic columns, which are imaged in TEM or chemical imaging, such like EELS and EDS, refer to the locations of the nucleus of the corresponding atoms. On the other hand, the excitations occurs from inner-shell orbitals. In particular, the experiments done in this chapter show that the white line ratio generally has local maximum at transition metal atomic columns, but sometimes it is not clearly associated with the atomic columns. In $(Pr_{0.85}Y_{0.15})_{0.7}Ca_{03}CoO_3$, $La_{0.83}Sr_{0.17}CoO_3$ and $BiFeO_3$, the white line ratio maxima coincide with the transition metal atomic columns. In $La_{0.7}Sr_{0.3}CoO_3$, however, it is hard to say that there is a one to one correspondence for higher and lower white line ratio for each atomic site. Similarly, for $La_{0.95}Sr_{0.05}CoO_3$, the maxima in the white line ratio signal coincides with O atomic columns and the minimum

is located at the La atomic columns. And finally, $SrTiO_3$ does not show any significant difference in the Ti *L* edges. In $SrTiO_3$, the different oxidation states do not only the change the fine structure but also causes chemical shift which I do not see here.

One can speculate that the fluctuations in the white line ratio as function of probe position stem from the particular orientation and position of the orbitals, which the atomic electrons excite from or into. Such a speculation also requires taking electron channeling effects and also the delocalization of inelastic scattering into account. It has been reported that the spatial localization of the inelastic scattering depends only on the energy loss measured, rather than a details of the material (117) as a consequence of the long-range nature of the electrostatic interaction between the incident electron and the atomic electrons in the samples which can be order of $0.1nm$ at an energy loss of about 700-800 eV. (43)

All in all, having a very small STEM probe requires more precaution as far as interpreting oxidation state maps are concerned. Depending on the probe being at the atomic column or not, the EELS fine structure of the transition metal *L*-edges can be significantly different. Therefore, the interpretation of oxidation state as result of change in the fine structure might be misleading. However, taking a spatial average of the EELS spectrum would lead a more realistic result.

6.4 Conclusion

In this chapter, I have shown the effects of STEM probes which are smaller than the interatomic spacing on the local EELS fine structure in transition metal oxides. I find

systematic change in the transition metal white line ratio within the unit cell of various Co-oxides, which challenges our understanding of the Co L-edge ratio as a measure of the local Co oxidation state. Therefore, my work in this chapter suggests that having a sub-Angstrom size probe, one should reconsider the relationship between the white line ratio and the oxidation state. However, I have only shown the changes in EELS signal as a function of probe position experimentally for some materials. For an extensive model of these observations, theoretical calculations are necessary.

7 CONCLUSION AND OUTLOOK

7.1 Conclusion

Having Co ions with three different spin states, namely LS, IS and HS, with mixed valency, and nonstoichiometric oxygen distribution, cobalt oxides are different from other *3d* metal oxides. The mechanism behind the spin states, oxidation states, their transitions and their relation to the macroscopic physical properties, such as magnetic ordering, metallic behavior etc. are still not well understood. After the recent progress in aberration correctors for transmission electron microscopes, sub-Angstrom probe size with high intensity made very high spatial resolution with high energy resolution possible, which provides us the opportunity of investigating the local structure of materials with high accuracy. In this thesis, complex cobalt oxides are investigated using a combination of aberration corrected scanning transmission electron microscopy, electron energy loss spectroscopy and electron energy loss magnetic circular dichroism.

Having a local probe provided by STEM and EELS techniques, I find a Co-ion spin state transition in 5% doped $La_{1-x}Sr_xCoO_3$ through in-situ cooling experiments, while HAADF images and SADP do not show any indication of changes in crystal structure symmetry for

17% and 30% doped samples. Utilizing the change in the *O K*-edge pre-peak intensity, I concluded that in the 17% and 30% doped samples studied here, the doping driven spin state transition is dominant over thermally driven spin state transition at low temperature.

Additionally, I also have revealed a general trend in the CoO_6 octahedral distortions as function of Sr doping: The average distortion decreases with the Sr doping level. On the other hand, at the highest Sr doping concentration, I have worked with during this thesis, areas with strong CoO_6 distortion are surrounded by larger areas with weaker distortion in opposite direction. In addition to the structure, spatially resolved EELS maps measure the variations in the spin states and electronic configuration of Co ions throughout the sample. I further find that the average dichromatic signals increase with the higher Sr content. More importantly, I have addressed a important question about the Co spin state in $LaCoO_3$. The existence of IS has been a controversy. The spatially resolved EMCD map reveals that, at room temperature, IS exists with LS and HS, which can guide the theoretical calculation to improve our understanding of Co oxides. Also, spatially resolved EMCD directly shows that, at 17% Sr doping, magnetic and nonmagnetic regions coexist, which reveals the percolative nature of emerging long range magnetic ordering.

I also have investigated the valance state transition in $(Pr_{0.85}Y_{0.15})_{0.70}Ca_{0.30}CoO_3$ which has been reported to have a simultaneous metal to insulator transition (MIT) and a sharp drop in magnetic moment upon cooling. In this thesis, for the first time, I measured the local structural and electronic changes in $(Pr_{0.85}Y_{0.15})_{0.70}Ca_{0.30}CoO_3$ as a result of this transition.

I identify the oxidation state of Co, which changes from ~+*3.3* to ~+*3* and the increase in Pr valance state, and utilize the O K edge pre-peak for quantifying the Co oxidation state. My finding show that the structural modulation in [001] direction, which is the effect of oxygen vacancies, become less common during MIT. This unusual behavior is the result of the oxygen vacancies migration during the cooling process which makes the sample chemically more homogenous, in addition to the structural homogeneity at temperature below MIT.

Finally, with the help of aberration-corrected microscopy, I presented experimental results showing that the EELS near edge fine structure varies in 3d-transition metal perovskite oxides depending on position of probe when it is smaller than the interatomic spacing., In particular, I have observed that, in some particular transition metal oxides, the white line ratio of transition metal oxide changes when the probe is not located on the atomic column. This part of my research suggests that the concept of oxidation state-white line ratio needs to be revised when very high spatial resolution is achieved. At lower spatial resolution, this effect does not appear to be not a problem . Additional theoretical modeling is required to fully understand these effects.

7.2 Outlook

During the course of this research, potential areas for expansion and improvement became apparent. The local CoO_6 distortion in $La_{1-x}Sr_xCoO_3$ is quantified at room temperature and

atomic-column resolved in-situ cooling imaging is achieved. However, the O columns are not resolved at low temperature due to the thermal instabilities. Imaging lighter elements at low temperature is one of the holy grails of cooling experiment with TEM. To understand the temperature dependent spin state and magnetic transition completely, quantification of local CoO_6 distortion is vital.

Moreover, my research suggests the coexistence of LS, IS and HS state of Co ions of $La_{0.83}Sr_{0.17}CoO_3$ at room temperature. Spatially-resolved EMCD measurements should be applied for the sample with different hole dopants and at low temperature.

In-situ heating experiments can help to improve our understandings of spin state mechanism of $La_{1-x}Sr_xCoO_3$ due to the expected the thermally driven spin state transition to high spin. With the help of new generation monochromatic STEM, low-loss EELS can be acquired with much higher energy resolution allowing the spin polarons to be studied using low-loss EELS.

During the cooling experiment of $(Pr_{0.85}Y_{0.15})_{0.70}Ca_{0.30}CoO_3$, partial electron transfer from Pr to Co ion is observed. To improve our understanding, specimen with different *Y* and *Ca* doping concentration should be examined. $Pr_{1-x}Ca_xCoO_3$ with $x<0.5$ is claimed to have similar transition during cooling when external pressure is applied. Thin film specimen grown on the suitable substrates can provide such pressure for TEM analysis.

As far as TEM techniques are concerned, this work suggested that sub-atomic chemical EELS maps require extensive modeling. The experiments done in the last chapter of this thesis are very interesting and hint at that we need to revise our understanding of valance

state maps using the transition metal *L*-edge. However, extensive theoretical calculations are necessary to provide a better understanding of what is observed here experimentally and the current DFT modeling approaches might not be sufficient in strongly correlated systems.

8 REFERENCES

1. Petric A, Huang P, Tietz F. Evaluation of La–Sr–Co–Fe–O perovskites for solid oxide fuel cells and gas separation membranes. Solid State Ionics. 2000;135(1–4):719-25.
2. Klie RF, Qiao Q, Paulauskas T, Gulec A, Rebola A, Ogut S, et al. Observations of Co^{4+} in a Higher Spin State and the Increase in the Seebeck Coefficient of Thermoelectric $Ca_3Co_4O_9$. Physical Review Letters. 2012;108(19):196601.
3. Klie RF, Gupta A, Mazumdar D, inventorsHigh-Efficiency Thin Film Materials For High-Temperature Thermo-Electric Energy. USA2012.
4. Goodenough JB. An interpretation of the magnetic properties of the perovskite-type mixed crystals La1−xSrxCoO3−λ. Journal of Physics and Chemistry of Solids. 1958;6(2–3):287-97.
5. Raccah PM, Goodenough JB. First-Order Localized-Electron Collective-Electron Transition in $LaCoO_3$. Physical Review. 1967;155(3):932.
6. Señarís-Rodríguez MA, Goodenough JB. Magnetic and Transport Properties of the System La1-xSrxCoO3-δ (0 < x ≤ 0.50). Journal of Solid State Chemistry. 1995;118(2):323-36.
7. Haverkort MW, Hu Z, Cezar JC, Burnus T, Hartmann H, Reuther M, et al. Spin State Transition in $LaCoO_3$ Studied Using Soft X-ray Absorption Spectroscopy and Magnetic Circular Dichroism. Physical Review Letters. 2006;97(17):176405.
8. Korotin MA, Ezhov SY, Solovyev IV, Anisimov VI, Khomskii DI, Sawatzky GA. Intermediate-spin state and properties of $LaCoO_3$. Physical Review B. 1996;54(8):5309-16.
9. Klie RF, Zheng JC, Zhu Y, Varela M, Wu J, Leighton C. Direct Measurement of the Low-Temperature Spin-State Transition in $LaCoO_3$. Physical Review Letters. 2007;99(4):047203.
10. Fita I, Markovich V, Mogilyansky D, Puzniak R, Wisniewski A, Titelman L, et al. Size- and pressure-controlled ferromagnetism in $LaCoO_3$nanoparticles. Physical Review B. 2008;77(22):224421.
11. Fuchs D, Pinta C, Schwarz T, Schweiss P, Nagel P, Schuppler S, et al. Ferromagnetic order in epitaxially strained $LaCoO_3$ thin films. Physical Review B (Condensed Matter and Materials Physics). 2007;75(14):144402-5.
12. Klie RF, Yuan T, Tanase M, Yang G, Ramasse Q. Direct measurement of ferromagnetic ordering in biaxially strained $LaCoO_3$ thin films. Applied Physics Letters. 2010;96(8):082510-3.
13. Zhou JS, Yan JQ, Goodenough JB. Bulk modulus anomaly in RCoO3 (R=La, Pr, and Nd). Physical Review B. 2005;71(22):220103.

14. Lugovy M, Slyunyayev V, Orlovskaya N, Verbylo D, Reece MJ. Room-temperature creep of $LaCoO_3$-based perovskites: Equilibrium strain under compression. Physical Review B. 2008;78(2).
15. Sundaram N, Jiang Y, Anderson IE, Belanger DP, Booth CH, Bridges F, et al. Local Structure of La1-xSrxCoO3 Determined from EXAFS and Neutron Pair Distribution Function Studies. Physical Review Letters. 2009;102(2):026401.
16. Smith RX, Hoch MJR, Moulton WG, Kuhns PL, Reyes AP, Boebinger GS, et al. Evolution of the spin-state transition with doping in La1-xSrxCoO3 Physical Review B. 2012;86(5):054428.
17. Smith RX, Hoch MJR, Kuhns PL, Moulton WG, Reyes AP, Boebinger GS, et al. Spin polarons in La1−xSrxCoO3 single crystals. Physical Review B. 2008;78(9):092201.
18. He C, El-Khatib S, Wu J, Lynn JW, Zheng H, Mitchell JF, et al. Doping fluctuation-driven magneto-electronic phase separation in La 1− x Sr x CoO 3 single crystals. EPL (Europhysics Letters). 2009;87(2):27006.
19. Podlesnyak A, Russina M, Furrer A, Alfonsov A, Vavilova E, Kataev V, et al. Spin-State Polarons in Lightly-Hole-Doped LaCoO3. Physical Review Letters. 2008;101(24):247603.
20. Wu J, Leighton C. Glassy ferromagnetism and magnetic phase separation in La1-xSrxCoO3. Physical Review B. 2003;67(17):174408.
21. Caciuffo R, Rinaldi D, Barucca G, Mira J, Rivas J, Señarís-Rodríguez MA, et al. Structural details and magnetic order of La1-xSrxCoO3. Physical Review B. 1999;59(2):1068-78.
22. Takami T, Zhou JS, Goodenough JB, Ikuta H. Correlation between the structure and the spin state in $R_{1-x}\ Sr_x\ Co\ O_3$, (R = La, Pr, and Nd). Physical Review B. 2007;76(14):144116.
23. Haas O, Struis RPWJ, McBreen JM. Synchrotron X-ray absorption of LaCoO3 perovskite. Journal of Solid State Chemistry. 2004;177(3):1000-10.
24. Fuchs D, Arac E, Pinta C, Schuppler S, Schneider R, v. Löhneysen H. Tuning the magnetic properties of LaCoO3 thin films by epitaxial strain. Physical Review B. 2008;77(1):014434.
25. Lee Y, Harmon BN. Rhombohedral distortion effects on electronic structure of LaCoO3. Journal of Applied Physics. 2013;113(17):-.
26. Richter J, Braun A, Harvey AS, Holtappels P, Graule T, Gauckler LJ. Valence changes of manganese and praseodymium in Pr1−xSrxMn1−yInyO3−δ perovskites upon cation substitution as determined with XANES and ELNES. Physica B: Condensed Matter. 2008;403(1):87-94.
27. Tsubouchi S, Kyômen T, Itoh M, Ganguly P, Oguni M, Shimojo Y, et al. Simultaneous metal-insulator and spin-state transitions in Pr0.5Ca0.5CoO3. Physical Review B. 2002;66(5):052418.
28. Saitoh T, Yamashita Y, Todoroki N, Kyômen T, Itoh M, Higashiguchi M, et al. Simultaneous spin-state-insulator–metal transition in Pr0.5Ca0.5CoO3. Journal of Electron Spectroscopy and Related Phenomena. 2005;144–147(0):893-5.
29. Knížek K, Hejtmánek J, Novák P, Jirák Z. Charge transfer, valence, and the metal-insulator transition in Pr0.5Ca0.5CoO3. Physical Review B. 2010;81(15):155113.

30. Masuda H, Fujita T, Miyashita T, Soda M, Yasui Y, Kobayashi Y, et al. Transport and Magnetic Properties of R1-xAxCoO3 (R = La, Pr and Nd; A = Ba, Sr and Ca). Journal of the Physical Society of Japan. 2003;72(4):873-8.
31. Herrero-Martín J, García-Muñoz JL, Valencia S, Frontera C, Blasco J, Barón-González AJ, et al. Valence change of praseodymium in Pr0.5Ca0.5CoO3 investigated by x-ray absorption spectroscopy. Physical Review B. 2011;84(11):115131.
32. Guillou F, Zhang Q, Hu Z, Kuo CY, Chin YY, Lin HJ, et al. Coupled valence and spin state transition in (Pr0.7Sm0.3)0.7Ca0.3CoO3. Physical Review B. 2013;87(11):115114.
33. Hejtmánek J, Šantavá E, Knížek K, Maryško M, Jirák Z, Naito T, et al. Metal-insulator transition and the Pr3+/Pr4+ valence shift in (Pr1−yYy)0.7Ca0.3CoO3. Physical Review B. 2010;82(16):165107.
34. Phelan D, Bhatti KP, Taylor M, Wang S, Leighton C. Magnetically inhomogeneous ground state below the first-order valence transition in (Pr1−yYy)0.7Ca0.3Co. Physical Review B. 2014;89(18):184427.
35. Knížek K, Hejtmánek J, Maryško M, Novák P, Šantavá E, Jirák Z, et al. Spin-state crossover and low-temperature magnetic state in yttrium-doped Pr0.7Ca0.3CoO3. Physical Review B. 2013;88(22):224412.
36. Fujita T, Miyashita T, Yasui Y, Kobayashi Y, Sato M, Nishibori E, et al. Transport and Magnetic Studies on the Spin State Transition of Pr1-xCaxCoO3 up to High Pressure. Journal of the Physical Society of Japan. 2004;73(7):1987-97.
37. Hejtmánek J, Jirák Z, Kaman O, Knížek K, Šantavá E, Nitta K, et al. Phase transition in Pr0.5Ca0.5CoO3 and related cobaltites. Eur Phys J B. 2013;86(7):1-8.
38. Fultz B, Howe JM. Transmission Electron Microscopy and Diffractometry of Materials. 4 ed. Heidelberg: Springer 2013. 761 p.
39. Kirkland EJ. Advanced Computing in Electron Microscopy. 2nd edition ed. New York: Plenum; 2010.
40. Pennycook SJ, Nellist PD. Scanning Transmission Electron Microscopy: Imaging and Analysis: Springer; 2011.
41. Williams DB, Carter CB. Transmission Electron Microscopy: Springer; 2009.
42. Schattschneider P. Linear and Chiral Dichroism in the Electron Microscope. London, GBR: Pan Stanford Publishing; 2012.
43. Egerton RF. Electron Energy-Loss Spectroscopy in the Electron Microscope. 3 ed. New York: Springer Science; 2011.
44. Goodhew P. General Introduction to Transmission Electron Microscopy (TEM). Aberration-Corrected Analytical Transmission Electron Microscopy: John Wiley & Sons, Ltd; 2011. p. 1-19.
45. Krivanek OL, Corbin GJ, Dellby N, Elston BF, Keyse RJ, Murfitt MF, et al. An electron microscope for the aberration-corrected era. Ultramicroscopy. 2008;108(3):179-95.
46. Ponce A, Mejía-Rosales S, José-Yacamán M. Scanning Transmission Electron Microscopy Methods for the Analysis of Nanoparticles. In: Soloviev M, editor. Nanoparticles in Biology and Medicine. Methods in Molecular Biology. 906: Humana Press; 2012. p. 453-71.

47. Dellby N, Krivanek OL, Nellist PD, Batson PE, Lupini AR. Progress in aberration-corrected scanning transmission electron microscopy. Journal Of Electron Microscopy. 2001;50(3):177-85.
48. Krivanek OL, Dellby N, Lupini AR. Towards sub-Å electron beams. Ultramicroscopy. 1999;78(1–4):1-11.
49. Cowley JM. Electron diffraction phenomena observed with a high resolution STEM instrument. Journal of Electron Microscopy Technique. 1986;3(1):25-44.
50. Lupini AR, Wang P, Nellist PD, Kirkland AI, Pennycook SJ. Aberration measurement using the Ronchigram contrast transfer function. Ultramicroscopy. 2010;110(7):891-8.
51. Pogany AP, Turner PS. Reciprocity in electron diffraction and microscopy. Acta Crystallographica Section A. 1968;24(1):103-9.
52. Cowley JM. IMAGE CONTRAST IN A TRANSMISSION SCANNING ELECTRON MICROSCOPE. Applied Physics Letters. 1969;15(2):58-9.
53. Williams DB, Carter CB. Transmission electron microscopy: Plenum Press; 1996.
54. Nellist PD, Pennycook SJ. Incoherent imaging using dynamically scattered coherent electrons. Ultramicroscopy. 1999;78(1-4):111-24.
55. Jesson DE, Pennycook SJ. Incoherent Imaging Of Crystals Using Thermally Scattered Electrons. Proceedings Of The Royal Society Of London Series A-Mathematical And Physical Sciences. 1995;449(1936):273-93.
56. Pennycook SJ. Z-contrast stem for materials science. Ultramicroscopy. 1989;30(1–2):58-69.
57. Krivanek OL, Dellby N, Murfitt MF, Chisholm MF, Pennycook TJ, Suenaga K, et al. Gentle STEM: ADF imaging and EELS at low primary energies. Ultramicroscopy. 2012;110(8):935-45.
58. Klie RF, Idrobo JC, Browning ND, Serquis A, Zhu YT, Liao XZ, et al. Observation of coherent oxide precipitates in polycrystalline MgB_2. Applied Physics Letters. 2002;80(21):3970-2.
59. Ziegler A, Idrobo JC, Cinibulk MK, Kisielowski C, Browning ND, Ritchie RO. Interface structure and atomic bonding characteristics in silicon nitride ceramics. Science. 2004;306(5702):1768-70.
60. Varela M, Lupini AR, van Benthem K, Borisevich AY, Chisholm MF, Shibata N, et al. Materials characterization in the aberration-corrected scanning transmission electron microscope. Annual Review Of Materials Research. 2005;35:539-69.
61. Muller DA. Structure and bonding at the atomic scale by scanning transmission electron microscopy. Nature Materials. 2009;8(4):263-70.
62. Klie RF, Zhu Y. Atomic resolution STEM analysis of defects and interfaces in ceramic materials. Micron. 2005;36(3):219-31.
63. Watanabe K, Yamazaki T, Kikuchi Y, Kotaka Y, Kawasaki M, Hashimoto I, et al. Atomic-resolution incoherent high-angle annular dark field STEM images of Si(011). Physical Review B. 2001;63(8):085316.
64. Okunishi E, Ishikawa I, Sawada H, Hosokawa F, Hori M, Kondo Y. Visualization of light elements at ultrahigh resolution by stem annular bright field microscopy. Microscopy and Microanalysis. 2009;15(SUPPL. 2):164-5.

65. Okunishi E, Ishikawa I, Sawada H, Hosokawa F, Hori M, Kondo Y. Visualization of light elements using annular bright field imaging with a Cs-corrected scanning transmission electron microscope. Journal of the Vacuum Society of Japan. 2011;54(4):248-52.
66. Findlay SD, Shibata N, Sawada H, Okunishi E, Kondo Y, Ikuhara Y. Dynamics of annular bright field imaging in scanning transmission electron microscopy Ultramicroscopy. 2010;110:903-623.
67. Findlay SD, Shibata N, Sawada H, Okunishi E, Kondo Y, Yamamoto T, et al. Robust atomic resolution imaging of light elements using scanning transmission electron microscopy. Applied Physics Letters. 2009;95(19):191913-3.
68. Phillips PJ, Klie RF. On the visibility of very thin specimens in annular bright field scanning transmission electron microscopy. Applied Physics Letters. 2013;103(3):-.
69. Findlay SD, Kohno Y, Cardamone LA, Ikuhara Y, Shibata N. Enhanced light element imaging in atomic resolution scanning transmission electron microscopy. Ultramicroscopy. 2014;136:31-41.
70. Krivanek OL, Lovejoy TC, Dellby N, Carpenter RW. Monochromated STEM with a 30 meV-wide, atom-sized electron probe. Microscopy. 2013;62(1):3-21.
71. de Groot F. High-Resolution X-ray Emission and X-ray Absorption Spectroscopy. Chemical Reviews. 2001;101(6):1779-808.
72. Zhang J. Application of Electron Energy-Loss Spectroscopy to Ferroelectric Thin Films [Dissertation]. Halle: Martin Luther University of Halle-Wittenberg; 2004.
73. Nishida S, Kobayashi S, Kumamoto A, Ikeno H, Mizoguchi T, Tanaka I, et al. Effect of local coordination of Mn on Mn-L2,3 edge electron energy loss spectrum. Journal of Applied Physics. 2013;114(5):-.
74. Paterson JH, Krivanek OL. Elnes of 3d transition-metal oxides: II. Variations with oxidation state and crystal structure. Ultramicroscopy. 1990;32(4):319-25.
75. Krivanek OL, Paterson JH. Elnes of 3d transition-metal oxides: I. Variations across the periodic table. Ultramicroscopy. 1990;32(4):313-8.
76. Tan H, Verbeeck J, Abakumov A, Van Tendeloo G. Oxidation state and chemical shift investigation in transition metal oxides by EELS. Ultramicroscopy. 2012;116(0):24-33.
77. Riedl T, Gemming T, Gruner W, Acker J, Wetzig K. Determination of manganese valency in La1−xSrxMnO3 using ELNES in the (S)TEM. Micron. 2007;38(3):224-30.
78. Daulton TL, Little BJ. Determination of chromium valence over the range Cr(0)–Cr(VI) by electron energy loss spectroscopy. Ultramicroscopy. 2006;106(7):561-73.
79. Graetz J, Ahn CC, Ouyang H, Rez P, Fultz B. White lines and d-band occupancy for the 3d transition-metal oxides and lithiumtransition-metal oxides. Physical Review B. 2004;69(23):235103.
80. Drummond-Brydson RM, Sauer H, Engel W. Probing Materials Chemistry Using ELNES. Transmission Electron Energy Loss Spectrometry in Materials Science and The EELS Atlas: Wiley-VCH Verlag GmbH & Co. KGaA; 2005. p. 223-70.
81. Wang ZL, Yin JS, Jiang YD. EELS analysis of cation valence states and oxygen vacancies in magnetic oxides. Micron. 2000;31(5):571-80.

82. Stöhr J. Exploring the microscopic origin of magnetic anisotropies with X-ray magnetic circular dichroism (XMCD) spectroscopy. Journal of Magnetism and Magnetic Materials. 1999;200(1–3):470-97.
83. Uchida M, Tonomura A. Generation of electron beams carrying orbital angular momentum. Nature. 2010;464(7289):737-9.
84. Schattschneider P, Löffler S, Stöger-Pollach M, Verbeeck J. Is magnetic chiral dichroism feasible with electron vortices? Ultramicroscopy. 2014;136(0):81-5.
85. Rusz J, Idrobo JC, Bhowmick S. Achieving atomic resolution magnetic dichroism by controlling the phase symmetry of an electron probe. arXiv:14083150v1 [cond-matmtrl-sci]. 2014.
86. Schattschneider P, Rubino S, Hebert C, Rusz J, Kunes J, Novak P, et al. Detection of magnetic circular dichroism using a transmission electron microscope. Nature. 2006;441(7092):486-8.
87. Löffler S, Schattschneider P. A software package for the simulation of energy-loss magnetic chiral dichroism. Ultramicroscopy. 2010;110(7):831-5.
88. Rusz J, Eriksson O, Novák P, Oppeneer PM. Sum rules for electron energy loss near edge spectra. Physical Review B. 2007;76(6):060408.
89. Lidbaum H, Rusz J, Liebig A, Hjörvarsson B, Oppeneer PM, Coronel E, et al. Quantitative Magnetic Information from Reciprocal Space Maps in Transmission Electron Microscopy. Physical Review Letters. 2009;102(3):037201.
90. Schattschneider P, Hébert C, Rubino S, Stöger-Pollach M, Rusz J, Novák P. Magnetic circular dichroism in EELS: Towards 10 nm resolution. Ultramicroscopy. 2008;108(5):433-8.
91. Rubino S, Schattschneider P, Stöger-Pollach M, Hébert C, Rusz J, Calmels L, et al. Energy-loss magnetic chiral dichroism (EMCD): Magnetic chiral dichroism in the electron microscope. Journal of Materials Research. 2008;23(10):2582-90.
92. Schattschneider P, Stöger-Pollach M, Rubino S, Sperl M, Hurm C, Zweck J, et al. Detection of magnetic circular dichroism on the two-nanometer scale. Physical Review B. 2008;78(10):104413.
93. Heikes RR, Miller RC, Mazelsky R. Magnetic and electrical anomalies in $LaCoO_3$. Physica. 1964;30(8):1600-8.
94. Klie RF, Zheng JC, Zhu Y, Varela M, Wu J, Leighton C. Phys Rev Lett. 2007;99:047203.
95. Kwon J-H, Choi WS, Kwon Y-K, Jung R, Zuo J-M, Lee HN, et al. Nanoscale Spin-State Ordering in LaCoO3 Epitaxial Thin Films. Chemistry of Materials. 2014;26(8):2496-501.
96. Biškup N, Salafranca J, Mehta V, Oxley MP, Suzuki Y, Pennycook SJ, et al. Insulating Ferromagnetic $LaCoO_{3-\delta}$ Films: A Phase Induced by Ordering of Oxygen Vacancies. Physical Review Letters. 2014;112(8):087202.
97. Ito Y, Klie RF, Browning ND, Mazanec TJ. Atomic resolution analysis of the defect chemistry and microdomain structure of brownmillerite-type strontium cobaltite. Journal of the American Ceramic Society. 2002;85(4):969-76.
98. Yoo YJ, Yu KK, Kim JY, Lee YP, Kim KW, Hong KP. Physical properties of $La_{1-x}Sr_xCoO_3$. Physica B: Condensed Matter. 2006;385–386, Part 1(0):411-4.

99. Sikolenko VV, Sazonov AP, Troyanchuk IO, Többens D, Zimmermann U, Pomjakushina EV, et al. Magnetic properties of $La_{1-x}Sr_xCoO_3$ (x = 0.15 and 0.3). Journal of Physics: Condensed Matter. 2004;16(41):7313.
100. He C, Eisenberg S, Jan C, Zheng H, Mitchell JF, Leighton C. Heat capacity study of magnetoelectronic phase separation in $LaSrCoO_3$ single crystals. Physical Review B. 2009;80(21):214411.
101. Wang ZL, Bentley J, Evans ND. Valence state mapping of cobalt and manganese using near-edge fine structures. Micron. 2000;31(4):355-62.
102. Haverkort MW, Hu Z, Cezar JC, Burnus T, Hartmann H, Reuther M, et al. Spin state transition in LaCoO 3 studied using soft X-ray absorption spectroscopy and magnetic circular dichroism. Physical review letters. 2006;97(17):176405.
103. Wu L, Wiesmann HJ, Moodenbaugh AR, Klie RF, Zhu Y, Welch DO, et al. Oxidation state and lattice expansion of CeO2 nanoparticles as a function of particle size. Physical Review B. 2004;69(12):125415.
104. Zhao Y, Feltes TE, Regalbuto JR, Meyer RJ, Klie RF. In situ electron energy loss spectroscopy study of metallic Co and Co oxides. Journal of Applied Physics. 2010;108(6):063704-7.
105. Stöger-Pollach M, Treiber CD, Resch GP, Keays DA, Ennen I. EMCD real space maps of Magnetospirillum magnetotacticum. Micron. 2011;42(5):456-60.
106. García-Muñoz JL, Frontera C, Barón-González AJ, Valencia S, Blasco J, Feyerherm R, et al. Valence transition in (Pr,Ca)CoO3 cobaltites: Charge migration at the metal-insulator transition. Physical Review B. 2011;84(4):045104.
107. Fujishiro H, Naito T, Ogawa S, Yoshida N, Nitta K, Hejtmánek J, et al. Valence Shift of Pr Ion from 3+ to 4+ in (Pr1-yYy)0.7Ca0.3CoO3 Estimated by X-Ray Absorption Spectroscopy. Journal of the Physical Society of Japan. 2012;81(6):064709.
108. Kim Y-M, He J, Biegalski MD, Ambaye H, Lauter V, Christen HM, et al. Probing oxygen vacancy concentration and homogeneity in solid-oxide fuel-cell cathode materials on the subunit-cell level. Nat Mater. 2012;11(10):888-94.
109. Gazquez J, Luo W, Oxley MP, Prange M, Torija MA, Sharma M, et al. Atomic-Resolution Imaging of Spin-State Superlattices in Nanopockets within Cobaltite Thin Films. Nano Letters. 2011;11(3):973-6.
110. Stemmer S, Jacobson AJ, Chen X, Ignatiev A. Oxygen vacancy ordering in epitaxial La0.5Sr0.5CoO3−∂ thin films on (001) LaAlO3. Journal of Applied Physics. 2001;90(7):3319-24.
111. Gilbert B, Frazer BH, Belz A, Conrad PG, Nealson KH, Haskel D, et al. Multiple Scattering Calculations of Bonding and X-ray Absorption Spectroscopy of Manganese Oxides. The Journal of Physical Chemistry A. 2003;107(16):2839-47.
112. Rask JH, Miner BA, Buseck PR. Determination of manganese oxidation states in solids by electron energy-loss spectroscopy. Ultramicroscopy. 1987;21(4):321-6.
113. Stoyanov E, Langenhorst F, Steinle-Neumann G. The effect of valence state and site geometry on Ti L3,2 and O K electron energy-loss spectra of TixOy phases. American Mineralogist. 2007;92(4):577-86.
114. Schattschneider P, Schaffer B, Ennen I, Verbeeck J. Mapping spin-polarized transitions with atomic resolution. Physical Review B. 2012;85(13):134422.

115. Oxley MP, Kapetanakis MD, Prange MP, Varela M, Pennycook SJ, Pantelides ST. Simulation of Probe Position-Dependent Electron Energy-Loss Fine Structure. Microscopy and Microanalysis. 2014;20(03):784-97.
116. Klie RF, Qiao Q, Paulauskas T, Ramasse Q, Oxley MP, Idrobo JC. Examining the structure and bonding in complex oxides using aberration-corrected imaging and spectroscopy. Physical Review B. 2012;85(5):054106.
117. Muller DA, Silcox J. Delocalization in inelastic scattering. Ultramicroscopy. 1995;59(1–4):195-213.

University of Illinois at Chicago Department of Physics, 845 w. Taylor St. M/C 273, Chicago, IL
60607•3129965048•agulec2@uic.edu

Ahmet Gulec

Research interest

Atomic and electronic properties of transition metal oxides and ceramic materials and their magnetic and spin state transitions using atomic resolution in situ Z-contrast imaging, electron energy-loss spectroscopy.

Academic and professional experience:

Research Assistant, Nano-Scale Physics Group, University of Illinois at Chicago 2010- present

Teaching Assistant, University of Illinois at Chicago 2009-present

Teaching Assistant, Bogazici University , Istanbul, Turkey 2006-2009

Visitor to USTEM, Vienna Technical University for EMCD measurements, July-August 2013

High Resolution Electron Microscopy Winter School, Arizona State University, February 2012

Visitor to ORNL, training on VG microscopes, August 2011

Education

Graduate

University of Illinois at Chicago 2009 -present
Ph.D. candidate in Physics
Advisor: Robert F. Klie
Bogazici University, Istanbul, Turkey 2006 - 2009
Master of Science, Physics

Undergraduate

Bogazici University, Istanbul, Turkey 2002 - 2006
Bachelor of Science, Physics

Awards and Honors:

University Of Illinois Provost`s Award, 2013
Midwest Microscopy and Microanalysis Society student travel awards, 2012
Conference Grant (for ISSCSMB 08 meeting in Mugla, Turkey 2008
Conference Grant (for FSC meeting in Iasi, Romania) 2007

Basari Scholar (Bogazici University)	2000
Graduation Bachelor degree in Physics in third rank	2006
Ranked in the top 0.1% in the nationwide university entrance exam, Turkey	2000

Publication

1) **"Measuring electron transfer and valance state transitions in $(Pr_{0.85}Y_{0.15})_{0.70}Ca_{0.30}CoO_3$ using in-situ atomic-resolution Z-contrast imaging and EELS", A. Gulec , Klie, R. F., D. Phelan and C. Leighton submission process (2014)**
2) **"Local CoO6 Octahedral distortion and Magnetic transitions in Hole doped LaCoO3" A. Gulec, R. F. Klie, P. Schattschneider, M.Stöger-Pollach, Submission process(2014)**
3) **"Direct measurement of the low temperature spin state transitions in $La_{1-x}Sr_xCoO_3$ ($0.05 < x < 0.3$)" A. Gulec, R.F. Klie, *Journal of Applied Physics* 116, no. 23 (2014)**
4) **"The New Jeol Jem-Arm200cf at the University of Illinois at Chicago.", Klie, R. F., A. Gulec, Z. Guo, T. Paulauskas, Q. Qiao, R. Tao, C. Wang, K. B. Low, A. W. Nicholls and P. J. Phillips. *Crystal Research and Technology* 49, no. 9, 653-662(2014)**
5) **"Reversible Modulation of Orbital Occupations Via an Interface-Induced Polar State in Metallic Manganites", Chen, Hanghui, Qiao Qiao, Matthew S. J. Marshall, Alexandru B. Georgescu, Ahmet Gulec, Patrick J. Phillips, Robert F. Klie, Frederick J. Walker, Charles H. Ahn and Sohrab Ismail-Beigi. *Nano Letters* 14, no. 9, 4965-4970 (2014)**
6) **"Observations of Co4+ in a Higher Spin State and the Increase in the Seebeck Coefficient of Thermoelectric $Ca_3Co_4O_9$," R.F. Klie, Q. Qiao, T. Paulauskas, A. Gulec, A. Rebola, S. Ogut, M.P. Prange, J.C. Idrobo, S.T. Pantelides, S. Kolesnik, B. Dabrowski, M. Ozdemir, C. Boyraz, D. Mazumdar, and A. Gupta, Physical Review Letters, 108(19),196601 (2012)**
7) **"Effect of substrate on the atomic structure and physical properties of thermoelectric $Ca_3Co_4O_9$ thin films," Q. Qiao, A. Gulec, T. Paulauskas, S. Kolesnik, B. Dabrowski, M. Ozdemir, C. Boyraz, D. Mazumdar, A. Gupta, and R.F. Klie,. Journal of Physics-Condensed Matter, 23(30): 305005 (2011)**

Contributed presentation:

" Local Spin State Measurements in Critically Doped LSCO"* A.Gulec, R. F. Klie, *APS March Meeting, Denver, Co, March 2014

"Energy-loss magnetic circular dichroism measurements of ferromagnetic ordering in $LaSrCoO_3$." **A. Gulec, R. F. Klie,** ***MRS Fall meeting, Boston MA, December, 2013***

"Measuring spin-state in $(La_{1-x}Sr_x)CoO_3$ using in-situ atomic-resolution Z-contrast imaging and EELS" **A. Gulec, R.F. Klie,** ***Microscopy & Microanalysis Meeting, Indianapolis, IN, August 2013***

"Energy-loss magnetic circular dichroism measurements of ferromagnetic ordering in $La_{1-x}Sr_xCoO_3$" A. Gulec, R. F. Klie, J. F. Mitchell, ***APS March Meeting,*** **Baltimore, MD, March 2013**

Contributed poster presentation:

"Measuring electron transfer and valance state transitions in $(Pr_{0.85}Y_{0.15})_{0.7}Ca_{0.3}CoO_3$ using in-situ atomic-resolution Z-contrast imaging and EELS", A. Gulec , Klie, R. F., D. ***Microscopy & Microanalysis Meeting,*** **Hartford,CT, August 2014**

"Direct measurement of the low temperature spin state transitions in $La_{1-x}Sr_xCoO_3$ ($0.05 < x < 0.3$)" A. Gulec, Robert Klie, ***Physics at the Falls: Structural and Electronic Instabilities in Oxide Nanostructures,*** **Amherst, NY, May 2014**

"Measuring spin-state and ferromagnetic transitions in $La_{1-x}Sr_xCoO_3$ using in-situ atomic-resolution Z-contrast imaging and EELS" A. Gulec, R.F. Klie, ***M3S 55th Anniversary Meeting,*** **Deerfield, IL, November 2012**

"Measuring spin-state and ferromagnetic transitions in $La_{1-x}Sr_xCoO_3$ using in-situ atomic-resolution Z-contrast imaging and EELS" A. Gulec, R.F. Klie, ***Microscopy & Microanalysis Meeting,*** **Phoenix, AZ, August 2012**

ELSEVIER LICENSE
TERMS AND CONDITIONS

Oct 06, 2014

This is a License Agreement between Ahmet Gulec ("You") and Elsevier ("Elsevier") provided by Copyright Clearance Center ("CCC"). The license consists of your order details, the terms and conditions provided by Elsevier, and the payment terms and conditions.

All payments must be made in full to CCC. For payment instructions, please see information listed at the bottom of this form.

Supplier	Elsevier Limited The Boulevard,Langford Lane Kidlington,Oxford,OX5 1GB,UK
Registered Company Number	1982084
Customer name	Ahmet Gulec
Customer address	UIC Department Of Physics CHICAGO, IL 60607
License number	3483201002418
License date	Oct 06, 2014
Licensed content publisher	Elsevier
Licensed content publication	Ultramicroscopy
Licensed content title	Dynamics of annular bright field imaging in scanning transmission electron microscopy
Licensed content author	S.D. Findlay,N. Shibata,H. Sawada,E. Okunishi,Y. Kondo,Y. Ikuhara
Licensed content date	June 2010
Licensed content volume number	110
Licensed content issue number	7
Number of pages	21
Start Page	903
End Page	923
Type of Use	reuse in a thesis/dissertation
Portion	figures/tables/illustrations
Number of figures/tables/illustrations	1
Format	both print and electronic
Are you the author of this Elsevier article?	No
Will you be translating?	No

Title of your thesis/dissertation	Atomic-Scale Study Of Complex Cobalt Oxide Using Scanning Transmission Electron Microscope
Expected completion date	Oct 2014
Estimated size (number of pages)	150
Elsevier VAT number	GB 494 6272 12
Permissions price	0.00 USD
VAT/Local Sales Tax	0.00 USD / 0.00 GBP
Total	0.00 USD
Terms and Conditions	

INTRODUCTION

1. The publisher for this copyrighted material is Elsevier. By clicking "accept" in connection with completing this licensing transaction, you agree that the following terms and conditions apply to this transaction (along with the Billing and Payment terms and conditions established by Copyright Clearance Center, Inc. ("CCC"), at the time that you opened your Rightslink account and that are available at any time at http://myaccount.copyright.com).

GENERAL TERMS

2. Elsevier hereby grants you permission to reproduce the aforementioned material subject to the terms and conditions indicated.

3. Acknowledgement: If any part of the material to be used (for example, figures) has appeared in our publication with credit or acknowledgement to another source, permission must also be sought from that source. If such permission is not obtained then that material may not be included in your publication/copies. Suitable acknowledgement to the source must be made, either as a footnote or in a reference list at the end of your publication, as follows:

"Reprinted from Publication title, Vol /edition number, Author(s), Title of article / title of chapter, Pages No., Copyright (Year), with permission from Elsevier [OR APPLICABLE SOCIETY COPYRIGHT OWNER]." Also Lancet special credit - "Reprinted from The Lancet, Vol. number, Author(s), Title of article, Pages No., Copyright (Year), with permission from Elsevier."

4. Reproduction of this material is confined to the purpose and/or media for which permission is hereby given.

5. Altering/Modifying Material: Not Permitted. However figures and illustrations may be altered/adapted minimally to serve your work. Any other abbreviations, additions, deletions and/or any other alterations shall be made only with prior written authorization of Elsevier Ltd. (Please contact Elsevier at permissions@elsevier.com)

6. If the permission fee for the requested use of our material is waived in this instance, please be advised that your future requests for Elsevier materials may attract a fee.

7. Reservation of Rights: Publisher reserves all rights not specifically granted in the

combination of (i) the license details provided by you and accepted in the course of this licensing transaction, (ii) these terms and conditions and (iii) CCC's Billing and Payment terms and conditions.

8. License Contingent Upon Payment: While you may exercise the rights licensed immediately upon issuance of the license at the end of the licensing process for the transaction, provided that you have disclosed complete and accurate details of your proposed use, no license is finally effective unless and until full payment is received from you (either by publisher or by CCC) as provided in CCC's Billing and Payment terms and conditions. If full payment is not received on a timely basis, then any license preliminarily granted shall be deemed automatically revoked and shall be void as if never granted. Further, in the event that you breach any of these terms and conditions or any of CCC's Billing and Payment terms and conditions, the license is automatically revoked and shall be void as if never granted. Use of materials as described in a revoked license, as well as any use of the materials beyond the scope of an unrevoked license, may constitute copyright infringement and publisher reserves the right to take any and all action to protect its copyright in the materials.

9. Warranties: Publisher makes no representations or warranties with respect to the licensed material.

10. Indemnity: You hereby indemnify and agree to hold harmless publisher and CCC, and their respective officers, directors, employees and agents, from and against any and all claims arising out of your use of the licensed material other than as specifically authorized pursuant to this license.

11. No Transfer of License: This license is personal to you and may not be sublicensed, assigned, or transferred by you to any other person without publisher's written permission.

12. No Amendment Except in Writing: This license may not be amended except in a writing signed by both parties (or, in the case of publisher, by CCC on publisher's behalf).

13. Objection to Contrary Terms: Publisher hereby objects to any terms contained in any purchase order, acknowledgment, check endorsement or other writing prepared by you, which terms are inconsistent with these terms and conditions or CCC's Billing and Payment terms and conditions. These terms and conditions, together with CCC's Billing and Payment terms and conditions (which are incorporated herein), comprise the entire agreement between you and publisher (and CCC) concerning this licensing transaction. In the event of any conflict between your obligations established by these terms and conditions and those established by CCC's Billing and Payment terms and conditions, these terms and conditions shall control.

14. Revocation: Elsevier or Copyright Clearance Center may deny the permissions described in this License at their sole discretion, for any reason or no reason, with a full refund payable to you. Notice of such denial will be made using the contact information provided by you. Failure to receive such notice will not alter or invalidate the denial. In no event will Elsevier or Copyright Clearance Center be responsible or liable for any costs, expenses or damage incurred by you as a result of a denial of your permission request, other than a refund of the amount(s) paid by you to Elsevier and/or Copyright Clearance Center for denied permissions.

LIMITED LICENSE

The following terms and conditions apply only to specific license types:

15. **Translation**: This permission is granted for non-exclusive world **English** rights only unless your license was granted for translation rights. If you licensed translation rights you may only translate this content into the languages you requested. A professional translator must perform all translations and reproduce the content word for word preserving the integrity of the article. If this license is to re-use 1 or 2 figures then permission is granted for non-exclusive world rights in all languages.

16. **Posting licensed content on any Website**: The following terms and conditions apply as follows: Licensing material from an Elsevier journal: All content posted to the web site must maintain the copyright information line on the bottom of each image; A hyper-text must be included to the Homepage of the journal from which you are licensing at http://www.sciencedirect.com/science/journal/xxxxx or the Elsevier homepage for books at http://www.elsevier.com; Central Storage: This license does not include permission for a scanned version of the material to be stored in a central repository such as that provided by Heron/XanEdu.

Licensing material from an Elsevier book: A hyper-text link must be included to the Elsevier homepage at http://www.elsevier.com . All content posted to the web site must maintain the copyright information line on the bottom of each image.

Posting licensed content on Electronic reserve: In addition to the above the following clauses are applicable: The web site must be password-protected and made available only to bona fide students registered on a relevant course. This permission is granted for 1 year only. You may obtain a new license for future website posting.

For journal authors: the following clauses are applicable in addition to the above: Permission granted is limited to the author accepted manuscript version* of your paper.

***Accepted Author Manuscript (AAM) Definition:** An accepted author manuscript (AAM) is the author's version of the manuscript of an article that has been accepted for publication and which may include any author-incorporated changes suggested through the processes of submission processing, peer review, and editor-author communications. AAMs do not include other publisher value-added contributions such as copy-editing, formatting, technical enhancements and (if relevant) pagination.

You are not allowed to download and post the published journal article (whether PDF or HTML, proof or final version), nor may you scan the printed edition to create an electronic version. A hyper-text must be included to the Homepage of the journal from which you are licensing at http://www.sciencedirect.com/science/journal/xxxxx. As part of our normal production process, you will receive an e-mail notice when your article appears on Elsevier's online service ScienceDirect (www.sciencedirect.com). That e-mail will include the article's Digital Object Identifier (DOI). This number provides the electronic link to the published article and should be included in the posting of your personal version. We ask that you wait until you receive this e-mail and have the DOI to do any posting.

Posting to a repository: Authors may post their AAM immediately to their employer's institutional repository for internal use only and may make their manuscript publically

available after the journal-specific embargo period has ended.

Please also refer to Elsevier's Article Posting Policy for further information.

18. **For book authors** the following clauses are applicable in addition to the above: Authors are permitted to place a brief summary of their work online only.. You are not allowed to download and post the published electronic version of your chapter, nor may you scan the printed edition to create an electronic version. **Posting to a repository:** Authors are permitted to post a summary of their chapter only in their institution's repository.

20. **Thesis/Dissertation**: If your license is for use in a thesis/dissertation your thesis may be submitted to your institution in either print or electronic form. Should your thesis be published commercially, please reapply for permission. These requirements include permission for the Library and Archives of Canada to supply single copies, on demand, of the complete thesis and include permission for UMI to supply single copies, on demand, of the complete thesis. Should your thesis be published commercially, please reapply for permission.

Elsevier Open Access Terms and Conditions

Elsevier publishes Open Access articles in both its Open Access journals and via its Open Access articles option in subscription journals.

Authors publishing in an Open Access journal or who choose to make their article Open Access in an Elsevier subscription journal select one of the following Creative Commons user licenses, which define how a reader may reuse their work: Creative Commons Attribution License (CC BY), Creative Commons Attribution – Non Commercial - ShareAlike (CC BY NC SA) and Creative Commons Attribution – Non Commercial – No Derivatives (CC BY NC ND)

Terms & Conditions applicable to all Elsevier Open Access articles:

Any reuse of the article must not represent the author as endorsing the adaptation of the article nor should the article be modified in such a way as to damage the author's honour or reputation.

The author(s) must be appropriately credited.

If any part of the material to be used (for example, figures) has appeared in our publication with credit or acknowledgement to another source it is the responsibility of the user to ensure their reuse complies with the terms and conditions determined by the rights holder.

Additional Terms & Conditions applicable to each Creative Commons user license:

CC BY: You may distribute and copy the article, create extracts, abstracts, and other revised versions, adaptations or derivative works of or from an article (such as a translation), to include in a collective work (such as an anthology), to text or data mine the article, including for commercial purposes without permission from Elsevier

CC BY NC SA: For non-commercial purposes you may distribute and copy the article,

create extracts, abstracts and other revised versions, adaptations or derivative works of or from an article (such as a translation), to include in a collective work (such as an anthology), to text and data mine the article and license new adaptations or creations under identical terms without permission from Elsevier

CC BY NC ND: For non-commercial purposes you may distribute and copy the article and include it in a collective work (such as an anthology), provided you do not alter or modify the article, without permission from Elsevier

Any commercial reuse of Open Access articles published with a CC BY NC SA or CC BY NC ND license requires permission from Elsevier and will be subject to a fee.

Commercial reuse includes:

- Promotional purposes (advertising or marketing)
- Commercial exploitation (e.g. a product for sale or loan)
- Systematic distribution (for a fee or free of charge)

Please refer to Elsevier's Open Access Policy for further information.

21. **Other Conditions**:

v1.6

Questions? customercare@copyright.com or +1-855-239-3415 (toll free in the US) or +1-978-646-2777.

Gratis licenses (referencing $0 in the Total field) are free. Please retain this printable license for your reference. No payment is required.

ELSEVIER LICENSE
TERMS AND CONDITIONS

Oct 06, 2014

This is a License Agreement between Ahmet Gulec ("You") and Elsevier ("Elsevier") provided by Copyright Clearance Center ("CCC"). The license consists of your order details, the terms and conditions provided by Elsevier, and the payment terms and conditions.

All payments must be made in full to CCC. For payment instructions, please see information listed at the bottom of this form.

Supplier	Elsevier Limited The Boulevard,Langford Lane Kidlington,Oxford,OX5 1GB,UK
Registered Company Number	1982084
Customer name	Ahmet Gulec
Customer address	UIC Department Of Physics CHICAGO, IL 60607
License number	3483201303799
License date	Oct 06, 2014
Licensed content publisher	Elsevier
Licensed content publication	Ultramicroscopy
Licensed content title	Enhanced light element imaging in atomic resolution scanning transmission electron microscopy
Licensed content author	S.D. Findlay,Y. Kohno,L.A. Cardamone,Y. Ikuhara,N. Shibata
Licensed content date	January 2014
Licensed content volume number	136
Licensed content issue number	n/a
Number of pages	11
Start Page	31
End Page	41
Type of Use	reuse in a thesis/dissertation
Intended publisher of new work	other
Portion	figures/tables/illustrations
Number of figures/tables/illustrations	1
Format	both print and electronic
Are you the author of this	No

Elsevier article?	
Will you be translating?	No
Title of your thesis/dissertation	Atomic-Scale Study Of Complex Cobalt Oxide Using Scanning Transmission Electron Microscope
Expected completion date	Oct 2014
Estimated size (number of pages)	150
Elsevier VAT number	GB 494 6272 12
Permissions price	0.00 USD
VAT/Local Sales Tax	0.00 USD / 0.00 GBP
Total	0.00 USD
Terms and Conditions	

INTRODUCTION

1. The publisher for this copyrighted material is Elsevier. By clicking "accept" in connection with completing this licensing transaction, you agree that the following terms and conditions apply to this transaction (along with the Billing and Payment terms and conditions established by Copyright Clearance Center, Inc. ("CCC"), at the time that you opened your Rightslink account and that are available at any time at http://myaccount.copyright.com).

GENERAL TERMS

2. Elsevier hereby grants you permission to reproduce the aforementioned material subject to the terms and conditions indicated.

3. Acknowledgement: If any part of the material to be used (for example, figures) has appeared in our publication with credit or acknowledgement to another source, permission must also be sought from that source. If such permission is not obtained then that material may not be included in your publication/copies. Suitable acknowledgement to the source must be made, either as a footnote or in a reference list at the end of your publication, as follows:

"Reprinted from Publication title, Vol /edition number, Author(s), Title of article / title of chapter, Pages No., Copyright (Year), with permission from Elsevier [OR APPLICABLE SOCIETY COPYRIGHT OWNER]." Also Lancet special credit - "Reprinted from The Lancet, Vol. number, Author(s), Title of article, Pages No., Copyright (Year), with permission from Elsevier."

4. Reproduction of this material is confined to the purpose and/or media for which permission is hereby given.

5. Altering/Modifying Material: Not Permitted. However figures and illustrations may be altered/adapted minimally to serve your work. Any other abbreviations, additions, deletions and/or any other alterations shall be made only with prior written authorization of Elsevier Ltd. (Please contact Elsevier at permissions@elsevier.com)

6. If the permission fee for the requested use of our material is waived in this instance,

please be advised that your future requests for Elsevier materials may attract a fee.

7. Reservation of Rights: Publisher reserves all rights not specifically granted in the combination of (i) the license details provided by you and accepted in the course of this licensing transaction, (ii) these terms and conditions and (iii) CCC's Billing and Payment terms and conditions.

8. License Contingent Upon Payment: While you may exercise the rights licensed immediately upon issuance of the license at the end of the licensing process for the transaction, provided that you have disclosed complete and accurate details of your proposed use, no license is finally effective unless and until full payment is received from you (either by publisher or by CCC) as provided in CCC's Billing and Payment terms and conditions. If full payment is not received on a timely basis, then any license preliminarily granted shall be deemed automatically revoked and shall be void as if never granted. Further, in the event that you breach any of these terms and conditions or any of CCC's Billing and Payment terms and conditions, the license is automatically revoked and shall be void as if never granted. Use of materials as described in a revoked license, as well as any use of the materials beyond the scope of an unrevoked license, may constitute copyright infringement and publisher reserves the right to take any and all action to protect its copyright in the materials.

9. Warranties: Publisher makes no representations or warranties with respect to the licensed material.

10. Indemnity: You hereby indemnify and agree to hold harmless publisher and CCC, and their respective officers, directors, employees and agents, from and against any and all claims arising out of your use of the licensed material other than as specifically authorized pursuant to this license.

11. No Transfer of License: This license is personal to you and may not be sublicensed, assigned, or transferred by you to any other person without publisher's written permission.

12. No Amendment Except in Writing: This license may not be amended except in a writing signed by both parties (or, in the case of publisher, by CCC on publisher's behalf).

13. Objection to Contrary Terms: Publisher hereby objects to any terms contained in any purchase order, acknowledgment, check endorsement or other writing prepared by you, which terms are inconsistent with these terms and conditions or CCC's Billing and Payment terms and conditions. These terms and conditions, together with CCC's Billing and Payment terms and conditions (which are incorporated herein), comprise the entire agreement between you and publisher (and CCC) concerning this licensing transaction. In the event of any conflict between your obligations established by these terms and conditions and those established by CCC's Billing and Payment terms and conditions, these terms and conditions shall control.

14. Revocation: Elsevier or Copyright Clearance Center may deny the permissions described in this License at their sole discretion, for any reason or no reason, with a full refund payable to you. Notice of such denial will be made using the contact information provided by you. Failure to receive such notice will not alter or invalidate the denial. In no event will Elsevier or Copyright Clearance Center be responsible or liable for any costs, expenses or damage incurred by you as a result of a denial of your permission request, other than a refund of the

amount(s) paid by you to Elsevier and/or Copyright Clearance Center for denied permissions.

LIMITED LICENSE

The following terms and conditions apply only to specific license types:

15. **Translation**: This permission is granted for non-exclusive world **English** rights only unless your license was granted for translation rights. If you licensed translation rights you may only translate this content into the languages you requested. A professional translator must perform all translations and reproduce the content word for word preserving the integrity of the article. If this license is to re-use 1 or 2 figures then permission is granted for non-exclusive world rights in all languages.

16. **Posting licensed content on any Website**: The following terms and conditions apply as follows: Licensing material from an Elsevier journal: All content posted to the web site must maintain the copyright information line on the bottom of each image; A hyper-text must be included to the Homepage of the journal from which you are licensing at http://www.sciencedirect.com/science/journal/xxxxx or the Elsevier homepage for books at http://www.elsevier.com; Central Storage: This license does not include permission for a scanned version of the material to be stored in a central repository such as that provided by Heron/XanEdu.

Licensing material from an Elsevier book: A hyper-text link must be included to the Elsevier homepage at http://www.elsevier.com . All content posted to the web site must maintain the copyright information line on the bottom of each image.

Posting licensed content on Electronic reserve: In addition to the above the following clauses are applicable: The web site must be password-protected and made available only to bona fide students registered on a relevant course. This permission is granted for 1 year only. You may obtain a new license for future website posting.

For journal authors: the following clauses are applicable in addition to the above: Permission granted is limited to the author accepted manuscript version* of your paper.

***Accepted Author Manuscript (AAM) Definition:** An accepted author manuscript (AAM) is the author's version of the manuscript of an article that has been accepted for publication and which may include any author-incorporated changes suggested through the processes of submission processing, peer review, and editor-author communications. AAMs do not include other publisher value-added contributions such as copy-editing, formatting, technical enhancements and (if relevant) pagination.

You are not allowed to download and post the published journal article (whether PDF or HTML, proof or final version), nor may you scan the printed edition to create an electronic version. A hyper-text must be included to the Homepage of the journal from which you are licensing at http://www.sciencedirect.com/science/journal/xxxxx. As part of our normal production process, you will receive an e-mail notice when your article appears on Elsevier's online service ScienceDirect (www.sciencedirect.com). That e-mail will include the article's Digital Object Identifier (DOI). This number provides the electronic link to the published article and should be included in the posting of your personal version. We ask that you wait until you receive this e-mail and have the DOI to do any posting.

Posting to a repository: Authors may post their AAM immediately to their employer's institutional repository for internal use only and may make their manuscript publically available after the journal-specific embargo period has ended.

Please also refer to Elsevier's Article Posting Policy for further information.

18. **For book authors** the following clauses are applicable in addition to the above: Authors are permitted to place a brief summary of their work online only.. You are not allowed to download and post the published electronic version of your chapter, nor may you scan the printed edition to create an electronic version. **Posting to a repository:** Authors are permitted to post a summary of their chapter only in their institution's repository.

20. **Thesis/Dissertation**: If your license is for use in a thesis/dissertation your thesis may be submitted to your institution in either print or electronic form. Should your thesis be published commercially, please reapply for permission. These requirements include permission for the Library and Archives of Canada to supply single copies, on demand, of the complete thesis and include permission for UMI to supply single copies, on demand, of the complete thesis. Should your thesis be published commercially, please reapply for permission.

Elsevier Open Access Terms and Conditions

Elsevier publishes Open Access articles in both its Open Access journals and via its Open Access articles option in subscription journals.

Authors publishing in an Open Access journal or who choose to make their article Open Access in an Elsevier subscription journal select one of the following Creative Commons user licenses, which define how a reader may reuse their work: Creative Commons Attribution License (CC BY), Creative Commons Attribution – Non Commercial - ShareAlike (CC BY NC SA) and Creative Commons Attribution – Non Commercial – No Derivatives (CC BY NC ND)

Terms & Conditions applicable to all Elsevier Open Access articles:

Any reuse of the article must not represent the author as endorsing the adaptation of the article nor should the article be modified in such a way as to damage the author's honour or reputation.

The author(s) must be appropriately credited.

If any part of the material to be used (for example, figures) has appeared in our publication with credit or acknowledgement to another source it is the responsibility of the user to ensure their reuse complies with the terms and conditions determined by the rights holder.

Additional Terms & Conditions applicable to each Creative Commons user license:

CC BY: You may distribute and copy the article, create extracts, abstracts, and other revised versions, adaptations or derivative works of or from an article (such as a translation), to include in a collective work (such as an anthology), to text or data mine the article, including for commercial purposes without permission from Elsevier

CC BY NC SA: For non-commercial purposes you may distribute and copy the article, create extracts, abstracts and other revised versions, adaptations or derivative works of or from an article (such as a translation), to include in a collective work (such as an anthology), to text and data mine the article and license new adaptations or creations under identical terms without permission from Elsevier

CC BY NC ND: For non-commercial purposes you may distribute and copy the article and include it in a collective work (such as an anthology), provided you do not alter or modify the article, without permission from Elsevier

Any commercial reuse of Open Access articles published with a CC BY NC SA or CC BY NC ND license requires permission from Elsevier and will be subject to a fee.

Commercial reuse includes:

- Promotional purposes (advertising or marketing)
- Commercial exploitation (e.g. a product for sale or loan)
- Systematic distribution (for a fee or free of charge)

Please refer to Elsevier's Open Access Policy for further information.

21. **Other Conditions**:

v1.6

Questions? customercare@copyright.com or +1-855-239-3415 (toll free in the US) or +1-978-646-2777.

Gratis licenses (referencing $0 in the Total field) are free. Please retain this printable license for your reference. No payment is required.

AIP PUBLISHING LLC LICENSE TERMS AND CONDITIONS

Jan 30, 2015

All payments must be made in full to CCC. For payment instructions, please see information listed at the bottom of this form.

License Number	3558581230894
Order Date	Jan 30, 2015
Publisher	AIP Publishing LLC
Publication	Journal of Applied Physics
Article Title	Direct measurement of the low temperature spin state transitions in La1−xSrxCoO3 (0.05 < x < 0.3)
Author	A. Gulec,R. F. Klie
Online Publication Date	Dec 15, 2014
Volume number	116
Issue number	23
Type of Use	Thesis/Dissertation
Requestor type	Author (original article)
Format	Print and electronic
Portion	Figure/Table
Number of figures/tables	3
Title of your thesis / dissertation	Atomic-Scale Study Of Complex Cobalt Oxide Using Scanning Transmission Electron Microscope
Expected completion date	May 2015
Estimated size (number of pages)	150
Total	0.00 USD

Terms and Conditions

AIP Publishing LLC -- Terms and Conditions: Permissions Uses

AIP Publishing LLC ("AIPP"") hereby grants to you the non-exclusive right and license to use and/or distribute the Material according to the use specified in your order, on a one-time basis, for the specified term, with a maximum distribution equal to the number that you have ordered. Any links or other content accompanying the Material are not the subject of this license.

1. You agree to include the following copyright and permission notice with the reproduction of the Material:"Reprinted with permission from [FULL CITATION]. Copyright [PUBLICATION YEAR], AIP Publishing LLC." For an article, the copyright and permission notice must be printed on the first page of the article or book chapter. For photographs, covers, or tables, the copyright and permission notice may appear with the Material, in a footnote, or in the reference list.
2. If you have licensed reuse of a figure, photograph, cover, or table, it is your responsibility to ensure that the material is original to AIPP and does not contain the copyright of another entity, and that the copyright notice of the figure, photograph, cover, or table does not indicate that it was reprinted by AIPP, with permission, from another source. Under no circumstances does AIPP, purport or intend to grant permission to reuse material to which it does not hold copyright.
3. You may not alter or modify the Material in any manner. You may translate the Material into another language only if you have licensed translation rights. You may not use the

Material for promotional purposes. AIPP reserves all rights not specifically granted herein.

4. The foregoing license shall not take effect unless and until AIPP or its agent, Copyright Clearance Center, receives the Payment in accordance with Copyright Clearance Center Billing and Payment Terms and Conditions, which are incorporated herein by reference.
5. AIPP or the Copyright Clearance Center may, within two business days of granting this license, revoke the license for any reason whatsoever, with a full refund payable to you. Should you violate the terms of this license at any time, AIPP, AIP Publishing LLC, or Copyright Clearance Center may revoke the license with no refund to you. Notice of such revocation will be made using the contact information provided by you. Failure to receive such notice will not nullify the revocation.
6. AIPP makes no representations or warranties with respect to the Material. You agree to indemnify and hold harmless AIPP, AIP Publishing LLC, and their officers, directors, employees or agents from and against any and all claims arising out of your use of the Material other than as specifically authorized herein.
7. The permission granted herein is personal to you and is not transferable or assignable without the prior written permission of AIPP. This license may not be amended except in a writing signed by the party to be charged.
8. If purchase orders, acknowledgments or check endorsements are issued on any forms containing terms and conditions which are inconsistent with these provisions, such inconsistent terms and conditions shall be of no force and effect. This document, including the CCC Billing and Payment Terms and Conditions, shall be the entire agreement between the parties relating to the subject matter hereof.

This Agreement shall be governed by and construed in accordance with the laws of the State of New York. Both parties hereby submit to the jurisdiction of the courts of New York County for purposes of resolving any disputes that may arise hereunder.

Questions? customercare@copyright.com or +1-855-239-3415 (toll free in the US) or +1-978-646-2777.

Gratis licenses (referencing $0 in the Total field) are free. Please retain this printable license for your reference. No payment is required.